PHYSIK–DEPARTMENT

Lattice Dynamics in Ferromagnetic Shape Memory Alloy System Ni–Mn–Ga

Dissertation
von

Semih Ener

TECHNISCHE UNIVERSITÄT
MÜNCHEN

TECHNISCHE UNIVERSITÄT MÜNCHEN

Physik-Department
Lehrstuhl für Funktionelle Materialien

Lattice Dynamics in Ferromagnetic Shape Memory Alloy System Ni-Mn-Ga

Semih Ener

Vollständiger Abdruck der von der Fakultät für Physik der Technischen Universität München zur Erlangung des akademischen Grades eines

Doktors der Naturwissenschaften (Dr. rer. nat.)

genehmigten Dissertation.

Vorsitzender: Univ.-Prof. Dr. J. L. van Hemmen
Prüfer der Dissertation:
1. Univ.-Prof. Dr. W. Petry
2. Univ.-Prof. Chr. Pfleiderer, Ph.D.

Die Dissertation wurde am 13.11.2012 bei der Technischen Universität München eingereicht und durch die Fakultät für Physik am 07.12.2012 angenommen.

Abstract

Shape memory alloys are materials which are able to recover their initial form during a structural transition. When the shape recovery is achieved by an external magnetic field, the effect is named magnetic shape memory effect and the materials showing this effect are called ferromagnetic shape memory alloys (FSMAs). Most of the FSMAs exhibit a structural transition which is accompanied by a phonon anomaly. In this work, the vibrational properties of Ni-Mn-Ga ferromagnetic shape memory alloys have been investigated by means of inelastic neutron scattering.

Physical characterizations of the investigated single crystals have been done by means of different methods. Calorimetric and magnetic measurements were carried out to determine the structural transition and magnetic ordering temperatures. To see the effect of offstoichiometry, neutron diffraction measurements have been carried out on offstoichiometric samples in austenite and five-layer modulated (5M) martensite phases. These studies reveal that the excess manganese atoms occupy only the gallium sites in both austenite and martensite phases.

Experimental investigations and theoretical predictions show that the structural and magnetic transition properties of Ni-Mn-Ga alloys are strongly depending on the chemical composition. For FSMAs, it is possible to tune the structural and magnetic transition temperatures by varying the chemical composition. The effect of compositional differences on the vibrational properties has been investigated by measuring the high symmetry phonon modes in the austenite phases of Ni_2MnGa and $Ni_{49}Mn_{32}Ga_{19}$. For the first time, Born-von Kármán model fits were applied to the measured austenite phonon dispersions. Thermodynamic properties have been calculated from these models and compared to values from literature. A very good agreement is observed. Observed phonon dispersions in the austenite phases of Ni_2MnGa and $Ni_{49}Mn_{32}Ga_{19}$ lie in the same frequency region. In $Ni_{49}Mn_{32}Ga_{19}$, optical modes show flatter distribution due to the different occupancies of excess manganese atoms. In the overall phonon dispersion, the most prominent difference has been observed in the $TA_2[\xi\xi0]$-modes of stoichiometric and offstoichiometric compositions. In the case of Ni_2MnGa, the $TA_2[\xi\xi0]$-mode shows a strong softening centered at ξ=0.33 r.l.u. For the offstoichiometric composition, the softening is less pronounced and

centered around ξ=0.27 r.l.u.

Investigations of the effect of temperature on $TA_2[\xi\xi0]$-modes have been carried out for both stoichiometric and offstoichiometric compositions. Similar overall linear behaviour has been observed for both compositions. The square of the phonon frequencies becomes soft without reaching zero while approaching the structural transition temperature from both sides. No significant jump has been observed in the soft mode frequencies at the structural transition temperature. The observed anomalies on the $TA_2[\xi\xi0]$-modes of Ni-Mn-Ga alloys have been compared to the literature which exhibits similar martensite transitions. The elastic constants have been calculated from the initial slopes of the acoustic modes for both compositions. The results for the elastic constant C' reveal that in Ni_2MnGa shear does not play a role in the premartensite phase transition. In the case of $Ni_{49}Mn_{32}Ga_{19}$, the elastic constants C' show a temperature dependence which indicates the effect of shear in the martensite phase transition.

The vibrational properties of the low temperature martensite phases of 5M martensite and non-modulated (NM) marteniste have been measured on $Ni_{50}Mn_{29}Ga_{21}$ and $Ni_{50}Mn_{30}Ga_{20}$ compositions, respectively. The phonon dispersion measurements of the martensite phases show that the optical modes lie in a similar frequency region as in the austenite phase. The observed softening in the $TA_2[\xi\xi0]$-mode is smeared out in the martensite phase but still keeps its existence. Additionally, due to the modulation, low frequency excitations have been observed below the 1 THz region of the $[\xi\xi0]$. These observed low frequency excitations have been compared to the low frequency excitations of the premartensite and martensite phases of the stoichiometric composition. In the 5M phase, low frequency excitations were accompanied by commensurate superstructure Bragg peaks. In Ni_2MnGa, the low frequency excitations were accompanied with commensurate (ξ=0.33 r.l.u.) and incommensurate (ξ=0.43 r.l.u.) elastic peaks, in premartensite and martensite phases, respectively. These low frequency excitations observed in Ni_2MnGa have been attributed to charge density waves (CDW). In the offstoichiometric 5M martensite no evidence of CDWs were found.

The stabilization of the austenite phases and the driving forces for the structural transition have been investigated by means of the entropy calculations. The calculations show the lattice entropy alone is not enough to stabilize the austenite phase or drive the martensitic phase transition. The magnetic and electronic entropies play an important role on the transition and phase stabilization properties of Ni-Mn-Ga alloys.

Kurzzusammenfassung

Formgedächtnis-Legierungen sind Materialien, die nach einer plastischen Verformung ihre Ausgangsform mit Durchlaufen einer Phasenumwandlung wieder erlangen. Wenn das Formgedächtnis durch ein externes magnetisches Feld erreicht wird, spricht man vom magnetischen Formgedächtnis-Effekt. Materialien, die dieses Verhalten zeigen, werden als ferromagnetische Formgedächtnis-Legierungen bezeichnet (ferromagnetic shape memory alloys, FSMAs). Die meisten FSMAs zeigen eine Strukturänderung, die mit einer Phononen-Anomalie einher geht. In dieser Arbeit wurden die Vibrationsmoden von Ni-Mn-Ga FSMAs mittels inelastischer Neutronenstreuung untersucht.

Die physikalische Charakterisierung der untersuchten Einkristalle wurde mit mehreren Methoden durchgeführt. Kalorimetrische und magnetische Messungen dienten der Bestimmung des strukturellen Übergangs und der magnetischen Ordnungstemperaturen. Um den Effekt der nicht-stöchiometrischen Zusammensetzung zu sehen, wurden Neutronenstreuexperimente an diesen Proben in der Austenit- und der Fünffach-modulierten (5M)-Martensite Phase ausgeführt. Diese Studien zeigen, dass die überzähligen Mangan Atome nur die Positionen des Galliums einnehmen, sowohl in der Austenit- als auch in der Martensit-Phase.

Experimentelle Untersuchungen und theoretische Vorraussagen zeigen, dass die Eigenschaften des strukturellen und magnetischen Übergangs von Ni-Mn-Ga Legierungen stark mit der chemischen Zusammensetzung variieren. So lassen sich die strukturellen und magnetischen Übergangstemperaturen für FSMAs durch Änderung der chemischen Zusammensetzung gezielt einstellen. Der Effekt der unterschiedlichen Zusammensetzungen auf die Vibrationseigenschaften der Austenit-Phasen von Ni_2MnGa und $Ni_{49}Mn_{32}Ga_{19}$ wurde mittels Messung der Phonen moden in Hochsymmetrierichtungen untersucht. Zum ersten Mal wurden Born-von Kármán Modelle für die Interpretation der gemessenen Austenit-Phonendispersionen verwendet. Thermodynamische Eigenschaften wurden aus diesen Modellen extrahiert und mit theoretischen Vorraussagen aus der Literatur verglichen, wobei eine sehr gute Übereinstimmung gefunden wurde. Die beobachteten Phonendispersionen der Austenit-Phasen von Ni_2MnGa und $Ni_{49}Mn_{32}Ga_{19}$ liegen beide in der selben Frequenzregion. Die optischen Moden von $Ni_{49}Mn_{32}Ga_{19}$ zeigen eine flachere Verteilung,

die auf die unterschiedliche Besetzung mit überzähligen Mangan Atomen zurückzuführen ist. Der größte Unterschied in der gesamten Phonendispersion wurde für die $TA_2[\xi\xi 0]$-Moden der stöchiometrischen und nicht-stöchiometrischen Zusammensetzungen gefunden. Im Fall von Ni_2MnGa zeigt die $TA_2[\xi\xi 0]$-Mode eine starke Aufweichung mit ihrem Zentrum bei $\xi = 0.33$ r.l.u. Die nicht-stöchiometrische Zusammensetzung hingegen zeigt eine weniger ausgeprägte Aufweichung und hat ihr Zentrum um $\xi = 0.27$ r.l.u.

Der Effekt der Temperatur auf die $TA_2[\xi\xi 0]$-Moden wurden sowohl für die stöchiometrischen als auch für die nicht-stöchiometrischen Zusammensetzungen untersucht, wobei sich ein ähnliches, lineares Verhalten zeigte. Das Quadrat der Phonenfrequenzen weicht bei der Annäherung an die strukturelle Übergangstemperatur von beiden Seiten auf, ohne auf Null abzufallen. Es wurde kein signifikanter Sprung der weichen Phononenmoden bei der strukturellen Übergangstemperatur entdeckt. Die beobachtete Anomalie der $TA_2[\xi\xi 0]$-Moden von Ni-Mn-Ga-Legierungen wurde mit der Literatur verglichen, wobei ähnliche martensitische Übergänge beobachtet wurden. Die Elastizitätskonstanten wurden aus den Anfangssteigungen der akustischen Moden für beide Zusammensetzungen berechnet. Die Ergebnisse der Elastiziätsmodule C' zeigen, dass Scherung im Fall von Ni_2MnGa keine Rolle für den prä-martensitischen Phasenübergang spielt. Für $Ni_{49}Mn_{32}Ga_{19}$ zeigten die Elastizitätkonstanten C' eine Temperaturabhängigkeit, was einen Hinweis auf einen Einfluss der Scherung auf den Martensit-Phasenbergang darstellt.

Die Vibrationseigenschaften der Tieftemperatur-Martensitphasen der 5M und nicht modulierten (NM) Struktur wurden für $Ni_{50}Mn_{29}Ga_{21}$ und $Ni_{50}Mn_{30}Ga_{20}$ gemessen. Die gesamten Phononen Dispersionsmessungen der Martensit-Phasen zeigen, dass die optischen Moden in einem ähnlichen Frequenzbereich liegen wie die der Austenitphase. Die beobachtete Aufweichung in der $TA_2[\xi\xi 0]$-Mode ist in der Martensit-Phase ausgeschmiert, aber dennoch vorhanden. Zusätzlich wurden Anregungen, bedingt durch die Modulationen, in der $[\xi\xi 0]$-Region bei niedrigen Frequenzen unter 1 THz gefunden. Diese Anregungen wurden mit denen der prä-martensitischen und martensitischen Phasen der stöchiometrischen Proben verglichen. In der 5M Phase traten zusätzlich zu den niederfrequenten Anregungen entsprechende Überstruktur-Bragg-Maxima auf. Ni_2MnGa zeigte zusätzlich sowohl kommensurable ($\xi = 0.33$ r.l.u.) als auch nicht-kommensurable ($\xi = 0.43$ r.l.u.) elastische Streumaxima, jeweils in der Vormartensit- und Martensitphase. Diese nieder-frequenten Anregungen in Ni_2MnGa wurden auf Ladungsdichtewellen (charge density waves, CDWs) zurückgeführt. In der nicht-stöchiometrischen 5M Martensitphase wurde kein Hinweis auf CDWs gefunden.

Die Stabilisierung der Austenit-Phasen und die treibenden Kräfte für den strukturellen Übergang wurden mittels Rechnungen zur Entropie untersucht. Diese Berechnungen zeigen, dass die Gitterentropie alleine nicht ausreicht, um die Austenit-Phase zu stabilisieren oder den Martensit-Phasenübergang zu verursachen. Die magnetischen und elektronischen Entropien spielen eine wichtige Rolle für die Übergangs- und Phasenstabilisierungseigenschaften von Ni-Mn-Ga-Legierungen.

Contents

Chapter 1

Introduction

In early 20th century the term “Heusler alloy” was introduced after the discovery of the ferromagnetic Cu-Mn-Al alloy by Frederic Heusler. In general, Heusler alloys are defined as ternary inter-metallic compounds with the chemical composition of stoichiometric X_2YZ and the crystallographic face centered cubic $L2_1$ structure. The offstoichiometric compositions of these types of ternary alloys are also referred as Heusler alloys. High temperature face centered cubic structures of these materials are named “austenite” due to the similarities of the $L2_1$ phase with the gamma phase of iron. The gamma phase of iron is called “austenite” in honor of Sir William Chandler Roberts-Austen. Heusler alloys show first order, diffusionless structural transformations from the austenite phase to a low temperature, low-symmetry phase which is named “martensite”. The term “martensite” is used to define the displacive transformation in any crystallographic structure and named after German metallurgist Adolf Martens, who investigated different types of steel in the late 19th century. The product phases of these kind of transitions are also named “martensite“.

Some of the Heusler alloys are able to recover from high stresses during the structural transition from austenite to martensite and/or vice versa. This stress recovery is known as shape memory effect and alloys which show this effect are called shape memory materials. It is possible to trigger the structural transition with different external parameters such as temperature, mechanical stress or, for ferromagnetic materials, magnetic fields. If an external magnetic field is used for the shape memory effect, the phenomenon is referred to as ”magnetic shape memory (MSM)“. MSM materials are promising candidates for smart material applications, like actuators and sensors due to their unique properties mentioned above will be addressed in this thesis.

Ni-Mn-based Heusler alloys attracted scientific interest after the discovery of high stress recovery in the $Ni_{2+x}Mn_{1-x}Ga$ alloy [UHK+96]. Many of the Ni-Mn-X alloys undergo a martensitic transformation as a function of temperature for different compositions [PMA09]. Some of the Ni-Mn based alloys show a martensitic transformation in a wide range of composition. Also the magnetic properties of these materials strongly depend on the chemical composition. In general, magnetic and structural properties of different Ni-Mn-Ga compositions are investigated in a very wide variety of methods. The room temperature crystallographic structure of the stoichiometric Ni_2MnGa has been initially investigated by P.J. Webster *et al.* [WZTP84]. Also the martensitic transformation properties and the magnetic properties have been investigated by means of magnetization, optical microscopy, x-ray and neutron diffraction measurements. In the late 20th century A. González-Comas *et al.* investigated the pre-martensitic and martensitic transition properties of stoichiometric Ni_2MnGa by using ultrasonic techniques [GCOM+99]. Especially the premartensitic transition properties of Ni_2MnGa have been investigated in detail with different methods [ZSW98, VBK+99, KTB+01, WCG+01, CPSC02, PMA09]. Additionally to these investigations, the vibrational properties of stoichiometric Ni_2MnGa have been studied by inelastic neutron scattering [ZSW+95, ZSWT96, SVKL97, SVK00, MPZ+01, CPS03].

Figure 1.1 shows an example of observed phonon softening at the $TA_2[\xi\xi0]$ phonon mode of stoichiometric Ni_2MnGa. Here the anomalous softening in the $TA_2[\xi\xi0]$ phonon mode has been observed for the first time by Zheludev *et al.* [ZSW+95]. Structural characterization of austenite and martensite phases of Ni-Mn-Ga alloys have been investigated by using x-ray and neutron diffraction methods [PCSC00, RAC+06, RAP+07, RAV+08]. Shape recovery properties of Ni-Mn-Ga ferromagnetic shape memory alloys are strongly coupled to the crystallographic structure of the low temperature marteniste phase. The conventional shape recovery can be observed in all possible martensite phases of Ni-Mn-Ga alloys while the magnetic shape memory effect is only observable in modulated martensite phases. For the offstoichiometric compositions of Ni-Mn-Ga alloys, shape recoveries of up to 10% and 6% have been observed in the 7-layered and 5-layered modulated martensite phases, respectively [SLLU02, MMA+00].

It has been reported that, the marteniste phase stability of Ni-Mn-Ga alloys is related with the valence electron per atom (e/a) ratios of the materials [LSS+04]. The effect of e/a on the structural and magnetic transition temperatures of Ni-Mn-based Heusler alloys has been shown by Planes *et al.* [PMA09]. The e/a dependences of the lattice instabilities of the austenite phases have been theoretically and experimentally investigated on Ni_2MnGa [ZAER06] and Ni_2MnAl [MNP+08], respectively. All of these studies show a strong effect of valence electron concentration on the physical properties of ferromagnetic Heusler alloys.

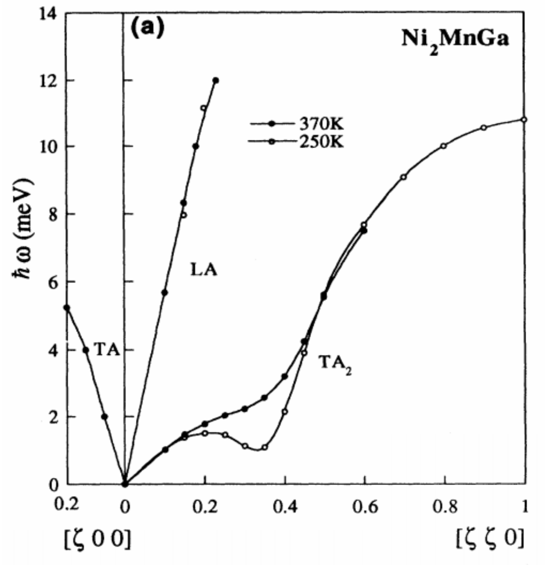

Figure 1.1: *First acoustic phonon measurements on Ni_2MnGa shape memory alloy. A softening is observed only at the TA_2 phonon branch in [110] direction. The figure is taken from [ZSW⁺95].*

As shown in Figure 1.1 vibrational properties of Ni-Mn-Ga alloys show a softening behavior in a particular phonon mode. Similar features have been observed in Ni-based binary systems like Ni-Ti [SSSW84] and Ni-Al [ZH92, SLN$^+$86]. The Ni_xAl_{1-x} alloys show martensitic phase transformation. Related to these transitions the corresponding low lying transverse phonon branch along [110] direction softens [ZH92]. Similar to Ni-Mn-Ga systems Ni-Ti alloys show premartensitic transformations [SPH71]. In Ni-Ti alloys, similar to near stoichiometric Ni-Mn-Ga compositions, superstructure elastic peaks are observed at $\xi=[\frac{1}{3},\frac{1}{3},0]$, which are attributed to the formation of charge density waves. Unlike the stoichiometric Ni_2MnGa alloy, additional to the $[\frac{1}{3},\frac{1}{3},0]$ superstructure peak, the $[\frac{2}{3},\frac{2}{3},0]$ peak is also observed in the Ni-Fe system [SSSW84]. Phonon softening which is observed in Ni-Al and Ni-Ti systems is attributed to the electron-phonon interaction with the Fermi surface nesting. A similar situation is observed in Ni-Mn-Ga systems. Basic theories for binary systems predict a relation between charge density waves and the $[\xi\xi0]$ longitudinal phonon branch [SSSW84]. The softening in the longitudinal acoustic branch is called "Kohn anomaly“ and generally observed in transition metals.

Stoichiometric and most of the offstoichiometric compositions of Ni-Mn-Ga alloys undergo a structural transition in the ferromagnetic phase. Due to this, Ni-Mn-Ga alloys are promising candidates for the ferromagnetic shape memory applications. The vibrational properties of Ni_2MnGa have been investigated by Zheludev *et al.* using inelastic neutron scattering [ZSW$^+$95]. At room temperature, a softening is observed at the TA$_2$[$\xi\xi0$] phonon branch around $\xi = 0.33$ r.l.u. The relation between the softening and the magnetic transition has been investigated by different groups [ZSW$^+$95, ZSWT96, SVKL97, MPZ$^+$01]. Offstoichiometric compositions of Ni-Mn-Ga alloys also show a ferromagnetic shape memory effect and the vibrational properties of these materials are not investigated in detail. In literature it is possible to find partial investigations of vibrational properties of offstoichiometric Ni-Mn-Ga for a Ni-rich composition [MPZ$^+$01]. As the compositional change strongly effects the shape memory properties, it is essential to investigate the vibrational properties of a system which shows one of the highest ferromagnetic shape memory effect (MSE) and which is used as a prototype material for the technical applications.

Besides these investigations found in literature, Ni-Mn-Ga alloys still have lots of interesting questions waiting to be answered. This study is aimed to find answers to some of these questions. One of the most interesting question in MSE alloys arises in the compositional dependence of the physical properties. It has been shown in the literature that the compositional changes affect the physical properties of these materials but the effect on vibrational properties is still a subject to be investigated. In this study we will try to find answers to this interesting question. In literature, there are multiple theoretical studies which query the driving forces of the structural transitions in ferromagnetic shape memory alloys. In this study, we will try to give some experimental support to the theory of the structural transitions. In addition, there is a huge lack of information in the vibrational properties of the Ni-Mn-Ga alloys in the martensite phase. For the first time, we were able to measure the martensite phase phonons of modulated and non-modulated marteniste phases of Ni-Mn-Ga alloys to eliminate this lack of knowledge.

In this work vibrational properties of Ni-Mn-Ga alloys are investigated in detail. In Chapter 2, the basic properties of the martensitic transition and its relation to the shape memory effect is explained. In Chapter 3, experimental procedures of sample characterization and phonon measurements are explained. In Chapter 4, fundamental theoretical models of the lattice dynamics are discussed. Classical and quantum theory of the lattice dynamics are shown and the used models are defined briefly. The results of the sample characterization are shown in Chapter 5. The chemical compositional analysis, magnetic and structural transition properties are presented. Elastic neutron scattering measurements of offstoichiometric alloys are also shown. A detailed investigation of the vibrational properties of Ni-Mn-Ga alloys is presented in Chapter 6. In this chapter, vibrational properties are presented for both austenite and martensite phases. Austenite phonon dispersions of stoichiometric and offstoichiometric compositions are presented with corresponding Born-von Kármán model fits. The effect of temperature change on the softening properties of the $TA_2[\xi\xi0]$ branch is also shown in this chapter. Pre-martensite phase measurement of Ni_2MnGa and martensite phase measurements of different offstoichiometric compositions are presented. In Chapter 7, the results are discussed and compared to literature. Finally, a summary and an outlook are presented in Chapter 8.

Chapter 2

Heusler Alloys and Shape Memory Effect

2.1 Heusler Alloys

Heusler alloys are ternary inter-metallic compounds which have a X_2YZ composition for full- and a XYZ composition for half-Heusler structure. These alloys show an open body-centered cubic (bcc) structure which is only stable at very high temperatures. Due to the kinetic reasons at low temperatures the open bcc structure transforms to different ordered structures like B2 and $L2_1$. The B2 phase has a bcc structure and for Heusler alloys due to the occupancies of the atoms in the unit cell, it is named as disordered phase. In B2 phase, atoms at the Y and Z positions are randomly distributed which causes the disorder. In the case of $L2_1$ phase, the atomic occupancies are well defined for all constituent atoms. Figure 2.1 shows the general $L2_1$ high temperature crystallographic structure of a full Heusler alloy. The $L2_1$ has a face-centered cubic structure with the space group of $Fm\bar{3}m$ (Space group number: 225) [WZTP84]. Due to this high order of the atoms, the $L2_1$ Heusler structure can be characterized by four inter-penetrating face centered cubic lattices as shown in Figure 2.1. In the basic unit cell of $L2_1$ only four atoms exist and the positions are shown in Table 2.1.

Generally the order of the system is defined by these atomic positions. A disorder occurs usually in the offstoichiometric compositions. In the stoichiometric compositions of Heusler alloys, it is also possible to observe disorder due to misoccupations of the atomic sites. The effect of disorder on properties of Cu_2MnAl and associated alloys has been shown by G. B. Johnston and E. O. Hall in the late 60s [JH68]. The effect of disorder in the fcc lattice of Fe-Pt has been investigated by Kästner *et al.* by means of inelastic neutron scattering [KPS+99]. Here, the $TA_2[\xi\xi0]$ phonon modes of the $Fe_{72}Pt_{28}$ have been

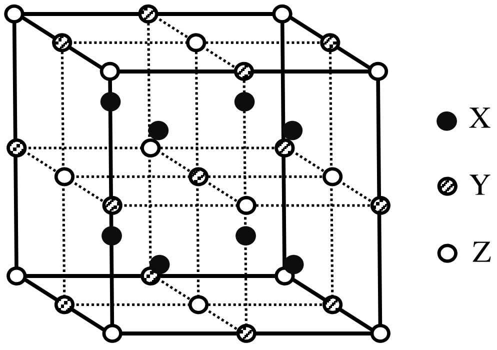

Figure 2.1: *Representation of high temperature face centered cubic full Heusler ($L2_1$) structure [WZTP84].*

Table 2.1: Atomic coordinates and positions of a full-Heusler structure.

Atom	a/x	b/y	c/z	Wyckoff position
X_1	0.25	0.25	0.25	8c
X_2	0.75	0.75	0.75	8c
Y	0.5	0.5	0.5	4b
Z	0	0	0	4a

investigated for both $L1_2$ ordered and disordered fcc systems. The results show that in the $L1_2$ ordered system a strong softening has been observed as a precursor effect of the structural transition. In the disordered system, the softening has been observed in the low ξ region of the Brillouin zone with a very small amplitude. The disorder parameter for the $L2_1$ structure is defined as a misoccupancy of Y and Z sites which is also known as $L2_1$-B2 disorder. The crystallographic structure of B2 is the same as $L2_1$ except the difference in the occupancy of Y and Z sites. In the B2 structure the occupancy of the Y and Z positions are random which is not the case for the $L2_1$ phase. The ratio of the $L2_1$-B2 disorder can be controlled by applying a proper heat treatment to the samples.

2.2 Martensitic Transformations

Martensitic transformations are shear dominant displacive, diffusionless first order solid state structural transformations. The atomic movement during the structural transformation is smaller than the interatomic distances. The first observation of the martensitic transition and structure are carried out by German metallurgist Adolf Martens using stainless steel. Additional to steel, austenite and martensite transformations occur in a very wide range of materials. The martensite transformation occurs as a nucleation and growth process. During the growth process, the growth directions are perpendicular to habit planes. Habit planes are special crystallographic planes which have the same atomic ordering in both austenite and martensite phases. Figure 2.2 shows a schematic representation of a habit plane between austenite and martensite phases and the growth direction of the martensite.

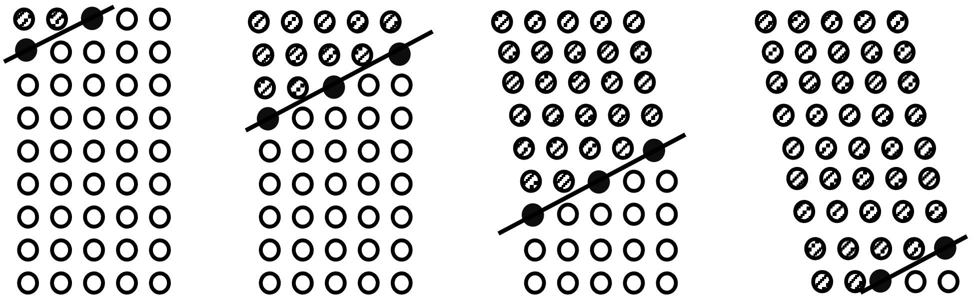

Figure 2.2: *Schematic representation of a habit plane and growth process of the martensite phase into the austenite phase. Open circles represent the austenite phase, line-filled circles represent the martensite phase and the full circles represents atoms in the habit plane. Solid line is guide for the eye which represents the habit plane.*

Another important feature of the martensitic transformation is the hysteresis which is observed during the structural transition. Thermal hysteresis is observed in all of the temperature dependent measurements of the martensitic transformations. The temperature dependent measurements of physical properties like magnetization, resistivity, heat capacity etc. show thermal hysteresis around the martensitic transformation temperature [Mar95, AMP11]. The critical temperatures of martensitic transformation start (M_s), martensitic transformation finish (M_f), and austenitic transformation start (A_s), austenitic transformation finish (A_f) are generally determined from these temperature dependent measurements. The determination of the critical temperatures is schematically shown in Figure 2.3.

Martensitic transitions in the Heusler alloys generally occur as a Bain transformation. Figure 2.4 shows the Bain transformation dominated structural transition of a full-Heusler alloy. In general, a Bain transformation is defined as the crystallographic deformation of body-centered structure to a face-centered structure or vice versa [MFM94]. In the high temperature austenite phase, all of the X atoms are located in the corners of the unit cell. Y and Z atoms are occupying the atomic positions in the centers of these unit cells. During the structural transition from cubic to tetragonal structure the axes of the unit cell shrink or expand. In the middle image of Figure 2.4, the shrunk state is represented.

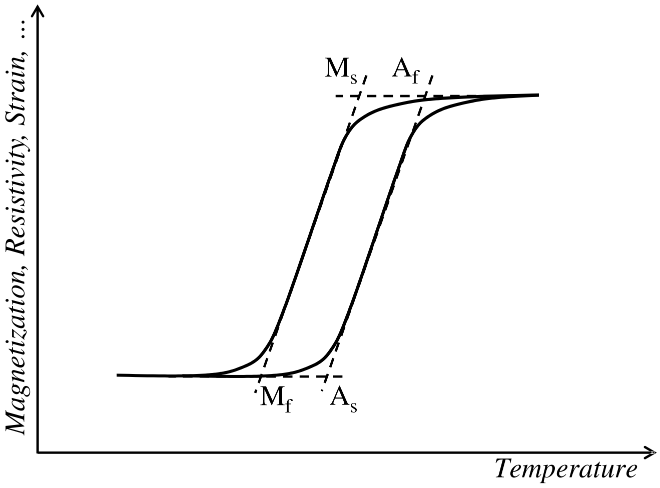

Figure 2.3: *Schematic representation of a thermal hysteresis around the structural transition temperature. Determination of the critical temperatures are indicated in figure.*

The unit cell of the tetragonal phase is shown as a red rectangular prism. The right hand side image shows the unit cell of the tetragonal phase with new unit cell parameters. In the tetragonal phase as in the cubic phase, X atoms occupy the corners of the unit cells but the Y and Z atoms sit in the face centers. This Bain transformation creates a volume change in the unit cell which creates huge strain during the structural transition [SHSS11]. To reduce the emerging structural stress, the material creates twin structures (modulated structures) in the martensite phase.

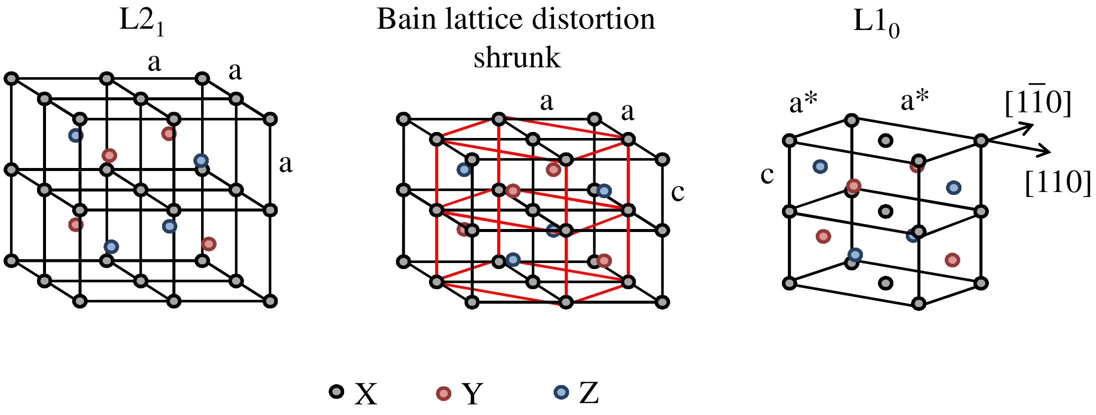

Figure 2.4: *Bain transformation driven structural transition of a full-Heusler structure from cubic austenite to tetragonal martensite structure. Black circles represent X atoms, red circles and blue circles show the Y and Z atoms, respectively.*

Figure 2.5 shows the most commonly observed modulated martensitic structures of Ni-Mn-Ga alloys. Figure 2.5a shows the top view of the $L1_0$ non-modulated tetragonal (NM) structure in the (001) plane. In this non-modulated structure there is no modulation of (110) planes perpendicular to the [1$\bar{1}$0] direction. Two possible 5-layer modulated martensite structures of Ni-Mn-Ga are shown in Figure 2.5b and Figure 2.5c which represent the modulated orthorhombic (5O) and monoclinic (5M) structures, respectively. Figure 2.5d shows the 7-layer modulated (7M) martensitic structure. Additionally to these common martensite phases, other tetragonal, monoclinic and orthorhombic phases are rarely observed in the marteniste phase of Ni-Mn-Ga alloys. In recent years, the growth processes of different modulated structures and the details of the martensite phases have been investigated by means of diffraction methods [Rol11].

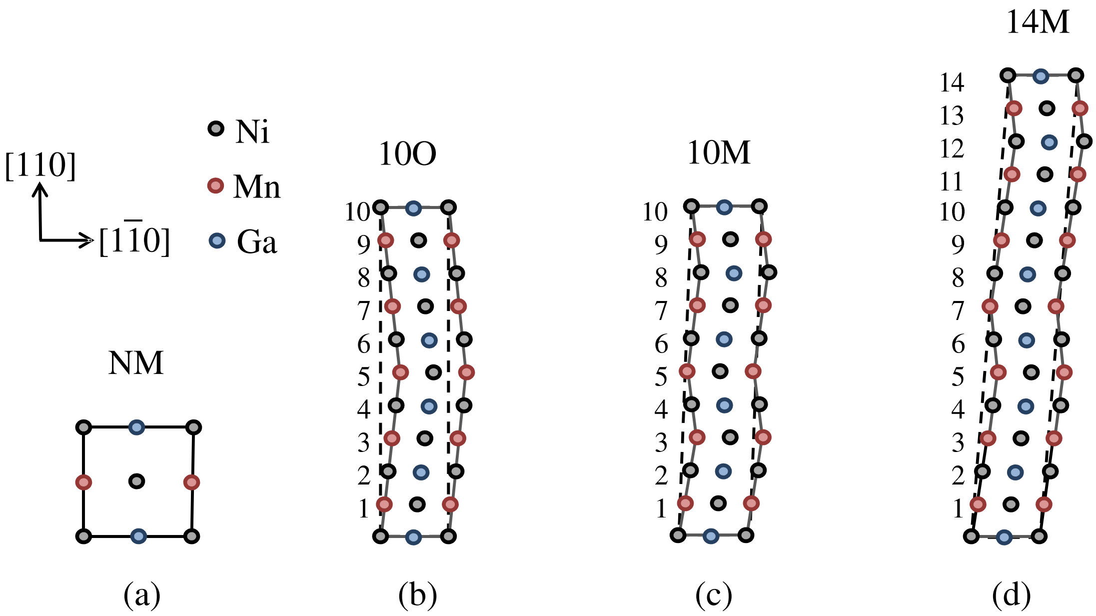

Figure 2.5: *Most common martensitic structures of Ni-Mn-Ga alloys. (a) non-modulated tetragonal structure, (b) 10 (or 5) layer modulated orthorhombic structure, (c) 10 (or 5) layer modulated monoclinic structure and (d) 14 (or 7) layer modulated monoclinic structure. The modulated structures are occurring with the shearing (or shuffling) of the (110) planes in [1$\bar{1}$0] direction.*

Aforementioned structural transition properties of Ni-Mn-based alloys are strongly related with the compositional changes of these alloys. For many of the ferromagnetic shape memory alloys, it is possible to tune the structural and magnetic properties by changing the chemical composition or in other words changing the valance electron per atom (e/a) ratio. Figure 2.6 shows the structural and magnetic transition temperatures of different NiMn-based alloys as a function of e/a ratio.

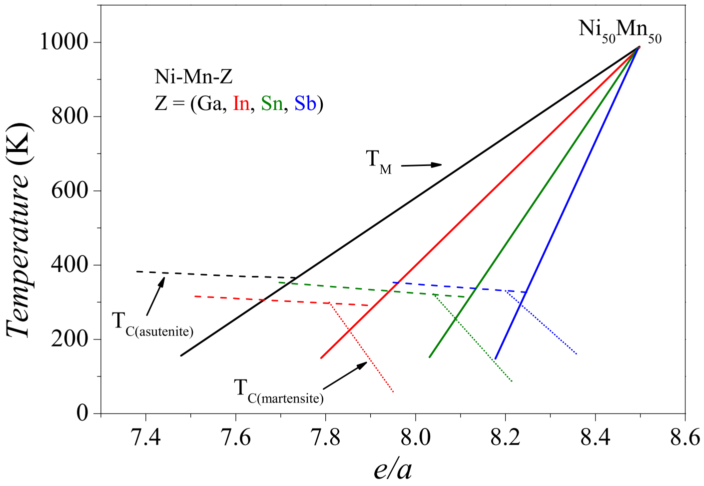

Figure 2.6: *Phase diagram of NiMn-based ferromagnetic shape memory alloys. Solid lines indicate the structural transition temperatures of the corresponding system. Dashed lines and dotted lines depict the magnetic ordering temperatures in the austenite and the martensite phases, respectively. The figure is adapted from [PMA09].*

It is clearly indicated in Figure 2.6 that, the e/a ratio strongly effects the structural transition temperatures, T_M. T_M of all Ni-Mn-based alloys increase drastically with increasing e/a ratio. Similar to the changes in the structural transition temperatures, in the case of indium, antimony and tin, the magnetic ordering temperatures in the martensite phases decreases strongly with increasing e/a ratio. Additionally, the austenite phase Curie temperatures do not change so much. The study of Lanska *et al.* showed that the crystallographic structures of the martensite phases of Ni-Mn-Ga alloys are related to the e/a ratios [LSS+04]. The NM marteniste phase has been observed mainly for the e/a ratios higher than 7.67 and modulated martensite phases have been observed in the e/a interval of $7.61 < e/a < 7.71$. These investigations show the strong influence of e/a-ratio on the structural transition properties and the magnetic properties on the martensite phase.

2.3 Shape Memory Effect (SME)

The recovery from the high stresses during the martensite to austenite structural transition is called shape memory effect (SME). For conventional shape memory materials, this effect occurs after heating the mechanically deformed martensite to the austenite phase. Around 100% shape recovery of the deformation occurs in the heating process. There are two main types of SME: The first type is the “conventional SME” and the second type is the “magnetic SME”. In the conventional shape memory materials the deformation is generally caused by an external mechanical stress and the recovery is provided by the heating the sample to the austenite phase.

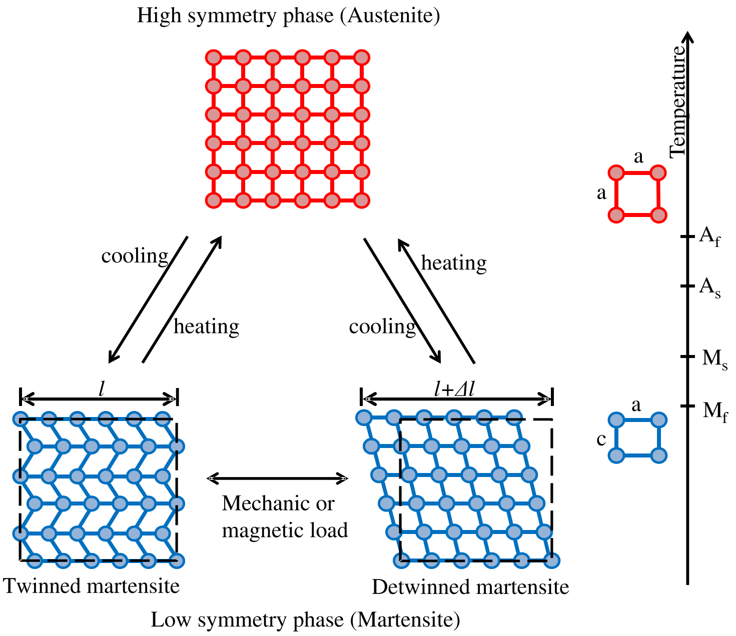

Figure 2.7: *Schematic representation of the shape memory effect in general.*

Figure 2.7 shows the fundamental explanation of the conventional shape memory effect. The right hand side arrow indicates the temperature axis and the critical structural transition temperatures are marked as they were defined in Chapter 2.2. When the material is cooled below the M_s temperature the martensitic structural transition starts and ends at M_f. When the material is heated up above the A_f temperature it fully transforms to the austenite structure again. During this structural transition no macroscopic shape change is observable which is just due to the twinned (modulated) structure of the martensite phase. When a mechanical load is applied to the twinned martensite, twin boundaries move easily and create a macroscopic shape change on the material (named as detwinned martensite in Figure 2.7). In this plastic-like mechanical deformation state, after the removal of the external stress, the material keeps its shape without any recovery. When the material is heated up, the structural recovery starts at the temperature A_s and the material recovers from the plastic-like deformation perfectly until above A_f. This whole deformation and recovery cycle is generally called “conventional one-way shape memory effect” because the material only remembers its original shape in the austenite phase. In the one-way shape memory effect, one has to deform the material after each cooling cycle to create a detwinned martensite phase.

2.3.1 Magnetic Field Induced Shape Memory Effect

As mentioned in the previous section, the detwinning can be driven not only by a mechanical load but also by the external magnetic field. To observe the magnetic field induced shape memory effect, the material has to be in the ferromagnetic order which creates a magnetic anisotropy. When a magnetic field is applied to a ferromagnetic shape memory material two different features may occur. First, the structural transition can be triggered by the external magnetic field, or second, in the marteniste phase single variant state can be formed due to the magnetic anisotropy. As briefly explained, the magnetic field induced shape memory effect is observable in two different ways which are the magnetic field induced structural transition (MIT) and the magnetic field induced variant reorientation (MIR).

2.3.1.1 Magnetic Field Induced Structural Transition - MIT

The working principle of the magnetic field induced structural transition (MIT) is similar to the conventional shape memory which is explained in Chapter 2.3. In MIT, the external field is used as the trigger mechanism for the shape memory effect instead of mechanical load and temperature. In ferromagnetic shape memory materials it is possible to change the structural transition temperature just by applying an external magnetic field. The magnetic field stabilizes the phase which has a higher magnetization. Due to this stabilization, the structural transition temperature can shift to lower or higher temperatures depending on the magnetization of the austenite and martensite phases.

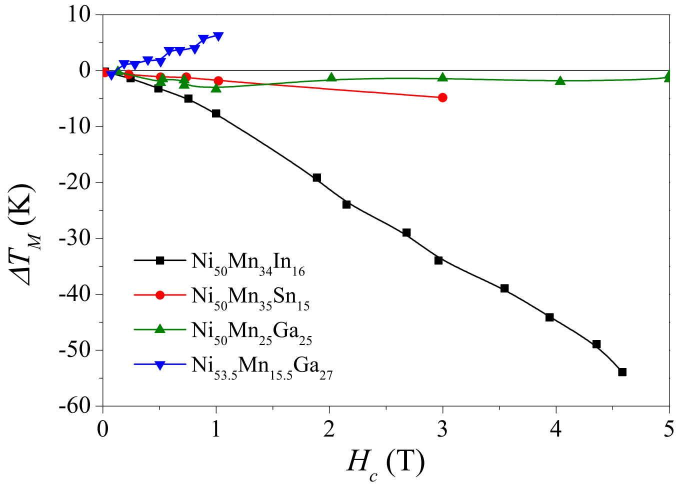

Figure 2.8: *The change of the martensitic transformation temperatures as a function of applied magnetic field for different Ni-Mn-X alloys. The figure is taken from [PMA09].*

The change of the martensite start temperature is shown for different Ni-Mn-based alloys in Figure 2.8 [PMA09]. For Ni-Mn-Sn and Ni-Mn-In alloys an external magnetic field causes a decrease in the martensite transition temperature which shows that the magnetization in the austenite phase is more favorable compared to the martensite phase. In the stoichiometric Ni_2MnGa alloy external magnetic fields up to 5 Tesla have no significant effect on the martensite transition temperature. The change in the temperature is in the order of 1-3 K/T. In the offstoichiometric $Ni_{53.5}Mn_{19.5}Ga_{27}$ composition, the martensit transition temperature increases strongly when applying an external magnetic field (approx. 8K/T). This huge effect gives a strong clue about the relation between the magnetization and the structural stability.

2.3.1.2 Magnetic Field Induced Variant Reorientation - MIR

Fundamentals of the magnetic field induced variant reorientation (MIR) are based on the relation between the magnetic ordering and the crystallographic structure. In the martensite phase the crystallographic c-axis (the short axis) is the easy axis of the magnetization. This magnetic easy axis and the structural c-axis are magnetostructurally coupled and move together. If the twin boundary mobility is high enough for the material, it is possible to remove the twin boundaries just by applying an external magnetic field. The mobility of the twin boundaries allows for minimization of the Zeeman energy which is created by the magnetic field.

The magnetic energy of a material can be written as the sum of Zeeman and magnetocrystalline anisotropy energies [AMP11]:

$$E_{mag} = -\mathbf{M} \cdot \mathbf{H} - K_u(\frac{\hat{u} \cdot \mathbf{M}}{M_s})^2 \tag{2.1}$$

where, $\mathbf{M}$ is the magnetization and has the form of $\mathbf{M} = M_s(\hat{h} sin\theta + \hat{k} cos\theta)$ (M_s is the saturation magnetization), $\mathbf{H}$ is the external magnetic field, $\hat{u}$ is the unit vector along the easy axis direction and K_u is the anisotropy.

When two different variants are considered, the Zeeman energy difference between these two variants is the driving force for the variant reorientation. To observe a twin boundary motion in between these two variants, the magnetic energy difference in between has to fulfill following condition,

$$\Delta E_{mag} > \epsilon_0 \sigma_{tw}. \tag{2.2}$$

Here, ϵ_0 is the lattice distortion ($\epsilon_0 = 1 - c/a$, where a and c are the unit cell parameters) and σ_{tw} is the twinning stress. In the case of magnetic saturation, all of the magnetic moments will align parallel to the external field and the difference of the Zeeman energies between two variant vanishes ($M_S \cdot H \gg K_u$). In this case, from the equation 2.1, ΔE_{mag} coincides with K_u and equation 2.2 changes to the following form [AMP11]

$$\frac{K_u}{\epsilon_0} > \sigma_{tw}. \tag{2.3}$$

When the twinning stress, σ_{tw}, is smaller than the magnetic stress, $\frac{K_u}{\epsilon_0}$, a magnetic field induced strain occurs.

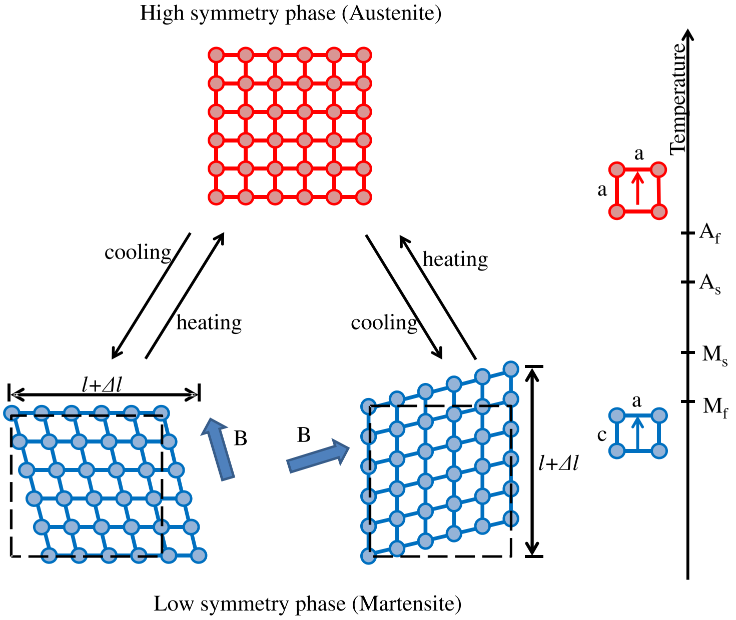

Figure 2.9: *Schematic representation of the Magnetic field Induced variant Reorientation (MIR).*

Figure 2.9 shows the schematic representation of the magnetic field induced variant reorientation. For the observation of the MIR effect, the material has to be in the martensite phase with a modulated structure. In Figure 2.9 the thick blue arrow, labeled as B, represents the direction of the applied external magnetic field. In the martensite phase due to the minimization of the energy, all of the magnetic moments will align parallel to the field as a whole domain. When the direction of the external magnetic field is changed, the magnetic structure of the material will follow it. In the figure, the magnetic field is rotated by 90° (in clockwise direction). The change in the direction of the external magnetic field creates a strain in the material and ferromagnetic shape memory materials are able to overcome this high stress due to their unique properties.

2.4 Ni-Mn-Ga Alloys

Among the investigated shape memory materials, NiMn-based alloys have a special place. Especially Ni-Mn-Ga has been investigated intensively due to its promising magnetic and structural properties. Offstoichiometric compositions of $Ni_{2+x}Mn_{1+y}Ga_{1-x-y}$ show strains up to about 10% in the martensite phase. As reported in literature, the ferromagnetic shape memory effect strongly depends on the existence of modulated phases in the martensite phase. For Ni-Mn-Ga systems, commonly modulated martensite phases are sketched in Figure 2.5. The magnetic shape memory effect is only observable in the five-layered (5M or 10M/10O) and seven-layered (7M or 14M) martensite phases. In the non-modulated (NM) martensite phase, strengths of the external magnetic fields up to 5 Tesla are not enough to observe the magnetic shape memory effect, but this does not mean that the NM phase does not show a shape memory effect at all. In the NM martensite phase Ni-Mn-Ga alloys are able to recover mechanical stresses up to 20% [JLX+02].

Structural properties of the Ni-Mn-Ga alloys have been investigated in literature. The high temperature high symmetry austenite phase has been investigated by Webster *et al.* in 1984, which shows a face-centered cubic $L2_1$ structure [WZTP84]. Modulated martensite phases of Ni-Mn-Ga alloys have been intensively investigated by Righi *et al.* using diffraction techniques [RAC+06, RAP+07, RAV+08, RAP+09]. Magnetic and structural transition properties are also investigated by different groups to understand the magneto-structural transition properties of Ni-Mn-Ga systems. The advantage of the NiMn-based shape memory materials is the tunability of the structural and magnetic transition properties. Figure 2.10 shows the well known phase diagrams of the $Ni_{2+x}Mn_{1-x}Ga$ [EBK+06] and $Ni_2Mn_{1+x}Ga_{1-x}$ [EBG+08] for magnetic and structural transition temperatures. Beside these studies, it has been shown by Schlagel *et al.* that the chemical composition of the Ni-Mn-Ga strongly effects the solidification, liquefaction, martensite transition and Curie temperatures [SWZL00]. The compositional dependence of the martensite phases and the unit cell parameters have been shown by Lanska *et al.* and Richard *et al.* [LSS+04, RFS+06]. Additionally to these above mentioned investigations, it is possible to find numerous studies investigating the relation between chemical composition and structural and magnetic transition temperatures.

Figure 2.10a shows the change of the critical temperatures of Ni-Mn-Ga alloys for nickel rich and manganese deficient compositions. The substitution of nickel with manganese increases the martensite transition temperature. In the shown composition region, the premartensite transition temperatures stay constant and the magnetic ordering temperature decreases. In Figure 2.10b the effect of manganese-gallium substitution on the

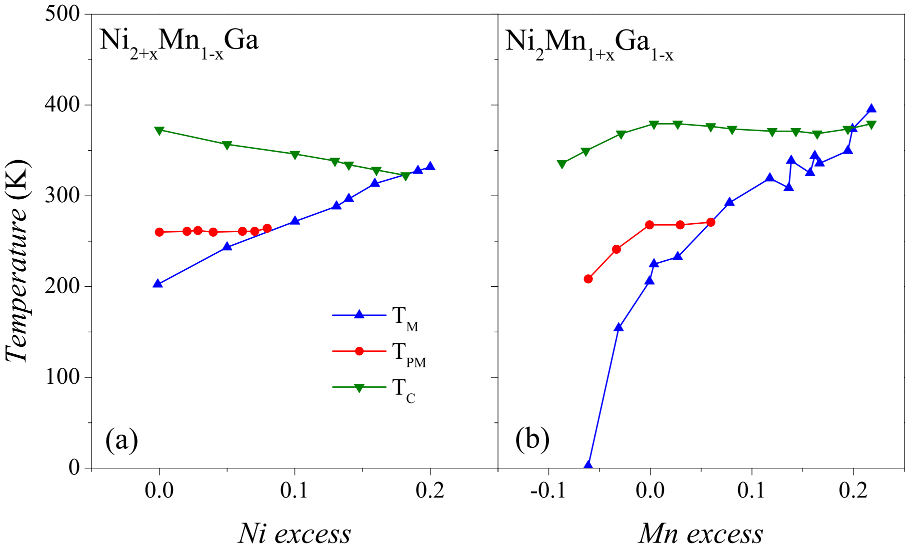

Figure 2.10: *Structural and magnetic transition temperatures of (a)$Ni_{2+x}Mn_{1-x}Ga$ and (b) $Ni_2Mn_{1+x}Ga_{1-x}$ as a function of compositional change [EBK+06, EBG+08]. Blue up triangles represent the martensit transition temperatures, red circles show the pre-martensit transition temperatures and green down arrows correspond to the magnetic ordering temperatures.*

critical temperatures is shown. In the manganese rich region, the concentration increase of manganese does not effect the magnetic ordering temperature nor the premartensite transition temperature but the martensite transition temperature changes drastically. In the manganese deficient region of the phase diagram, all of the critical temperatures decrease and the martensite transition vanishes in low manganese concentrations x below -0.06. In addition, the structural and magnetic properties of $Ni_{50}Mn_{25+x}Ga_{25-x}$ [JMD+04] and $Ni_{50+x}Mn_{25-x}Ga_{25}$ [VBK+99] have been investigated in literature.

Vibrational properties of Ni-Mn-Ga alloys have been investigated after the discovery of the high strains in these alloys. Especially the austenite phase phonon properties of Ni-Mn-Ga alloys have been investigated by different groups [ZSW+95, ZSWT96, SVKL97, SVK00, MPZ+01, CPS03]. In these studies, the main focus is the investigation of the soft $TA_2[\xi\xi0]$ mode as a function of temperature around the magnetic ordering temperature, T_C. Theoretical studies on the vibrational properties of the Ni_2MnGa alloy show that the experimentally observed softening in the $TA_2[\xi\xi0]$ phonon mode is strongly correlated to the magnetic properties. Similar to the experimental observations, first-principles calculations show soft phonon in the $TA_2[\xi\xi0]$ phonon mode at absolute zero temperature

[BRC03, ZEB04, EBK+06, UHN+09].

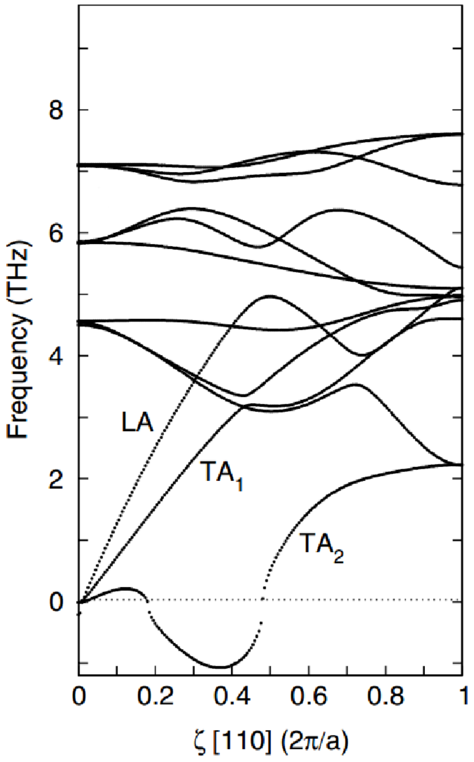

Figure 2.11: *Calculated phonon dispersion of stoichiometric Ni$_2$MnGa composition with propagation in [110] direction at absolute zero temperature. Phonon modes are shown for the first Brillouin zone in the [110] direction of the L2_1 structure. Figure is taken from [EBK+06].*

Figure 2.11 shows an example of a calculated phonon dispersion for stoichiometric Ni$_2$MnGa alloy at absolute zero temperature. The calculations of the [110] direction show imaginary phonon frequencies in a particular region of the TA$_2$-mode. These imaginary phonon frequencies indicate that the L2_1 structure is not stable at absolute zero temperature and needs to transform to a another crystallographic structure. Due to the limitations of the first-principles, theoretical calculations are only available at absolute zero temperature. To mimic the effect of temperature, it is common to use the magnetization as an external parameter which is strongly related to temperature for the magnetic systems (Stoner approach). A study of Gruner *et al.* shows that the magnetization effects the stability of the austenite phase which concludes the strong relation between magnetism and the structural instabilities in the austenite phase [GAZ+08].

Chapter 3

Methods

3.1 Sample Preparation

The single crystals used in this study were produced by K. Rolfs and R. Schneider by using a special single crystal growth technique at the Helmholtz-Zentrum Berlin (HZB), Berlin. Crystal growth from a melt is a well established method for single crystal production. Most common ways to grow a single crystal are the well known Czochralski and Bridgman methods. For the growth of the single crystals which are used in this work a modified version of the conventional Bridgman method was used. In the following paragraphs fundamentals of these mentioned methods will be briefly described.

The Czochralski method can be basically defined as pulling the crystal out from a melt. In this process, the material which is going to transform to a single crystal is molten in a crucible and the seed crystal is dipped in this melt. The temperature of the melt is adjusted to partially melt the seed crystal. After dipping the seed crystal in, it is slowly moved away from the melt and this small movement creates a temperature gradient. Due to this temperature gradient the molten material around the seed crystal will crystallize with the same crystallographic structure as the seed. Additionally, the seed crystal can be rotated to homogenize the single crystal. The main disadvantage of the Czochralski method is the requirement of large amount of material for the growth process.

The Bridgman method is mainly based on the movement of the crucible out of the furnace. Compared to the Czochralski method, there is no need of a seed crystal for the single crystal production. In this method, to grow the single crystal, a temperature gradient inside the furnace is necessary. It is possible to obtain this gradient in two different ways, either by moving the crucible away from the heat source or by cooling the furnace slowly. For the Bridgman method, tip shaped crucibles are generally used to obtain the seed crystal at the tip. When the seed crystal has formed, the rest of the crystal grows over this seed crystal. Depending on the number of seed crystals in the melt, single- or poly-crystalline materials can be obtained as a product.

Both of these single crystal growth methods have a common disadvantage for the growth of Ni-Mn-Ga systems, which is the evaporation of manganese due to its high vapor pressure. To overcome this problem, it is possible to use a high pressure noble gas atmosphere. Additional to noble gas atmosphere it is also possible and more efficient to avoid the material loss by burying the molten material under a slag material. This method is called "SLAg Remelting and Encapsulation (SLARE)" technique [RCG$^+$12]. In this technique the molten material is not touching to the crucible directly but floating in a molten slag - see Figure 3.1b. The important point of the SLARE technique is to find suitable slag materials for the alloy. The slag has to be non-reactive to both single crystal and crucible material. For the growth of Ni-Mn-Ga single crystals, CaF_3 and MgF_3 slags were used in YO_2 crucibles. The single crystals used in this study were prepared by SLARE technique, for more details about the SLARE single crystal growth process see [RCG$^+$12].

After the growth, the resulting crystals were annealed in a quartz tube to ensure homogeneity. The annealing of the crystals was carried out in a long thermal sequence. Initially the crystals were heated up to 1273 K and kept at this temperature for 80 hours then the temperature was decreased to 1000 K and held for 2 hours. After these annealing steps the homogenization of the sample was done. After the homogenization, to improve the ratio of $L2_1$ phase in the crystal, further annealing steps were carried out. The temperature of the oven was decreased to 973 K and kept there for 10 hours and then the furnace was cooled to 773 K and held for 20 hours. Finally, the samples were cooled down to room temperature.

After annealing the crystals, to ensure a single variant state in the martensite phase, mechanical training was carried out for the five-layer modulated and non-modulated martensite crystals. Before starting the mechanical training, rectangular prisms were cut from the single crystal rod. The surfaces of the prisms were defined to be parallel to the $\{100\}$ planes of the austenite phase. For the mechanical training, the crystals were mounted in a pneumatic punch device, consisted of a pneumatic cylinder and a brass heating block with two 90 W heating cartridges. The temperature of the heating block was measured with a PT-1000 element and controlled by a Lakeshore temperature controller. The pressure which was applied to the surface of the crystal was controlled by a pressure regulator of a nitrogen bottle.

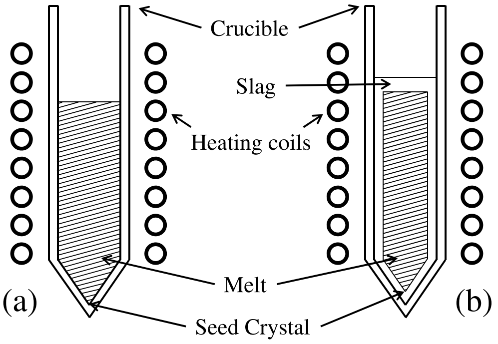

Figure 3.1: *Schematic representations of (a) Bridgman and (b) SLARE single crystal growth processes. The figure is adapted from [RCG+ 12].*

For the phase diagram investigation of Ni-Mn-Ga alloys, approximately 3 - 3.5 g polycrystalline materials were prepared by using a commercial arc melter (Edmund Bühler Arc Melter MAM1) in the Chair of Functional Materials, TUM Physics Department. The melting processes were carried out in a water cooled copper crucible under argon atmosphere. Commercial purity elements were used for the sample preparation (Nickel: 99.97%, Manganese: 99.99% and Gallium: 99.99%). Before starting the melting process the manganese pieces were purified by annealing under continuous vacuum (approx. 10^{-5} mbar) to remove the oxide layer on top of the manganese pieces. The melting processes were repeated 5 times for each polycrystalline material to ensure the homogeneity of the samples. After the repeated melting process, the resultant ingots were annealed in a sealed quartz tube under argon atmosphere for 3 days at 973 K. The resulting ingots were finally quenched in cold water.

3.2 Sample Characterization Methods

3.2.1 Magnetic Measurements

The magnetic properties of Ni-Mn-Ga alloys were investigated by using the Superconducting QUantum Interference Device (SQUID) magnetometer (Magnetic Property Measurement System (MPMS) by Quantum Design) at Universität Duisburg-Essen, Duisburg. The temperature dependent magnetization measurements, $M(T)$, were carried out in three different sequences. For the zero field cooled measurements, ZFC, the sample was cooled from room temperature to 7 K without any external magnetic field and a magnetic field of 5 mT was applied to the sample at low temperature. After the application of the magnetic field, the magnetization was measured up to 380 K under the steady presence of external magnetic field. For the field cooling and field heating measurements, FC and FH, the magnetization was measured in the temperature range of 380 K $\geq$ T $\geq$ 7 K and

7 K ≤ T ≤ 380 K, respectively, without removing the external magnetic field. The magnetic field dependent magnetization, $M(H)$, measurements were carried out isothermally. The $M(H)$ measurements were carried out only during magnetizing the sample.

Besides the magnetic properties, structural transition properties are also deducible from temperature and magnetic field dependent measurements. The thermal hysteresis between the FC and FH measurements generally indicates the first order structural transition in Heusler alloys. The difference between the ZFC and FC measurements gives information about the ferro- and anti-ferromagnetic interaction in the material. Magnetic field induced structural transition information can be acquired directly from magnetic field dependent magnetization measurements.

3.2.2 Calorimetric Measurements

Differential scanning calorimetry (DSC) measurements are one of the fastest and easiest way to determine the first and second order transition properties of materials. The basic working principle of the DSC measurements is based on measuring the heat changes during a constant heating and cooling process. Figure 3.2 shows the setup of a heat flow DSC device in a schematic way. In this setup, the whole system is heated up or cooled down with a constant ramp rate. During a transition, due to the enthalpy change of the sample, the temperature of the sample will stay constant which will create a heat flow from heater to the sample. By measuring these heat transfer values it is possible to characterize the transition properties of materials.

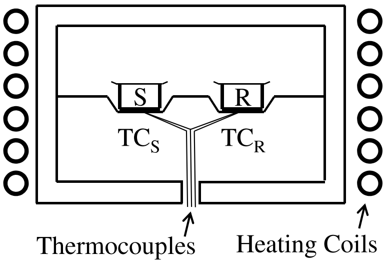

Figure 3.2: *Schematic representation of a heat flux DSC. S and R letters correspond to sample and reference sample cans, respectively.*

By using the DSC, the structural transition temperatures (A_S, A_F, M_S and F_F) and the Curie temperatures (T_C) of Ni-Mn-Ga alloys were determined. DSC measurements of the single crystals were carried out in the temperature range of 173 K ≤ T ≤ 473 K with a heating and cooling rate of 15-20 K/min in a commercial DSC device (Perkin Elmer - DSC 8500) at Forschungs-Neutronenquelle Heinz-Maier Leibnitz (FRM II), Munich. The polycrystalline samples are measured in the wider temperature range due to the high transition temperatures. The high temperature limit for the DSC measurements was 1023 K which is the upper limit of the instrument. But the real temperature limit was defined by the melting temperature of the aluminum sample cans. The measurements up to 873 K were done using sealed aluminum sample cans and the critical transition temperatures were determined from the peak maximum values of the calorimetric measurements.

3.2.3 Chemical Compositional Analysis

The chemical compositions of single- and poly-crystals were determined by energy dispersive x-ray spectroscopy (EDX) using a scanning electron microscope. The measurements were done at the Crystal Laboratory of TUM Physics Department, Munich. The sides of the single crystals were cut along the growth direction and polished with a 1200 grid sand paper. The EDX measurements were done in different spots on these polished surfaces to determine the overall composition of the sample and the compositional gradient along the single crystals. For the EDX analysis of the polycrystalline samples, the alloys were cut into two pieces in the middle and one side of the sample was polished with 1200 grid sand paper. The EDX analysis were carried out at different spots on the polished surfaces to get an overall average on the composition of the polycrystals.

3.3 Neutron Scattering

Elastic and inelastic neutron scattering are unique methods to investigate the structural and vibrational properties of condensed materials. In an elastic measurement, the energy of a neutron does not change after interacting with the sample. In the inelastic case, the energy of the neutron changes due to the creation or annihilation of a quantum state (like phonon and magnon). The energy of a neutron can be formulated as

$$E = \frac{1}{2}mv^2 = \frac{\hbar^2 k_B^2}{2m_N} \tag{3.1}$$

where, $\hbar$ is the reduced Planck's constant, k_B is Boltzmann's constant and m_N is the mass of a neutron.

The energy of a neutron can be measured by determining its wavelength or velocity. Both measurements are widely used in condensed matter research. For the determination of the velocity of a neutron, the time of flight method, TOF, is used. For the wavelength determination, Bragg reflections from single crystals are used. In this work for the determination of energies, wavelengths of the neutrons were measured by using the Bragg reflection laws in a three axis spectrometer.

For understanding the scattering experiments, it is essential to be aware of the concept of real space and reciprocal space. Figure 3.3 shows the relation between the scattering in the real space and the reciprocal place.

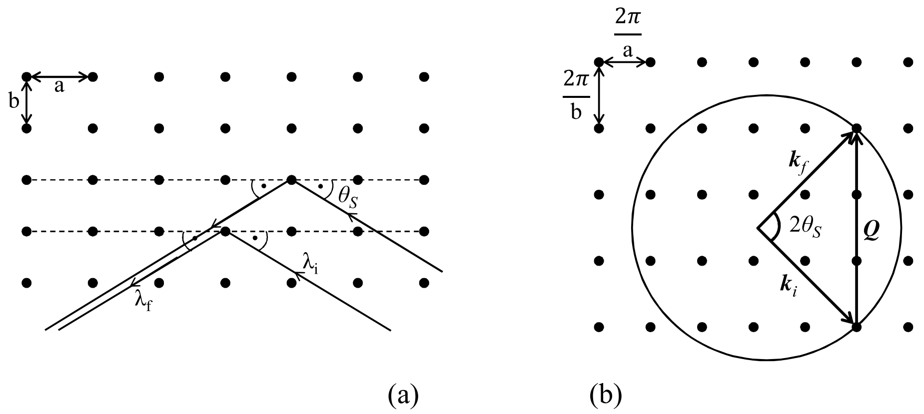

Figure 3.3: *Representation of the Bragg reflection from a single crystal lattice (a) in a real space and (b) reciprocal space.*

The dots in Figure 3.3a represent the atomic positions in real space, λ_i and λ_f are the neutron wavelengths for initial (incoming) and final (reflected) neutron beams, respectively. The dashed lines show two consecutive scattering planes in real space. In Figure 3.3b dots show the reciprocal lattice points, $\mathbf{k}_i$ and $\mathbf{k}_f$ are the initial and final wave vectors, and $\mathbf{Q}$ represents the scattering vector in the reciprocal space. The solid circle corresponds to the Ewald sphere in 2-dimensional space.

In elastic neutron scattering, $\mathbf{k}_i$ and $\mathbf{k}_f$ have to be equal, meaning there will be no energy transfer between the neutron and the sample. This condition can be formulated as

$$\mathbf{Q} = \mathbf{k}_f - \mathbf{k}_i \quad \text{with } |\mathbf{k}_f| = |\mathbf{k}_i|, \tag{3.2}$$
$$\hbar\omega = E_f - E_i = 0.$$

In case $\mathbf{G} = \mathbf{Q}$ ($\mathbf{G}$ is the lattice vector), the Laue condition is fulfilled and one observes the Bragg scattering at the particular reflection corresponding to $\mathbf{G}$. Then θ_S is the angle between $\mathbf{k}_i$ and the particular scattering plane. It holds

$$|\mathbf{Q}| = 2|\mathbf{k}_i| sin\theta_S. \tag{3.3}$$

In reciprocal space, $2\theta_S$ is the angle between the initial and the final wave vectors. It is possible to write this formula in a better known way by using the definition of the lattice vector ($|G| = 2\pi/d$) as,

$$\lambda = 2d \sin\theta_S. \tag{3.4}$$

Equation 3.4 is the well known Bragg's law with the inter-planar distance d.

In inelastic neutron scattering, it is possible to create or annihilate one or more quantum states, i.e. to create or annihilate one or multiple phonons with $\mathbf{q}$ being the propagation vector of the particular phonon with energy ω_q. In this case, momentum and energy conservation, equation 3.2 changes to the following form,

$$\begin{gathered} \mathbf{Q} = \mathbf{k}_f - \mathbf{k}_i = \mathbf{G} + \mathbf{q} \\ \hbar\omega = E_f - E_i = \hbar\omega_q. \end{gathered} \tag{3.5}$$

The fundamental theory of neutron scattering is generally discussed in the Born approximation [Bro66]. In this approximation the interaction between the sample and the neutron is replaced by a δ-function interaction. When a neutron scatters from a sample, it excites the sample from one quantum state (initial state), λ_i, to another one (final state), λ_f. For this interaction the differential cross section can be written as [SST02]:

$$\left(\frac{d^2\sigma}{d\Omega_f dE_f}\right)_{\lambda_i\to\lambda_f} = \frac{k_f}{k_i}\left(\frac{m_n}{2\pi\hbar^2}\right)^2 |\langle\mathbf{k}_f\lambda_f|V|\mathbf{k}_i\lambda_i\rangle|^2\delta(\hbar\omega + E_i - E_f) \tag{3.6}$$

where m_n is the mass of the neutron, V is the interaction operator of the neutron with the sample, and E_i and E_f are the initial and final energies, respectively. Generally in scattering experiments the differential cross section is averaged over all initial states and summed over all final states [SST02, Squ97]. After some simplifications the formula can be written in form of

$$\left(\frac{d^2\sigma}{d\Omega_f dE_f}\right)_{\lambda_i\to\lambda_f} = N\frac{k_f}{k_i}b^2 S(\mathbf{Q},\omega), \tag{3.7}$$

where

$$S(\mathbf{Q},\omega) = \frac{1}{2\pi\hbar N}\sum_{ll'}\int_{-\infty}^{\infty}\langle e^{-i\mathbf{Q}\cdot\mathbf{r}_{l'}(0)}e^{i\mathbf{Q}\cdot\mathbf{r}_l(t)}\rangle e^{-i\omega t}dt. \tag{3.8}$$

When the elastic contribution to the scattering is subtracted from the equation 3.8 the rest of the equation is related to the dissipative part of a linear response function via the fluctuation-dissipation theorem [SST02],

$$S(\mathbf{Q},\omega) = \frac{\chi''(\mathbf{Q},\omega)}{1 - e^{\frac{-\hbar\omega}{k_B T}}} \tag{3.9}$$

where $\chi''(\mathbf{Q},\omega)$ is the imaginary part of the dynamical susceptibility. Considering the creation and the destruction of one phonon in the case of neutron scattering the $\chi''(\mathbf{Q},\omega)$ has the form of

$$\chi''(\mathbf{Q},\omega) = \frac{1}{2}\frac{(2\pi)^3}{v_0}\sum_{\mathbf{G},\mathbf{q}}\delta(\mathbf{Q}-\mathbf{q}-\mathbf{G})\sum_{s}\frac{1}{\omega_{\mathbf{q}s}}|F(\mathbf{Q})|^2 \times [\delta(\omega-\omega_{\mathbf{q}s})-\delta(\omega+\omega_{\mathbf{q}s})]. \tag{3.10}$$

Here $F(\mathbf{Q})$ is the dynamical structure factor and defined by

$$F(\mathbf{Q}) = \sum_{j}\frac{\bar{b}_j}{\sqrt{m_j}}(\mathbf{Q}\cdot\xi_{js})e^{i\mathbf{Q}\cdot\mathbf{d}_j}e^{-W_j}. \tag{3.11}$$

The integrated intensity, $I(\mathbf{Q})$, of a neutron energy loss phonon measurement can be written as a function of $F(\mathbf{Q})$ as follows:

$$I(\mathbf{Q}) = A\frac{k_B T}{\hbar\omega_{\mathbf{q}s}^2}|F(\mathbf{Q})|^2. \tag{3.12}$$

This is related to the measured intensity for the phonon measurements.

One of the most important instrument used in neutron scattering is the three-axis spectrometer (TAS) which allows us to measure the scattering function $S(\mathbf{Q},\omega)$ in a wide range of the momentum ($\mathbf{Q}$) and the frequency (ω) space. Figure 3.4 shows the schematic representation of a TAS. The energies of the incoming and detected beams are selected by Bragg reflection from the monochromator and analyzer crystals, respectively.

In a regular inelastic scattering experiment a white neutron beam get first reflected from monochromator single crystal, the reflected monochromatic beam is then directed to the sample by help of neutron optics. The monochromatic neutron beam interacts with the sample and scatters in all directions. Scattered neutrons which are reaching the analyzer crystal will be reflected again to define the final energy. Those neutrons which have the desired final energy are detected by the neutron detectors. Energy and momentum transfers are defined by the rotation of these monochromator ($2\theta_M$), sample ($2\theta_S$) and analyzer ($2\theta_A$) axes.

The phonon measurements were carried out on the thermal three-axis spectrometer PUMA which is located at the Forschungs-Neutronenquelle Heinz Maier-Leibnitz (FRM II),

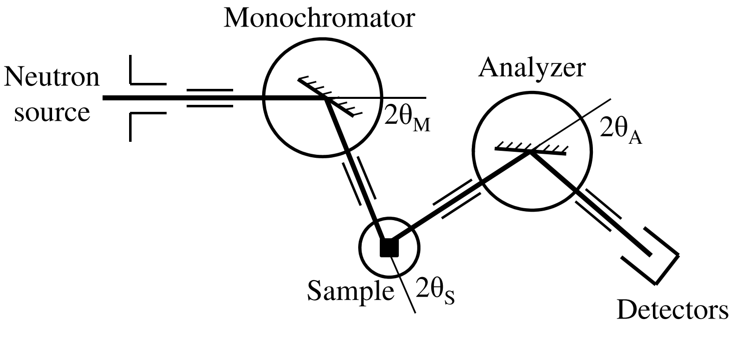

Figure 3.4: *Schematic representation of a three-axis spectrometer.* $2\theta_M$*,* $2\theta_S$ *and* $2\theta_A$ *are the scattering angles of monochromator, sample and analyzer, respectively.*

Garching. An image of the instrument is shown in Figure 3.5 where the main three axes of the instrument are visible. The huge yellow drum on the left hand side of the image is the monochromator housing which incorporates different monochromator crystals and neutron optics like neutron guides and collimators. In PUMA there are two monochromator options which are in use, PG(002) and Cu(220). For our measurements PG(002) monochromator has been mainly used due to its good resolution and high intensity at the measured energies. For high frequency transfer measurements we used the Cu(220) monochromator. The blue drum on the right hand side of the image is the analyzer drum which houses the analyzer crystals, neutron optics and detectors. As analyzer, only PG(002) has been used in our investigations. For some measurements, especially for low frequency transfer measurements, moderate collimation has been used as 40', 45', 45,' 45'. Here first number indicates the collimation between the source and the monochromator, second indicates the collimation between the monochromator and the sample, third shows the collimation between the sample and the analyzer and the last one shows the collimation between the sample and the detectors. With this setup the resolution ellipsoid is better defined in ($\mathbf{Q}$-ω)-space. In PUMA, five ^{3}He-detectors are used for neutron detection. Only one of these detectors is used for counting the neutrons because the beam is focused only on this detector. The grey-green parts in the middle of the image are the sample table (green in the bottom) and the sample environment (gray on top). For our investigations different sample environments have been used. For high temperature measurements, high temperature vacuum furnace from FRM II sample environment was available. Measurements below the room temperature have been carried out in a cryofurnace from FRM II sample environment. The room temperature measurements have been done without any sample environment.

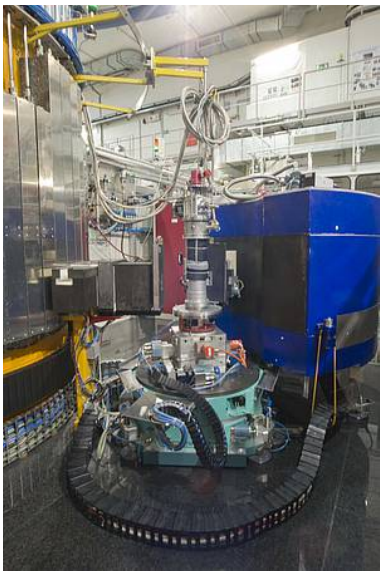

Figure 3.5: *Photo of the PUMA instrument at Forschungs-Neutronenquelle Heinz Maier-Leibnitz (FRM II). Yellow drum shows the monochromator shielding, gray cryostat shows the sample position with sample environment and blue drum shows the analyzer shielding. Taken from http://www.frm2.tum.de/de/wissenschaftliche-nutzung/spektrometrie/puma/index.html*

All inelastic measurements were mainly done in constant **q**-mode. The focus sides were used to measure the phonon dispersion for each desired **q** point. Figure 3.6 shows the difference between focus and defocus sides of a constant **q**-scan. Here, in the middle figure two different measurements have been schematically represented with corresponding intensity plots (left and right hands side figures). The ellipsoids in the middle figure show the resolution ellipsoid of the instrument different measurement points. The left hand side image represents the constant **q**-scan of a defocused measurement. The right hand side image corresponds to a focused state of a similar measurement. In the focus side the peak intensity of the inelastic signal is higher compared to the defocus side. Also the FWHM of the focus side is smaller than the defocus one. By defining the right focus side in the **q**-space, it is possible to distinguish phonons which are close to each other. In this study, focus sides were used for phonon measurements.

The phonon measurements were fitted to a damped harmonic oscillator function in a modified version of a Lorentzian function which has a form of [SST02]

$$y = y_0 + \frac{A}{2\pi\omega'}\frac{\Gamma}{(\omega \pm \omega')^2 + \Gamma^2}, \tag{3.13}$$

where y_0 is the constant background, ω is the frequency, Γ is the peak full-width half-maximum (FWHM) and

$$\omega' = \sqrt{\omega^2 - \Gamma^2}. \tag{3.14}$$

From these fits the phonon frequencies were defined from the peak maximum (ω) values

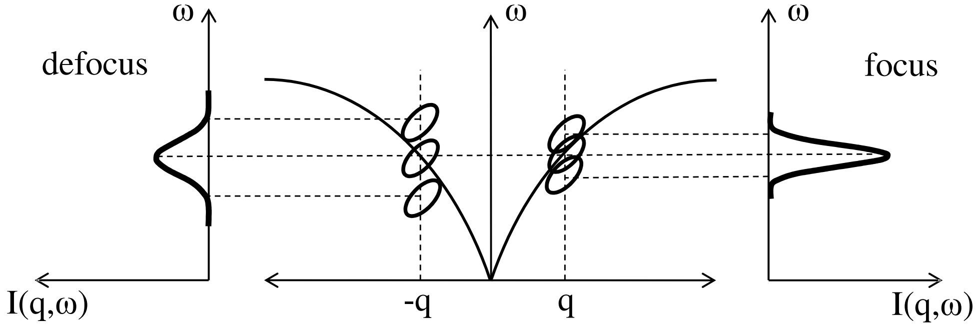

Figure 3.6: *Focus and defocus side representations of the same acoustic phonon branch. The ellipsoids represent the resolution ellipsoids of the instrument at given q and ω values.*

and the phonon life times were deduced from the widths (Γ) of these peaks. For more details and fundamentals of triple-axis scattering see [SST02].

For the determination of the crystallographic properties of the single crystal neutron diffraction experiments were carried out. Diffraction experiments were done in the REciprocal Space Investigator ($RESI$) at FRM II. Figure 3.7 shows a schematic representation of the RESI instrument. Here the white neutron beam which is coming from the source is impinging on the monochromator and the diffracted beam is directed on to the sample position with the help of neutron optics. For our investigations the incoming beam wavelength of $1\mathring{A}$ (precise value 1.03695 $\mathring{A}$) has been used. For this a Cu(422) monochromator at 90° take-off angle has been used. The sample has been mounted on an Euler cradle, interacts with the incoming beam and scatters it in all directions. The scattered beam is collected by detectors which are sitting on the Ewald sphere. In our investigations, for the detection of the scattered neutrons a MAR345 image plate detector with an FUJI BAS ND image plate has been used. This is a standard image plate with additional Gd_2O_3 as neutron converter. The Rietveld refinements of the collected data have been done by using the Jana2000 software package [PDL00].

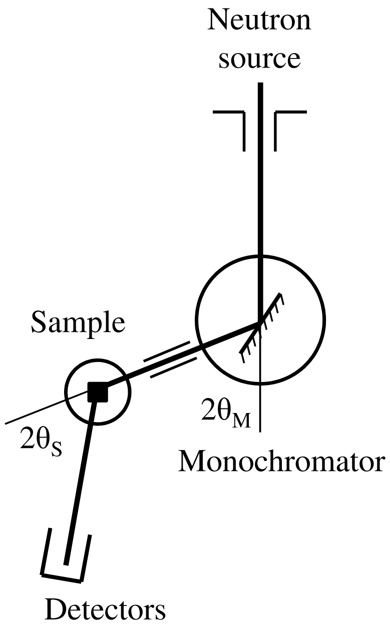

Figure 3.7: *Schematic representation of REsicprocal Space Investigator (RESI) at FRM II.* $2\theta_M$ *represents the monochromator angle which defines the energy of the monochromatic beam,* $2\theta_S$ *shows the sample angle.*

Chapter 4

Theoretical Models of the Lattice Dynamics

In general the whole phonon dispersion has to be investigated to conclude on the dynamical properties of a given material. In some cases single phonon branches can be as interesting as the whole phonon dispersion. To model and calculate the influence of the phonon dispersion to the macroscopic properties of the material (like lattice entropy, heat capacity, thermal atomic displacement, etc.) one has to model a mathematical fit to the set of measured phonons (ω_q,$\mathbf{q}$) in order to interpolate the full phonon dispersion. Most commonly the Born-von Kármán fits are used to describe a full phonon dispersion. Alternatively, the phonon dispersion can be calculated ab-initio by first-principles calculations.

In the following subchapters, the fundamental physics behind the first-principles calculations and the Born-von Kármán model will be described. For the definitions and detailed explanation of the theory of phonons it is suggested to the reader to review the books of C. Kittel [Kit86], J. A. Reissland [Rei73] and G. P. Srivastava [Sri90].

4.1 Classical Theory

In the classical approach, a phonon can be described by a fundamental two body system. The interatomic potential between two body system can be written in a Taylor series as in the following form [Kit86].

$$U = U(\mathbf{R}_0) + \left(\frac{\partial U}{\partial R}\right)_0 \cdot u + \frac{1}{2}\left(\frac{\partial^2 U}{\partial R^2}\right)_0 u^2 + \dots \tag{4.1}$$

Here $\mathbf{R}$ is the distance between the atoms and u is the displacement. $U(\mathbf{R}_0)$ is the equilibrium value and is a constant. The $\left(\frac{\partial U}{\partial R}\right)_0 \cdot u$ term creates a force and disappears in the case of equilibrium. The consideration of only the quadratic term, $\frac{1}{2}\left(\frac{\partial^2 U}{\partial R^2}\right)_0 u^2$, in equation 4.1 is known as the harmonic approximation where $\left(\frac{\partial^2 U}{\partial R^2}\right)_0$ represents an interatomic force constant [Sri90]. In the harmonic approximation, potential energy of a two body system can be written in a simple form as,

$$U_{harmonic} = \frac{1}{2}\left(\frac{\partial^2 U}{\partial R^2}\right)_0 u^2. \tag{4.2}$$

Consider a three dimensional crystal where the atomic displacement of the atom, b, in the unit cell, l, is defined as $\mathbf{u}(\mathbf{bl})$. In this case, equation 4.2 can be written as,

$$U_{harmonic} = \frac{1}{2}\sum_{\mathbf{lb},\mathbf{l'b'}}\sum_{\alpha\beta}\phi_{\alpha\beta}(\mathbf{lb};\mathbf{l'b'})\mathbf{u}_\alpha(\mathbf{lb})\mathbf{u}_\beta(\mathbf{l'b'}). \tag{4.3}$$

where $\phi_{\alpha\beta}(\mathbf{lb};\mathbf{l'b'})$ is the interatomic force constant matrix and is defined as,

$$\phi_{\alpha\beta}(\mathbf{lb};\mathbf{l'b'}) = \frac{\partial^2 U}{\partial \mathbf{u}_\alpha(\mathbf{lb})\partial \mathbf{u}_\beta(\mathbf{l'b'})}\Big|_0. \tag{4.4}$$

Here α and β correspond to different directions in the coordinate system. For example in the Cartesian coordinates, α and β may take the values of x, y or z. By generalizing the equation of motion, which is derived from Newton's second law and Hooke's law [Kit86, Sri90], one can write,

$$F_{\mathbf{lb}\alpha} = m_b\ddot{\mathbf{u}}_\alpha(\mathbf{lb}) = -\sum_{\mathbf{l'b'}\beta}\phi_{\alpha\beta}(\mathbf{lb};\mathbf{l'b'})\mathbf{u}_\beta(\mathbf{l'b'}) \tag{4.5}$$

where, m_b is the mass of the atom b.

The force constant matrix elements $\phi_{\alpha\beta}(\mathbf{lb};\mathbf{l'b'})$ have to obey some symmetry requirements [Sri90] which are lattice translation symmetry,

$$\phi_{\alpha\beta}(\mathbf{lb};\mathbf{l'b'}) = \phi_{\alpha\beta}(\mathbf{0b};(\mathbf{l'}-\mathbf{l})\mathbf{b'}) \tag{4.6}$$

and, infinitesimal translation invariance of the crystal,

$$\phi_{\alpha\beta}(\mathbf{lb};\mathbf{lb}) = -\sum_{\mathbf{l'b'}/\mathbf{lb}}\phi_{\alpha\beta}(\mathbf{lb};\mathbf{l'b'}). \tag{4.7}$$

One can try to solve the equation 4.5 with a plane wave:

$$u_\alpha(\mathbf{lb}) = \frac{1}{\sqrt{m_b}}\sum_{\mathbf{q}}U_\alpha(\mathbf{q};\mathbf{b})exp[i(\mathbf{q}\cdot\mathbf{x}(\mathbf{l})) - \omega t]. \tag{4.8}$$

By substituting equation 4.8 to equation 4.5 one can calculate,

$$\omega^2 U_\alpha(\mathbf{q};\mathbf{b}) = \sum_{\mathbf{b}'\beta} D_{\alpha\beta}(\mathbf{bb}'|\mathbf{q}) U_\beta(\mathbf{q};\mathbf{b}'). \tag{4.9}$$

Here $D_{\alpha\beta}(\mathbf{bb}'|\mathbf{q})$ is called dynamical matrix and has a structure of,

$$D_{\alpha\beta}(\mathbf{bb}'|\mathbf{q}) = \frac{1}{\sqrt{m_b m_{b'}}} \sum_{l'} \phi_{\alpha\beta}(\mathbf{0b};\mathbf{l'b'}) exp(i\mathbf{q}\cdot\mathbf{x}(\mathbf{l'})). \tag{4.10}$$

$D_{\alpha\beta}(\mathbf{bb}'|\mathbf{q})$, is also symmetric due to the symmetry of force constant matrix, $\phi_{\alpha\beta}(\mathbf{0b};\mathbf{l'b'})$. The solution of the equation 4.9 for p atoms in the unit cell will create 3p solutions with eigenvalues $\omega_s^2(\mathbf{q})$, where s = 1,2,3,..., 3p. For each eigenvalues in a given $\mathbf{q}$ an eigenvector, $\mathbf{e}_s(\mathbf{b};\mathbf{q})$, exists. By using this statement the equation 4.9 can be written in the following form,

$$\omega_s^2(\mathbf{q}) e_{s\alpha}(\mathbf{b};\mathbf{q}) = \sum_{\mathbf{b}'\beta} D_{\alpha\beta}(\mathbf{bb}'|\mathbf{q}) e_{s\beta}(\mathbf{b}';\mathbf{q}). \tag{4.11}$$

The complete solution of this problem can be searched in terms of $\omega = \omega_s(\mathbf{q})$ and $\mathbf{e} = \mathbf{e}_s(\mathbf{q})$, where s indicates polarization and acoustic and optical branches. The representation of these ω values for each phonon branch for different $\mathbf{q}$ values are called phonon spectrum. Out of the $3p$ solutions, 3 branches correspond to acoustic modes and the rest $3p - p$ branches correspond to optical modes of the system.

4.2 Quantum Theory

The classical model of the lattice vibrations is not accurate enough to describe vibrational properties of materials. To explain the vibrational properties in a better way, a more complex model is necessary, like a quantum mechanical model. In the quantum approach, the Hamiltonian of a harmonic oscillator system can be written as in the following [ML71].

$$\mathcal{H} = \sum_l \sum_b \sum_\alpha \sum_\beta \{\frac{1}{2m_b}\mathbf{p}(\mathbf{lb})^2 + \frac{1}{2}\phi_{\alpha\beta}(\mathbf{lb},\mathbf{l'b'})\mathbf{u}_\alpha(\mathbf{lb})\mathbf{u}_\beta(\mathbf{l'b'})\} \tag{4.12}$$

To change the coordinate system from particle coordinates, $\mathbf{u}(\mathbf{lb})$, to phonon coordinates, $\mathbf{U}(\mathbf{qb})$, one needs to apply Fourier transformation to the displacement with the following equations,

$$\mathbf{u}(\mathbf{lb}) = \frac{1}{\sqrt{V}} \sum_q \mathbf{U}(\mathbf{qb}) \exp[i\mathbf{qx}(\mathbf{l})] \tag{4.13}$$

$$\mathbf{U}(\mathbf{qb}) = \frac{1}{\sqrt{V}} \sum_l \mathbf{u}(\mathbf{lb}) \exp[-i\mathbf{qx}(\mathbf{l})] \tag{4.14}$$

where, V is the volume of the crystal. Similar to the displacement, the momenta of the atoms has to be transformed to the new space. To carry out this transformation one can use the following Fourier equations,

$$\mathbf{p}(\mathbf{lb}) = \frac{1}{\sqrt{V}} \sum_{q} \mathbf{P}(\mathbf{qb}) \exp[-i\mathbf{q}\mathbf{x}(\mathbf{l})] \tag{4.15}$$

$$\mathbf{P}(\mathbf{qb}) = \frac{1}{\sqrt{V}} \sum_{l} \mathbf{p}(\mathbf{lb}) \exp[i\mathbf{q}\mathbf{x}(\mathbf{l})] \tag{4.16}$$

By using these transition equations, the Hamiltonian can be rewritten in a new form,

$$\begin{aligned} \mathcal{H} = \sum_{l} \sum_{b} \sum_{q} \sum_{q'} \sum_{\alpha} \sum_{\beta} \frac{1}{V} \frac{\mathbf{P}(\mathbf{qb})\mathbf{P}(\mathbf{q'b})}{2m_b} \exp[-i(\mathbf{q}+\mathbf{q}')\mathbf{x}(\mathbf{l})] \\ + \frac{1}{2}\phi_{\alpha\beta}(\mathbf{lb}, \mathbf{l'b'})\mathbf{U}_{\alpha}(\mathbf{qb})\mathbf{U}_{\beta}(\mathbf{q'b'}) \exp[i(\mathbf{ql}+\mathbf{q'l'})]. \end{aligned} \tag{4.17}$$

Since, $\mathbf{u}(\mathbf{lb})$ and $\mathbf{p}(\mathbf{lb})$ are conjugate and provides the following case,

$$[\mathbf{u}(\mathbf{lb}), \mathbf{p}(\mathbf{lb})] = i\hbar\delta_{ll'}\delta_{bb'} \tag{4.18}$$

where, δ is the Kronecker delta function. Equation 4.18 also holds true for $\mathbf{U}(\mathbf{qb})$ and $\mathbf{P}(\mathbf{qb})$. By using the self-adjoint properties of $\mathbf{U}(\mathbf{qb})$ and $\mathbf{P}(\mathbf{qb})$, it is possible to write the Hamiltonian in a simplified form,

$$\mathcal{H} = \sum_{q} \sum_{b} \frac{1}{2m_b} \mathbf{P}(\mathbf{qb})\mathbf{P}^{\dagger}(\mathbf{qb}) + \sum_{q} \sum_{b} \sum_{b'} \sum_{\alpha} \sum_{\beta} \frac{1}{2}\phi_{\alpha\beta}(\mathbf{bb}', \mathbf{q})\mathbf{U}_{\alpha}(\mathbf{qb})\mathbf{U}^{\dagger}_{\beta}(\mathbf{qb}'). \tag{4.19}$$

Equation 4.19 gives the Hamiltonian just as a function of the momenta, $\mathbf{P}(\mathbf{qb})$, displacement, $\mathbf{U}(\mathbf{qb})$, and the harmonic force constant matrix, $\phi_{\alpha\beta}(\mathbf{bb}', \mathbf{q})$. The phonon coordinate operator, $\mathbf{U}(\mathbf{qb})$, can be driven from the Hamiltonian with the following equations,

$$i\hbar\dot{\mathbf{U}}(\mathbf{qb}) = [\mathbf{U}(\mathbf{qb}), H] = -i\hbar\frac{\mathbf{P}(\mathbf{q'b})}{m_b} \tag{4.20}$$

$$i\hbar\ddot{\mathbf{U}}(\mathbf{qb}) = [\dot{\mathbf{U}}(\mathbf{qb}), H] = \frac{1}{m_b}[\mathbf{P}(\mathbf{q'b}), H] = i\hbar\omega^2(\mathbf{q})\mathbf{U}(\mathbf{qb}) \tag{4.21}$$

which results in,

$$\ddot{\mathbf{U}}_{(\mathbf{qb})} + \omega^2(\mathbf{q})\mathbf{U}(\mathbf{qb}) = 0 \tag{4.22}$$

Equation 4.22 is the equation of motion of a harmonic oscillator with the energy eigenvalues of,

$$e(\mathbf{q}) = \hbar\omega(\mathbf{q})(n_{\mathbf{q}} + \frac{1}{2}). \tag{4.23}$$

With respect to equation 4.23, total vibrational energy of a system can be formulated as following,

$$U = \sum_{\mathbf{q}} \hbar\omega(\mathbf{q})(n_{\mathbf{q}} + \frac{1}{2}). \tag{4.24}$$

For more detailed explanation of the phonons, the phonon creation, a^+, and phonon annihilation, a^-, operators need to be taken into account in the harmonic model. Phonon creation operator can be defined as,

$$a^+|n\rangle = \sqrt{n+1}|n+1\rangle. \tag{4.25}$$

Equation 4.25 shows that, when the phonon creation operator is applied to a harmonic oscillator with n quantum numbers, it increases the number of phonon by one. Similar to these, phonon annihilation operator can be defined as following,

$$a^-|n\rangle = \sqrt{n}|n-1\rangle. \tag{4.26}$$

When these operators are embedded in the Hamiltonian, it forms a harmonic oscillator cluster Hamiltonian with the form of,

$$\mathcal{H} = \sum_{\mathbf{q}} \hbar\omega(\mathbf{q})(a^+_{\mathbf{q}} a^-_{\mathbf{q}} + \frac{1}{2}). \tag{4.27}$$

When the effect of both creation and annihilation operators is taken into consideration,

$$a^+a^-|n\rangle = a^+\sqrt{n}|n-1\rangle = n|n\rangle \tag{4.28}$$

$|n\rangle$ becomes an eigenstate, which corresponds to the eigenvalue n of the a^+a^- operator. By combining the equations 4.27 and 4.28 it is possible to obtain the total energy of the system - equation 4.24. By using this fundamental quantum mechanics it is possible to calculate the phonon dispersion.

4.3 Born-von Kármán Model

The first-principles calculations consume too much calculation time and the temperature can not be directly taken into account in the models. Thus it is necessary to resort to fitting model which can describe the phonon dispersion in an efficient way. In the Born-von Kármán model the crystal potential energy can be written in the following form.

$$U = \sum_i \sum_j \sum_\alpha \sum_\beta \phi_{\alpha\beta}(i,j) u_\alpha(i) u_\beta(j). \tag{4.29}$$

Here $\phi_{\alpha\beta}(i,j)$ is the force constant between atom i and j. By using the inter-atomic distances and the force constants in between the atom pairs, one can model the measured phonon dispersions with Born-von Kármán model. In principle, the Born-Oppenheimer approximation allows to express the dynamical matrix of any system by using force constants [SP06]. In theory, this model can be only used for short range interactions in lattices of high symmetry. To describe the an-harmonic interaction in the phonon dispersion (like soft phonon modes) the number of parameters can be increased. Fits with large number of parameters give better mathematical fit to the phonon dispersion but this does not always mean that all of fit parameters have a physical meaning. In the Born-von Kármán model, the interaction between two neighboring atoms can be defined by one transversal (f_T) and one longitudinal (f_L) force constants. From these defined force constants it is possible to derivate the energy of the system with the above mentioned equation.

In this work, the GENAX software [Rei10] has been used to apply the Born-von Kármán model to the phonon dispersions. With this software it is possible to fit the phonon dispersion by using different number of interactions and calculate inelastic structure factors additional to the macroscopic thermal properties. For each Born-von Kármán fit the inelastic structure factors of high symmetry directions were compared with the experimental intensities. The vibrational density of states have been calculated within the harmonic approximation by the GENAX software and thermal properties have been calculated from these density of states.

4.3.1 Phonon Related Calculations: Debye and Einstein Models

Let us consider N^3 atoms in a three dimensional cube with side length of L. There is only one $\mathbf{q}$ allowed in the reciprocal volume of $(2\pi/L)^3$. There are $D(\mathbf{q}) = (L/2\pi)^3$ values of $\mathbf{q}$ allowed in a unit volume of the $\mathbf{q}$-space for each phonon polarization. From this definition, the number of states of frequency, $g(\omega)$, between a defined frequency region can be formulated as [Kit66],

$$g(\omega)d\omega = \int d^3q D(\mathbf{q}) = \left(\frac{L}{2\pi}\right)^3 \int d^3q, \tag{4.30}$$

where, the integral is extended in the $\mathbf{q}$-space for the frequencies between ω and $\omega + d\omega$. Let dS_ω define the element of area on the surface of $\mathbf{q}$-space with a constant frequency ω. The element of volume between the surfaces of ω and $\omega + d\omega$ can be written as a volume of a cylinder,

$$d\omega = d\mathbf{q} \cdot \nabla_{\mathbf{q}}\omega \tag{4.31}$$

where, $d\mathbf{q}$ corresponds to the height of the cylinder. From this definition the density of the states can be written in the following form,

$$g(\omega)d\omega = \left(\frac{L}{2\pi}\right)^3 \int \frac{dS_\omega}{\nabla_{\mathbf{q}}\omega} d\omega. \tag{4.32}$$

Here, $\nabla_{\mathbf{q}}\omega$ is called as group velocity, v_g [Kit66]. Points where the group velocity is zero, have a special importance and these points in the density of states are known as Van Hove singularities. For the Debye model, the spectrum of the density of states is fulfilling the following condition.

$$\left.\begin{array}{rl} \frac{3}{\omega_D}\omega^2, & \omega \leq \omega_D \\ 0, & \omega > \omega_D \end{array}\right\} \quad = g(\omega) \tag{4.33}$$

Here, $\frac{3}{\omega_D}$ is a constant, ω_D is the Debye frequency which defines the highest possible vibration frequency for the Debye model [SP06]. The integral of the vibrational density of the states in the whole frequency region has to fulfill the following condition.

$$\int_0^\infty g(\omega)d\omega = 1 \tag{4.34}$$

It is possible to calculate lattice vibration related properties like vibrational entropy, lattice specific heat and atomic displacements of a material directly from the vibrational density of the states.

Vibrational entropy, $S_{vib}(T)$, can be calculated from the vibrational density of states with the following equation [SP06, Ful10]:

$$S_{vib}(T) = -3k_B \int_0^\infty g(\omega)\{n(\omega)ln[n(\omega)] - [1 + n(\omega)]ln[1 + n(\omega)]\}d\omega \tag{4.35}$$

where, $n(\omega)$ is the Bose-Einstein distribution function and defined as;

$$n(\omega) = \frac{1}{\exp(\frac{\hbar\omega}{k_B T} - 1)} \tag{4.36}$$

here $\hbar$ and k_B, are the Planck's and Boltzmann constants, respectively.

From the density of states, it is also possible to calculate the mean atomic displacements of the atoms. The average of mean square displacement in the unit cell, $\langle (u_x)^2 \rangle$, is defined as,

$$\langle u_x^2 \rangle = \frac{3\hbar}{4\pi M_x} \int \frac{g_x(\omega)}{\omega} \coth(\frac{\hbar\omega}{2k_B T}) d\omega \tag{4.37}$$

where, M_x is the mass of the atom x and $g_x(\omega)$ is the partial density of states of atom x. From the high temperature approximation, the Debye temperatures and the Debye frequencies can be calculated from the mean square displacement with following relations, respectively:

$$\Theta_D^2 = \frac{3 \cdot \hbar^2 \cdot T}{k_B \cdot M \cdot \langle (u_x)^2 \rangle} \tag{4.38}$$

and

$$\nu_D = \frac{k_B \cdot \Theta_D}{h}. \tag{4.39}$$

The constant volume heat capacity of a system, $C_v(T)$, can be described as a function of the Debye temperature as formulated below [Kit86, DTLP03]:

$$C_v(T) = 9Nk_B \left(\frac{T}{\Theta_D(T)} \right)^3 \int_0^{\frac{\Theta_D(T)}{T}} \frac{x^4 e^x}{(e^x - 1)^2} dx. \tag{4.40}$$

Here, $x = \hbar\omega / k_B T$. For the high temperatures, $x \ll 1$, heat capacity reaches to the limit value of $3Nk_B$, which agrees with Dulong-Petit law. In the low temperatures, $x \gg 1$,

$$\int_0^{\frac{\Theta_D(T)}{T} \approx \infty} \frac{x^4 e^x}{(e^x - 1)^2} dx \approx \frac{4\pi^4}{15} \tag{4.41}$$

and equation 4.40 can be re-written in the following form,

$$C_v(T) = \frac{12\pi^4}{5} Nk_B \left(\frac{T}{\Theta_D(T)} \right)^3. \tag{4.42}$$

Equation 4.42 is known as Debye T^3 law. For the very low temperature region, where only long wavelength acoustic modes are thermally excited, the T^3 approach works perfectly. In this low temperature region, only modes which fulfill the condition of $\hbar\omega < k_B T$, can be excited.

According to the Einstein model, the vibrational density of the states is defined as a delta function centered on a defined frequency, ω_0 - $D(\omega) = N(\omega - \omega_0)$. The heat capacity of this model can be calculated directly from the temperature derivation of the thermal energy of the system.

$$C_v(T) = \left(\frac{\partial U}{\partial T} \right)_V = 3Nk_B \left(\frac{\hbar\omega}{k_B T} \right) \frac{e^{\frac{\hbar\omega}{k_b T}}}{(e^{\frac{\hbar\omega}{k_B T}} - 1)^2} \tag{4.43}$$

In the high temperature region the constant volume heat capacity (eq. 4.43) approaches to the Dulong-Petit limit of $3Nk_B$. In the low temperature region equation 4.43 decreases with $exp(\frac{-\hbar\omega}{k_B T})$ which does not fit perfectly to the experimental phonon contributions. Due to this property Einstein model can only be used to explain high temperature heat capacities.

Chapter 5

Sample Properties and Phase Diagrams

5.1 Chemical and Physical Characterization of Ni-Mn-Ga Alloys

Single- and poly-crystals which are used in this work were investigated for chemical and physical properties. The chemical composition analysis of these crystals have been done precisely before doing any other measurement. After the determination of the composition, the physical properties like structural transition and magnetic transition properties were investigated by means of calorimetric and magnetic measurements. Additionally, detailed structural investigation of offstoichiometric Ni-Mn-Ga single crystal were carried out in both high temperature (austenite) and low temperature (martensite) phases. The results of these above mentioned measurements are shown in the following subchapters. Table 5.1 shows an abstract of the measured single crystals with corresponding phases and temperatures.

Table 5.1: Observed phases in the investigated Ni-Mn-Ga single crystals.

Sample	Austenite	Premartensite	Martensite
Ni_2MnGa	$L2_1$ (T > 280 K)	3M (220 K < T < 280 K)	NM (T < 220 K)
$Ni_{49}Mn_{32}Ga_{19}$	$L2_1$ (T > 360 K)	–	–
$Ni_{50}Mn_{29}Ga_{21}$	–	–	5M (at 300 K)
$Ni_{50}Mn_{30}Ga_{20}$	–	–	NM (at 300 K)

5.1.1 Chemical Compositional Analysis Results

The energy dispersive x-ray analysis (EDX) measurement results of $Ni_{2+x}Mn_{1-x}Ga$ polycrystalline samples are shown in Table 5.2 with corresponding standart error calculations. The shown atomic percentages are the mean values of 5 different measurements from different spots on each sample. The valance electron per atom (e/a) values were calculated by using these mean concentration values. For the valance electron concentration calculations, for Ni and Mn 3d and 4s electrons and for Ga 4s and 4p electrons were used (Ni:[Ar] $4s^2$ $3d^8$; Mn:[Ar] $2s^2$ $3d^5$; Ga:[Ar] $4s^2$ $3d^{10}$ $4p^1$).

Table 5.2: The EDX measurement results of $Ni_{2+x}Mn_{1-x}Ga$ polycrystals with standart errors.

Sample	at.% Ni	at.% Mn	at.% Ga	e/a
$Ni_{50}Mn_{25}Ga_{25}$	50.20 ± 0.13	24.15 ± 0.31	25.65 ± 0.34	7.48
$Ni_{52.5}Mn_{22.5}Ga_{25}$	52.61 ± 0.33	21.41 ± 0.40	25.94 ± 0.21	7.54
$Ni_{55}Mn_{20}Ga_{25}$	55.33 ± 0.40	19.62 ± 0.26	25.04 ± 0.32	7.66
$Ni_{57.5}Mn_{17.5}Ga_{25}$	57.38 ± 0.07	17.17 ± 0.22	25.44 ± 0.28	7.71
$Ni_{60}Mn_{15}Ga_{25}$	59.89 ± 0.45	14.85 ± 0.19	25.16 ± 0.30	7.79
$Ni_{62.5}Mn_{12.5}Ga_{25}$	61.45 ± 0.21	12.03 ± 0.25	26.53 ± 0.27	7.79
$Ni_{65}Mn_{10}Ga_{25}$	64.68 ± 0.31	9.68 ± 0.21	25.64 ± 0.20	7.92

The EDX analysis results of the single crystals are shown in Table 5.3 and Table 5.4 . The offstoichiometric measurements, shown in Table 5.3 have been carried out by Mehaddene *et al.* [TJ06]. One side of the single crystal has been cut, polished and the measurements have been done along this surface. The measurement positions have been selected along the crystal to see the compositional deviation along the sample. The results show that there is no monotonous change in the chemical composition along the offstoichiometric single crystal.

Chemical composition analysis of the stoichiometric Ni_2MnGa has been done in detail and is shown in Table 5.4. The EDX analysis were done in two opposing faces of the stoichiometric single crystal. Both faces were polished before the EDX measurement. Positions from 1 to 10 corresponds to one side of the single crystal from top to bottom and 11 to 20 corresponds to the opposite site from bottom to top - see Figure 5.1. The results show no significant difference in chemical composition along the stoichiometric single crystal.

Table 5.3: The EDX measurement results of offstoichiometric Ni-Mn-Ga ($Ni_{49}Mn_{32}Ga_{19}$) single crystal with standard error calculations [TJ06].

Position	at.% Ni	at.% Mn	at.% Ga
1	48.73	32.74	18.53
2	49.46	32.41	18.13
3	48.40	33.32	18.74
4	48.89	32.93	18.18
5	49.14	32.42	18.44
6	49.08	32.54	18.38
7	48.52	32.70	18.78
8	48.16	33.20	18.68
9	48.54	32.56	18.89
10	49.02	32.71	18.27
11	49.17	32.27	18.55
average	48.83 ± 0.12	32.71 ± 0.10	18.51 ± 0.08

Table 5.4: The EDX measurement results of stoichiometric Ni-Mn-Ga (Ni_2MnGa) single crystal with standard error calculations.

Position	at.% Ni	at.% Mn	at.% Ga	Position	at.% Ni	at.% Mn	at.% Ga
1	51.05	25.93	23.03	11	50.98	25.41	23.61
2	52.39	24.09	23.52	12	51.55	26.34	22.12
3	51.26	25.38	23.36	13	50.70	26.12	23.18
4	52.10	25.28	22.62	14	50.96	26.93	22.11
5	50.46	25.56	23.98	15	50.98	26.00	23.02
6	51.72	25.39	22.90	16	51.29	27.04	21.66
7	50.68	26.13	23.19	17	50.15	27.63	22.21
8	50.86	26.75	22.39	18	49.21	27.11	23.68
9	50.91	27.02	22.07	19	49.88	26.89	23.22
10	50.37	27.29	22.34	20	50.79	27.94	21.27
				average	50.91 ± 0.17	26.31 ± 0.22	22.78 ± 0.17

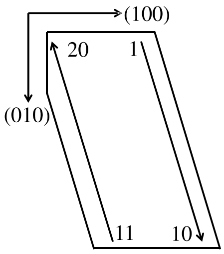

Figure 5.1: Sketch of the EDX measurement points on the stoichiometric Ni_2MnGa single crystal.

5.1.2 Calorimetric Analysis Results

Transition temperatures obtained from the differential scanning calorimetry (DSC) measurements for the $Ni_{2+x}Mn_{1-x}Ga$ polycrystals are shown in Figure 5.2. The measurement results of $Ni_{60}Mn_{15}Ga_{25}$, $Ni_{62.5}Mn_{12.5}Ga_{25}$ and $Ni_{65}Mn_{10}Ga_{25}$ could not be shown in the figure, due to the high transition temperatures of these compositions. Above mentioned compositions have higher structural transition temperatures than the measurement limit of the setup. For the DSC measurements aluminum sample cans have been used and these cans limit the highest point of the measurement temperature to 873 K. The transition temperature of $Ni_{75}Ga_{25}$ has been taken from [YQIE04] and a linear fit was applied to the present data. Fitting results show similar behavior as Mn rich compositions [PMA09]. Present work shows that 1% nickel excess increases structural transition temperature of the alloy by around 50 K. The study of Planes *et al.* [PMA09] gives 33 K temperature change for 1% of excess manganese. It was shown be by Entel *et al.* that the substitution of Ga by Ni increases the structural transition temperature of the Ni-Mn-Ga alloys [EBK$^+$06]. Here, we proved that the substitution of Mn with Ni increases the martensite transition temperature even more.

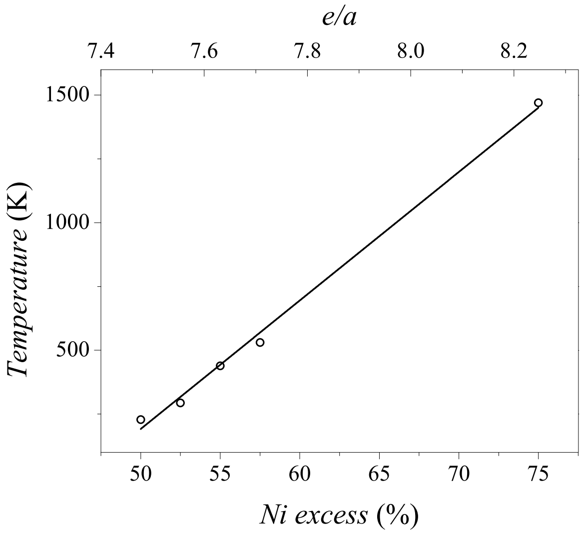

Figure 5.2: *Structural transition temperatures of $Ni_{2+x}Mn_{1-x}Ga$ polycrystals for different Ni concentrations. Symbols correspond to measured martensite transition temperature, solid line is a linear fit to data. Transition temperature of Ni_3Ga is taken from literature [YQIE04].*

5.1.3 Magnetic and Magnetocaloric Properties

The magnetic transition temperatures of stoichiometric and offstoichiometric single crystals were investigated as a function of temperature. Figure 5.3 shows temperature dependent magnetization measurements of Ni_2MnGa alloy. Different symbols correspond to different measurement sequences. Full circles correspond to ZFC measurements, dotted triangles correspond to FC and open squares correspond FH measurements, respectively. Definitions of measurements were given in Chapter 3.2.1. Structural transition temperatures were defined by using the FC and FH measurements. The Curie temperature, T_C, is defined from the FC measurement. Defined critical temperatures are given inside the Figure 5.3. For the stoichiometric sample the structural transition sequence is observed as;

$$L2_1 \xrightarrow{280\ K} 3M \xrightarrow{220\ K} NM$$

where $L2_1$, $3M$ and NM correspond to austenite, pre-martensite and non-modulated martensite, respectively. These transformation temperatures are obtained from the derivative of the FC measurements. For the transition temperature determination peak minimum temperatures of the derivatives have been used. Curie temperature of the stoichiometric sample is found as 383 K, from the DSC measurement. T_C of Ni_2MnGa is out of the upper temperature limit of the magnetometer, therefore it could not be observed in the MT measurements.

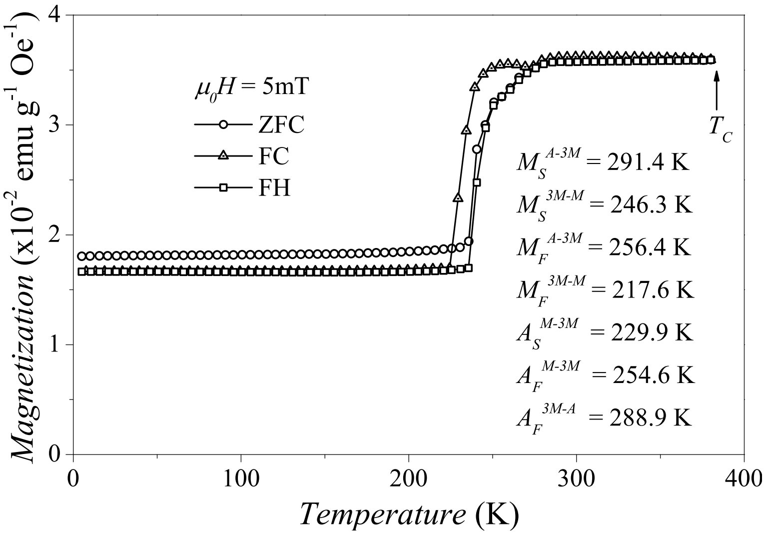

Figure 5.3: *Temperature dependent magnetization measurements of stoichiometric Ni_2MnGa under 5mT external magnetic field. The solid circles indicate the ZFC measurements, up triangles and square indicate the FC and FH measurements, respectively. The observed critical temperatures are shown in the figure.*

Thermal hysteresis between the FC and FH measurements provides information about the structural transition due to the hysteresis nature of the martensitic transition - see Chapter 2.2. The structural transition temperatures were defined from the onset values of the derivatives of magnetization measurements. M_X^{Y-Z} represents the martensite transition temperatures, where X shows the start (S) or finish (F) temperatures, Y and Z shows the initial and product phases of the transition, respectively ($A=$ austenite, $3M=$ pre-martensite and $M=$ martensite phases). A_X^{Y-Z} represents the austenite transition temperatures similar to martensite transition temperatures as explained above.

The magnetization difference between ZFC and FC measurements gives information about the anti-ferromagnetic interactions in the material. The small difference which is observed in Figure 5.3 is based on the anti-ferromagnetic interaction in the material due to the small offstoichiometry which is observed in the stoichiometric single crystal - see Table 5.4. Small decrease in the FC measurement around 270 K corresponds to the pre-martensite feature of the stoichiometric composition. This pre-martensitic transformation shows its existence in FC and FH measurement as a slope change around 270 K.

Figure 5.4 shows the temperature dependent magnetization of Ni_2MnGa under strong external magnetic field of 5 Tesla. The structural transition temperatures could not be determined due to the noisy derivation of the FC and FH measurements. Despite the noisy derivation of the measurements, the structural transition keeps its existence in the measurements as a step like behavior around 240K. It is observed that, under 5 Tesla magnetic field, the structural transition temperature was shifted a little bit to a lower value. Additionally, the anti-ferromagnetic behavior which was observed in the low field measurements was disappeared due to the high external magnetic field.

External magnetic field dependent magnetization measurements of the stoichiometric sample is shown in Figure 5.5. Here, each color represents different isothermal measurement. For each temperature, the magnetic field was applied up to 5 Tesla and during the application of the field, magnetization of the sample was measured. In the temperature interval of $200 \text{ K} \leq \text{T} \leq 300 \text{ K}$ ferromagnetic behavior has been observed.

From the field dependent magnetization measurements, entropy changes, ΔS_{MT}, have been calculated by using the well known Maxwell equation [PGPT01];

$$\Delta S_{MT}(H,T) = S(H_1,T) - S(H_2,T) = \mu_0 \int_{H_1}^{H_2} \left(\frac{\delta M(H,T)}{\delta T} \right)_H dH \tag{5.1}$$

where, $S(H_1,T)$ and $S(H_2,T)$ are entropies at constant temperatures under different mag-

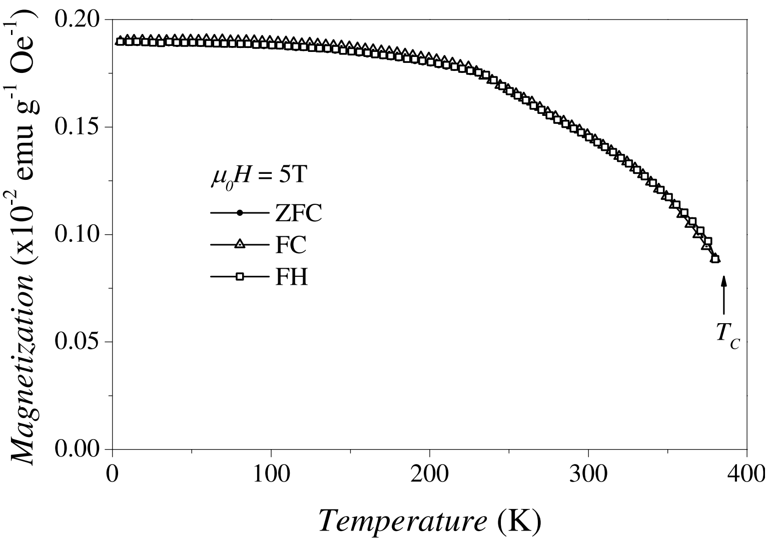

Figure 5.4: *Temperature dependent magnetization measurements of stoichiometric* Ni_2MnGa *under 5T external magnetic field. The solid circles indicate the ZFC measurements, up triangles and square indicate the FC and FH measurements, respectively.*

netic fields. For the calculations of the entropy changes equation 5.1 has been converted to a numerical form as in the following,

$$\Delta S(H, M) = \frac{\Delta H}{2\Delta T}\left(\Delta M_1 + 2\sum_{i=2}^{n-1}\Delta M_i + \Delta M_n\right). \tag{5.2}$$

Here, ΔM_x stands for the magnetization difference in between two consecutive temperatures. ΔT and ΔH correspond to the step sizes of temperature and magnetic field changes.

Calculated entropy changes are shown in Figure 5.5 as an inset. Here, different colors represent different magnetic field changes. As seen from the calculations highest entropy change was observed for 5 Tesla magnetic field change as expected. When an external magnetic field is applied to a ferromagnetic material, a decrease in magnetic entropy is expected. This holds true for Ni_2MnGa, only for the magnetic field changes higher than 2 Tesla. In general, it is claimed that, the entropy changes which are calculated directly from the magnetization measurements are named as magnetic entropy changes, ΔS_M. But this definition is only true if the entropy calculations are done around the second order transition like Curie temperature. In the case of Ni_2MnGa, around 270 K, a structural transition occurs and due to this structural transition, magnetization of the sample changes. Related to this change, at low magnetic fields, a positive entropy change has been observed - see inset of Figure 5.5. It is not possible to observe an increase in the magnetic entropy change of a ferromagnet with the application of external magnetic field. This anomalous behavior in the entropy changes are strongly related with the coupling of the vibrational entropy with the electronic and/or magnetic entropies.

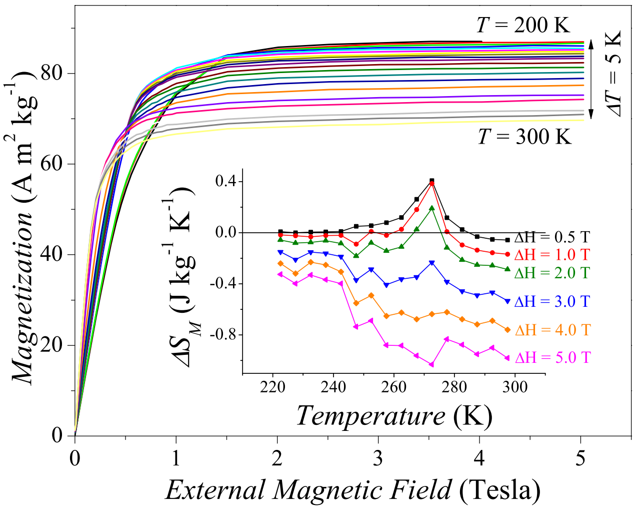

Figure 5.5: *Magnetic field dependence of stoichiometric Ni_2MnGa around the structural transition temperature. Different colors correspond to different isothermal measurement. Inset figure shows the entropy change calculated from the field dependent magnetization.*

The temperature dependent magnetization measurements of $Ni_{49}Mn_{32}Ga_{19}$ under 5mT magnetic field is shown in Figure 5.6. For the offstoichiometric composition, the observed structural transition has a sequence of;

$$L2_1 \xrightarrow{360\ K} 5M \tag{5.3}$$

where the $L2_1$ corresponds to the high temperature austenite phase, $5M$ correspond to low temperature martensite phases of five-layer modulated martensite. The transition temperature has been obtained from the derivative of FC measurement. All of the obtained critical temperatures are indicated by arrows in the Figure 5.6. The obtained structural transition temperatures are M_S= 361.1 K, M_F= 351.2 K, A_S=357.5 K and A_F= 362.5 K. A_F temperature could not be observed due to the overlapping of A_F and the Curie temperature. The $Ni_{49}Mn_{32}Ga_{19}$ shows paramagnetic ordering for the temperatures above T_C= 371.2 K.

Figure 5.6 shows a difference in between the ZFC and FC measurements at low temperatures which is due to the antiferromagnetic relations. The nature of this splitting has been investigated by Aksoy *et al.* by the means of neutron polarization analysis on Ni-Mn-based Heusler alloys [AAD⁺09]. It has been shown in [AAD⁺09] that in the Ni-Mn-based Heusler alloys the excess manganese creates antiferromagnetic interaction in the martensite phase which reveals itself as a splitting of ZFC and FC. Additionally, studies of Khan *et al.* [KDSA07] and Li *et al.* [LJC⁺07] confirm the presence of antiferromagnetic interactions in the martensite phases of Ni-Mn-based Heusler alloys.

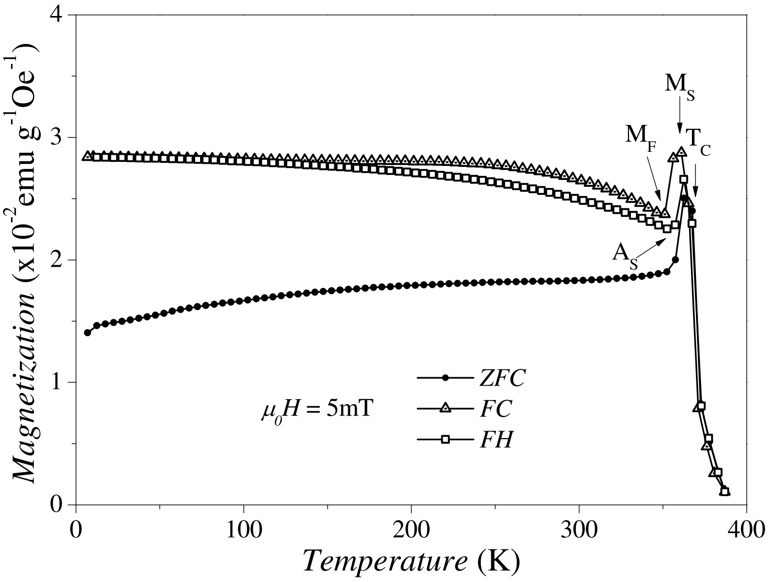

Figure 5.6: *Temperature dependent magnetization measurements of offstoichiometric* $Ni_{49}Mn_{32}Ga_{19}$ *under 5mT external magnetic field. The solid circles indicate the ZFC measurements, up triangles and square indicate the FC and FH measurements, respectively. Critical temperatures are indicated by arrows in the figure.*

5.1.4 Elastic Measurements of Ni-Mn-Ga Alloys

Crystallographic and compositional investigations of the offstoichiometric single crystals have been carried out by using the elastic neutron scattering technique. Rietveld refinement of high temperature austenite phase has been carried out for the elastic measurements at 600 K to hinder the magnetic scattering of the ferromagnetic ordering in the austenite phase. For the refinement, face centered cubic structure with the space group of $Fm\bar{3}m$ has been used. The obtained lattice parameter of the austenite phase at 600 K was 5.8548 $\mathring{A}$. Table 5.5 shows the refined atomic coordinates of the austenite phase with the occupancy factors. The chemical composition of $Ni_2Mn_{1.21}Ga_{0.79}$ ($Ni_{50}Mn_{30.25}Ga_{19.75}$) has been calculated from the intensities of Bragg reflections. The neutron coherent scattering lengths of 10.3, -3.730 and 7.388 fm have been used for Ni, Mn and Ga, respectively.

Similar to the austenite phase, five-layered modulated martensite structure has been investigated by elastic neutron scattering. The elastic measurements of the martensite phase have been carried out at room temperature where the offstoichiometric composition is in a fully ferromagnetic martensite phase. The Rietveld refinement of the five layered martensite phase has been carried out without taking the magnetic contribution into account. The refinement results of the room temperature measurement of martensite $Ni_{50}Mn_{29}Ga_{21}$ are shown in Table 5.6. In the martensite phase, as expected, five layered modulations have been observed in the surface normal to the [001] direction. Figure 5.7a shows the reconstructed surface, normal to the [001] direction for the five layered martensite of $Ni_{50}Mn_{29}Ga_{21}$ in a comparison with a corresponding transversal elastic measurement of

Table 5.5: Rietveld refinement results of the $L2_1$ ($Fm\bar{3}m$) phase of $Ni_{49}Mn_{32}Ga_{19}$ at 600 K. The unit cell parameters of the austenite phase are a=b=c= 5.8548∓0.0020 $\AA$ and $\alpha=\beta=\gamma=90°$. Columns represent the atomic positions and occupancies of the corresponding atoms.

Atom Label	a/x	b/y	c/z	Occupancy
Ga	0	0	0	0.793(13)
Mn	0.5	0.5	0.5	1
Ni	0.25	0.25	0.25	1
Mn	0	0	0	0.207(13)

PUMA around 220 Bragg peak - Figure 5.7b.

For the Rietveld refinements, commensurate modulation vector **q**= 0.4 r.l.u. have been used in the modulation direction of c^*. The elastic neutron scattering measurements show that the modulation of the martensite is not only in one direction but in two different directions which are perpendicular to each other. Figure 5.7a shows these two different modulations in the martensite phase along [110] and [$1\bar{1}0$] directions. Before each elastic and inelastic measurement the five-layered martensite samples have been mechanically trained to create a single variant state but elastic measurement results show that it is not possible to select one of the variants just by applying the uniaxial pressure to the sample. Two observed shuffling kinds, (110)[$1\bar{1}0$] and ($1\bar{1}0$)[110], create two different kind of domains with a domain boundary. These kind of domain structures are observed in different offstoichiometric compositions of the marteniste Ni-Mn-Ga alloys [GSL+03, RCW+10, CGH+11].

Table 5.6: Atomic positions and occupancy factors of the monoclinic martensite phase of $Ni_{50}Mn_{29}Ga_{21}$ with the space group of $I2/m(\alpha 0 \gamma)00$. The unit cell parameters are a= 4.1933∓0.0018 $\AA$, b= 4.2013∓0.0029 $\AA$, c=5.5543∓0.0020 $\AA$ and $\alpha=\gamma=90°$, $\beta=90.273$ ∓0.052°.

Atom Label	a/x	b/y	c/z	Occupancy
Mn	0	0	0	0.5
Ga	0	0	0.5	0.422(10)
Mn	0	0	0.5	0.078(10)
Ni	0	-0.5	0.2519(5)	0.5

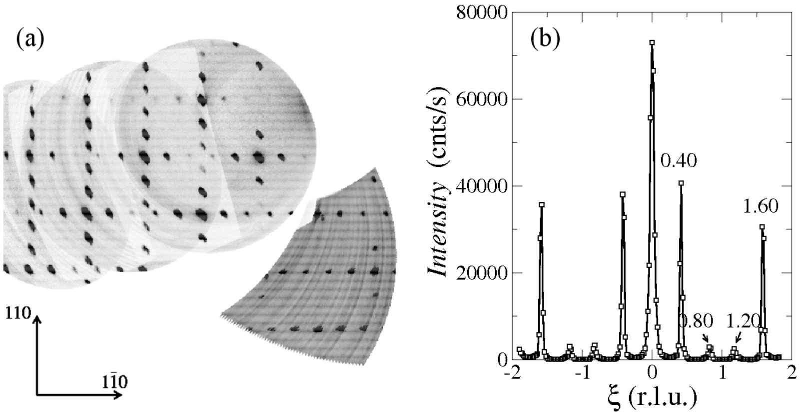

Figure 5.7: *(a) depicts the reconstructed hk0-plane of the five-layered modulated martensite phase. Black points are the Bragg intensities of different scattering planes measured at the single crystal diffractometer RESI. (b) shows elastic measurements of [2+ξ 2-ξ 0]. Superstructure Bragg peaks of the modulated martensite phase are observed at the commensurate positions of ξ = 0.4, 0.8, 1.2, and 1.6 r.l.u. For reason of comparison the r.l.u are expressed in terms of the cubic $L2_1$ austenite representation.*

5.1.4.1 Mosaic Spread of Ni-Mn-Ga Single Crystals

The qualities of the single crystals which have been used in the inelastic neutron scattering measurements were defined by the rocking curve measurements. Selected rocking curve measurements of $Ni_{49}Mn_{32}Ga_{19}$ are shown in Figure 5.8 for 200 and 220 Bragg reflections of cubic $L2_1$ phase. Here the symbols are experimental results and the red curves are Gaussian fits to the measurements. Full width half maximums, $FWHM$, of the measurements are calculated from the width of these Gaussian fits. The mosaic spreads of 1.40° and 1.29° are obtained from the $FWHM$ of $Ni_{49}Mn_{32}Ga_{19}$, respectively for 200 and 220 Bragg peaks.

Figure 5.9 shows selected rocking curve measurements of the stoichiometric Ni_2MnGa in the high temperature cubic ($L2_1$) phase. Black symbols correspond to the measurement results and solid red curves are Gaussian fits to the experimental results. At room temperature, mosaic spread of Ni_2MnGa for 200 and 220 peaks are calculated as 1.36° and 1.40°, respectively. Mosaic spreads of Ni_2MnGa and $Ni_{49}Mn_{32}Ga_{19}$ are similar to each other which creates similar resolution limits for the samples.

Mosaic spreads around the 200 Bragg peak of modulated martensites are shown in Figure 5.10. Both measurements were carried out at room temperature. The mosaic spread of the 5M martensite phase has been achieved after proper mechanical training of the single

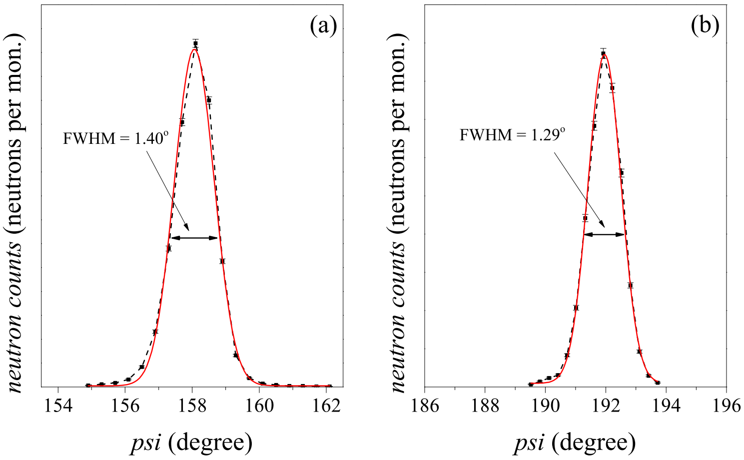

Figure 5.8: *Rocking curve measurements of $Ni_{49}Mn_{32}Ga_{19}$ alloy at fundamental reflections of the cubic $L2_1$ phase (a) 200 and (b) 220. The measurements were done at 373 K with k_f = 2.662 Å. The mosaic spread of the crystal for 200 and 220 reflections are observed as 1.40° and 1.29°, respectively.*

crystal. In the case of 7M martensite no mechanical training has been applied to the sample and due to this reason secondary variant is visible in the rocking curve measurement. The mechanical training is not suitable for the 7M single crystal due to its high fragility. All of the 7M martensite measurements have been carried out on this crystal by T.Mehaddene.

Figure 5.11 shows the rocking curve measurements of non-modulated $Ni_{50}Mn_{30}Ga_{20}$ alloy in the marteniste phase at room temperature. In Figure 5.11a multiple peaks are observed due to the multi variant structure of the non-modulated phase. From this measurement, the mosaic spread of the sample is defined around 10°. In this multi variant state it is not possible to make any phonon measurements. To overcome this problem, the single crystal is mechanically trained by applying uni-axial pressure perpendicular to the unit cell surfaces. Figure 5.11b depicts the same measurement after mechanical training process. In the non-modulated martensite phase after a proper mechanical training the multi variant structure changes to perfect single variant phase.

Rocking curve measurements show the qualities of the investigated single crystals. It has been shown that for the austenite samples mosaic spreads lower than 1.4° have been observed which makes these samples suitable for phonon measurements. In the case of 5M martensite, a mosaic spread around 1.15° has been achived after mechanical training.

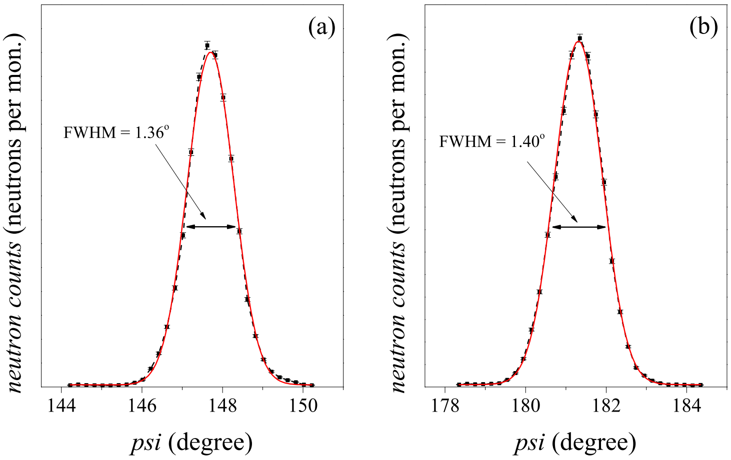

Figure 5.9: *Rocking curve measurements of Ni_2MnGa alloy at fundamental reflections of the cubic $L2_1$ phase (a) 200 and (b) 220. The measurements were done at 300 K with k_f = 2.662 Å. The mosaic spread of the crystal for 200 and 220 reflections are observed as 1.36° and 1.40°, respectively.*

The same holds true for the NM martensite sample. After mechanical training a single variant state with mosaic spreat smaller than 1.5° has been achieved. The measurement of T.Mehaddene show that, in the 7M martensite phase the mosaic spread of the crystal is around 1.7°. Additionally, a splitting at 200 Bragg peak has been observed which indicates the low quality of the single crystal.

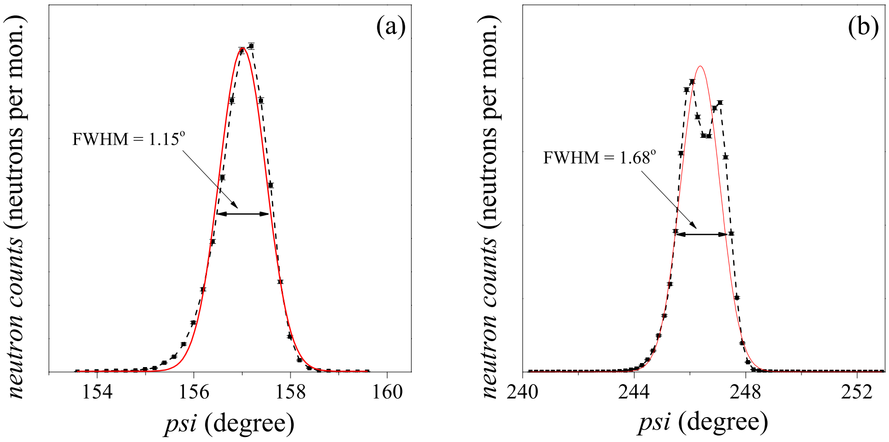

Figure 5.10: *Rocking curve measurements of (a) 5M martensite* $Ni_{50}Mn_{29}Ga_{21}$ *and (b) 7M martensite* $Ni_{49}Mn_{31}Ga_{20}$ *alloys aroung 200 Bragg peak. 7M marteniste measurements were done by T.Mehaddene. Mosaic spreads of 1.15° and 1.68° are observed for 5M and 7M samples, respectively for* $k_f = 2.662$ *Å.*

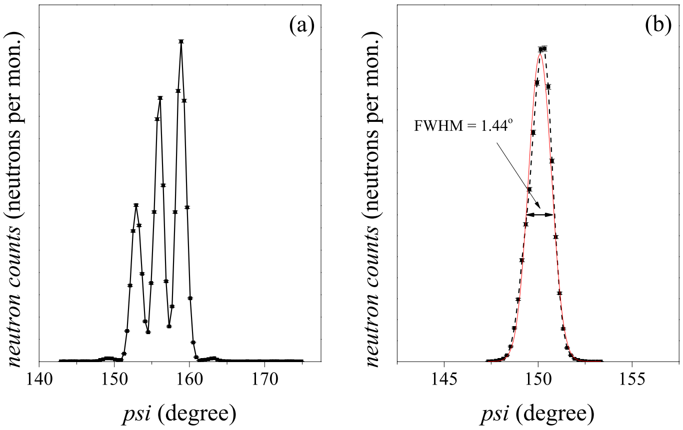

Figure 5.11: *Rocking curve measurements of* $Ni_{50}Mn_{30}Ga_{20}$ *alloy in the non-modulated martensite phase. (a) shows the measurement result before mechanical training of the sample. (b) denotes the measurement result after mechanical training. Measurements were done at room temperature with* $k_f = 2.662$ *Å. Trained sample shows mosaic spread of 1.44°.*

Chapter 6

Phonons in Ni-Mn-Ga Alloys

In this chapter, phonons of different Ni-Mn-Ga alloys are shown. Measured compositions and temperatures are summarized in Figure 6.1. In the figure, measured phonon dispersions are shown as star symbols for different compositions with corresponding temperatures. The measured phases of the phonon dispersions are shown as $L2_1$, 3M and 5M for austenite, premartensite and martensite phases, respectively. Colored symbols indicate the temperature dependent measurements of $TA_2[\xi\xi0]$ phonon modes. The austenite phase measurements of stoichiometric and offstoichiometric samples are shown as blue triangles, the premartensite and martensite phase measurements are depicted in red circles and green diamonds, respectively.

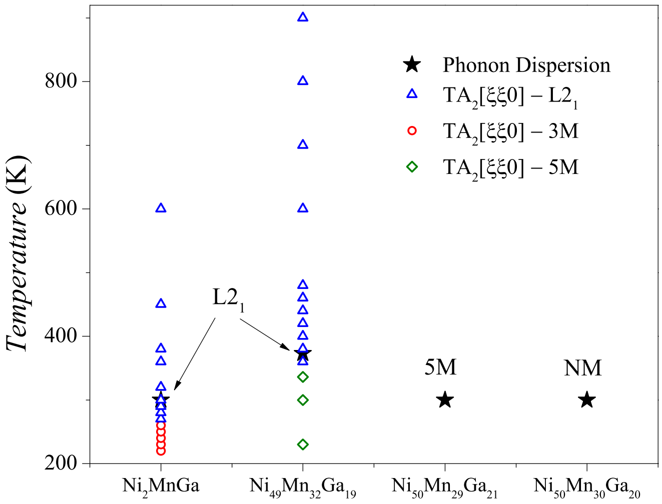

Figure 6.1: *Ni-Mn-Ga ferromagnetic shape memory alloys which are used in phonon investigations. Different colors correspond to different phases. 3M and 5M stand for premartensite and martensite phases, respectively. Star symbols indicate the phonon dispersion measurements of different compositions at corresponding temperatures.*

6.1 Phonon Dispersions in the Austenite Phases

Phonon measurements of the austenite phases have been carried out on both Ni_2MnGa and $Ni_{49}Mn_{32}Ga_{19}$ single crystals. Measurements of Ni_2MnGa have been carried out at room temperature where the single crystal is in the $L2_1$ phase. To obtain the austenite phase in $Ni_{49}Mn_{32}Ga_{19}$, first the single crystal was heated up to 673 K and cooled down to the measured temperature. The phonon dispersion of $Ni_{49}Mn_{32}Ga_{19}$ have been measured at 373 K. To measure the vibrational properties, different measurement directions have been selected. Figure 6.2 shows the first Brillouin zone of a face-centered cubic (fcc) structure. Full points in the figure indicate the high symmetry points of (ξ00), ($\xi\xi$0), ($\xi\xi\xi$) and the low symmetry point of (2$\xi\xi$0). The dotted lines are the symmetry directions of corresponding points. The phonon measurements have been carried out along these lines.

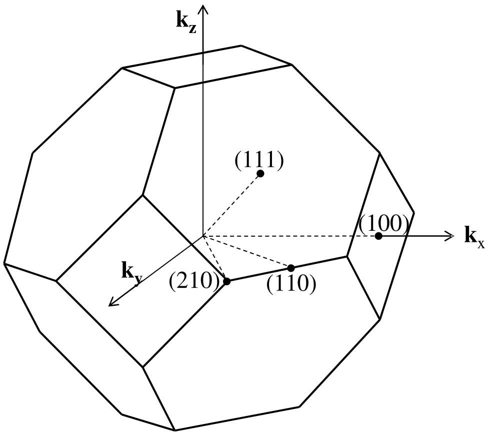

Figure 6.2: *First Brillouin zone of a face-centered cubic (fcc) structure. Thick solid lines show the boundaries of the first Brillouin zone. Points on the surface of the Brillouin zone indicate the symmetry points of fcc structure and dotted lines are the corresponding symmetry directions which are used for phonon measurements.*

Figure 6.3 shows a representation of the $hk0$ scattering plane with examples of phonon measurements along different high symmetry directions. Full circles correspond to Bragg positions which can create scattering intensities according to the selection rule of the fcc structure (for the fcc structure all of the hkl parameters have to be even or odd numbers). Open circles correspond to the forbidden Bragg positions. Due to the symmetry, it is possible to access two different measurement directions in the $hk0$ plane. Measurements from (020) to (030) yield information on the longitudinal phonon modes in the [100] direction which are named L[100]. In the same plane measurements perpendicular to L[100] give information about the transverse phonon modes in the [100] direction which are labeled T[100]. It is also possible to reach the [110] direction measurements in the $hk0$ scattering plane. Longitudinal and second transverse measurements respectively, are shown in Figure 6.3 with the labels L[110] and T_2[110]. Phonon measurements have been carried out in different Brillouin zones to reach the whole phonon dispersion within the limits of the experimental setup.

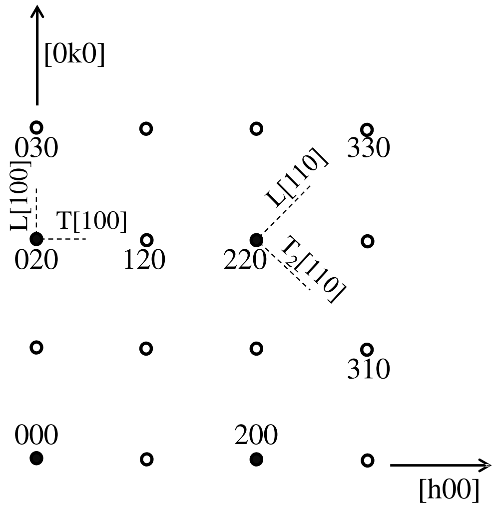

Figure 6.3: *Representation of the hk0 scattering plane. Solid circles and open circles indicate allowed and not allowed reciprocal lattice points, respectively. Dashed lines represent different phonon measurement directions.*

The basic unit cell of the austenite $L2_1$ phase consists of four atoms resulting in the observation of twelve phonon branches, three acoustic and nine optical. In the acoustic branches, one corresponds to the longitudinal mode and the other two to different transversal modes, which are perpendicular to the longitudinal mode and also to each other. The optical branches of phonons in the austenite phase consist of three different optical groups, each group has one longitudinal and two transversal branches similar to the acoustic branches. In the case of $[\xi 00]$ and $[\xi\xi\xi]$ measurements, two transversal branches are degenerate and only one transverse mode is observable for these measurement directions. In the $[\xi\xi 0]$ and $[2\xi\xi 0]$ directions, transversal branches are not degenerate due to the symmetry of the $L2_1$ phase, so two different transverse modes are observable in these symmetry directions.

6.1.1 Austenite Phonon Dispersion of Stoichiometric Ni_2MnGa

Phonon measurements of Ni_2MnGa have been carried out along the high symmetry directions of $[\xi 00]$, $[\xi\xi 0]$, $[\xi\xi\xi]$ and a lower symmetry direction of $[2\xi\xi 0]$ at room temperature. Results of the phonon measurements are shown in Figure 6.4 with the corresponding first-principles calculations by Siewert *et al.* [SGE12a]. In the figure, symbols and lines correspond to the experimental data and first-principles calculations, respectively. For the first-principles calculations different line shapes have been used to show different polarizations.

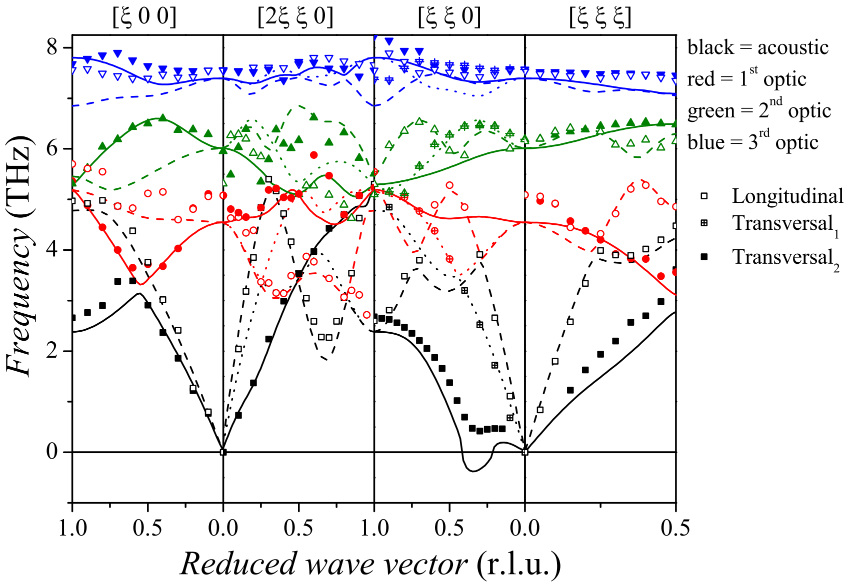

Figure 6.4: *Phonon dispersion of Ni_2MnGa for different symmetry directions of the $L2_1$ structure. Lines show the first-principles calculations of the stoichiometric sample which are taken from [SGE12a]. Symbols indicate the experimental results. The measurements were performed at room temperature and the first-principles calculations were done for absolute zero temperature.*

Phonon measurements have been carried out at room temperature and the first-principles calculations have been done for absolute zero temperature. Nevertheless, the overall agreement between the first-principles calculations and the experimental data is quite good. In both measurements and calculations the $TA_2[\xi\xi 0]$ phonon branch shows a softening feature. The minimum of the phonon softening is observed at $\xi = 0.33$ r.l.u. for both experimental measurements and first-principles calculations. For the first-principles calculations at 0 K, the $TA_2[\xi\xi 0]$ phonon branch exhibits imaginary phonon frequencies i.e. at 0 K the $L2_1$ structure is unstable. Regarding the optical modes, first-principles calculations show a gap around 7 THz. In the experimental results a gap of 0.55 THz is observed in the frequency region between 6.78 THz and 7.33 THz, which agrees with the first-principles calculations. There is a deviation between the experimental results and the first-principles calculations at the gamma point of the Brillouin zone and for the small ξ values of the first optical branch. The reason for this difference is mainly the effect of temperature. For the first-principles calculations, the phonon dispersion relations have been calculated for absolute zero temperature and the measurements have been performed at room temperature. The calculations of Zayak *et al.* show, that in the first-principles calculations imaginary phonons in the $TA_2[\xi\xi 0]$ phonon mode are associated with the T_{2g}-mode, which corresponds to the gamma point of the first optical modes [ZAER06].

This association between the TA_2 and T_{2g}-mode explains the difference between the measurements and calculations at the gamma points of the first optical modes. Due to this first-principles prediction, the first optical mode is expected to have higher frequencies in the T_{2g}-mode at finite temperatures, which agrees with our measurements. In the symmetry direction of $[2\xi\xi0]$, the calculations of the longitudinal acoustic mode show a wide oscillation in the whole reciprocal space in the frequency region of 2-5 THz. This wide oscillation has been confirmed by our finite temperature measurements.

6.1.2 Born-von Kármán Model Fit to the Ni_2MnGa

By using the Born-von Kármán model (BvK), a fit to the measured phonon dispersion of the austenite Ni_2MnGa has been performed. For the mathematical modeling, interactions up to the 9th nearest neighborhood (42 parameters) have been used, the results for the 42 parameters are given in Table 6.1. The BvK model fits are shown in Figure 6.5 along with the experimental data.

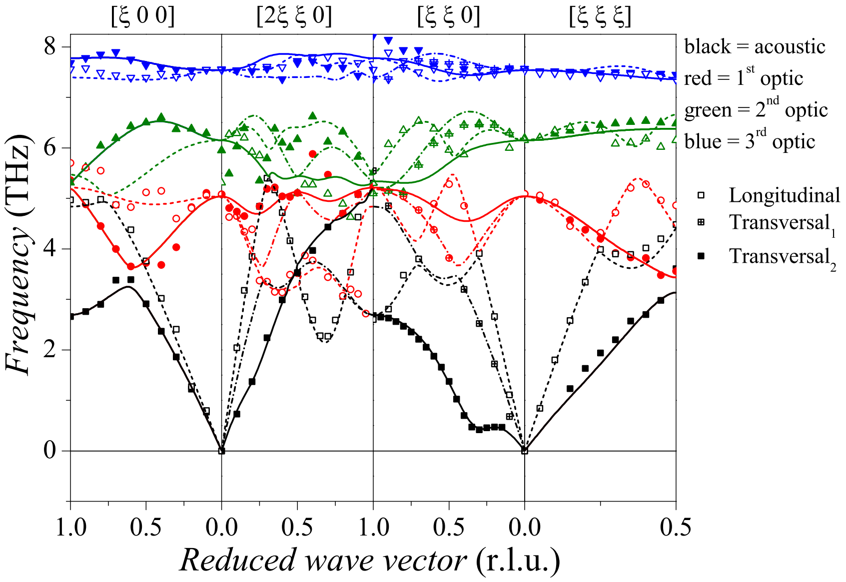

Figure 6.5: *Born-von Kármán model fit results of Ni_2MnGa sample. Symbols are the experimental results as shown in Figure 6.4. Lines are the Born-von Kármán model fit to the phonon dispersion.*

The agreement between the BvK model and experimental results is almost perfect. The softening at the $TA_2[\xi\xi0]$ phonon branch is perfectly reproduced with the used model. For all of the optical modes the agreement between the model and the measured dispersion is quite good. Despite the high number of fitting parameters there is a small deviation between the data and the model in the [2ξξ0] direction.

Table 6.1: Longitudinal (f_L) and transversal (f_T) force constants obtained from the Born-von Kármán model fit to the Ni_2MnGa at room temperature (300 K) as shown in Figure 6.5. "N.N." defines the nearest neighbor numbers, "Shell" indicates the number of shells which are taken into account. Force constants are in the unit of dyn/cm.

N.N.	Shell	Interaction	f_L	f_T
1	1	Ni_1-Mn	44342.40	852.90
2	1	Ni_1-Ga	33494.70	1217.60
3	2	Ni_1-Ni_2	217.30	-5876.80
4	2	Mn-Ga	9134.40	-734.60
5	3	Ni_1-Ni_1	-696.20	1247.20
6	3	Mn-Mn	9958.10	-1279.40
7	3	Ga-Ga	2326.70	-3838.50
8	4	Ni_1-Mn	-51.80	-180.60
9	4	Ni_1-Ga	2030.10	24.30
10	5	Ni_1-Ni_2	-4032.20	829.70
11	5	Mn-Ga	8945.60	-1115.10
12	6	Ni_1-Ni_1	-872.50	-134.80
13	6	Mn-Mn	-6715.10	2788.20
14	6	Ga-Ga	2257.60	444.10
15	7	Ni_1-Mn	-1038.30	-524.50
16	7	Ni_1-Ga	-773.20	980.20
17	8	Ni_1-Ni_2	831.80	966.70
18	8	Mn-Ga	-461.20	-578.70
19	9	Ni_1-Ni_1	210.40	-38.70
20	9	Mn-Mn	1332.00	-713.70
21	9	Ga-Ga	-1080.00	33.80

The total and the partial density of states are obtained from the Born-von Kármán fit results. Figure 6.6 shows the calculated vibrational density of states for the stoichiometric composition from the first-principles and the Born-von Kármán model. Black lines represent the total vibrational density of states. The partial density of states of nickel, manganese and gallium are shown as red, blue and green lines, respectively. Figure 6.6a corresponds to the first-principles calculations. The high frequency vibrations (third optical branches) are mainly dominated by manganese atoms and nickel atoms also contribute to these vibrations. The mid-frequency optical modes (second optical branches) are equally occupied by nickel and gallium atoms. Nickel atoms mainly occupy the low-frequency optical modes (first optical branches). In the low frequency vibrations region (acoustic mode region) all of the consisting atoms contribute to the vibrations.

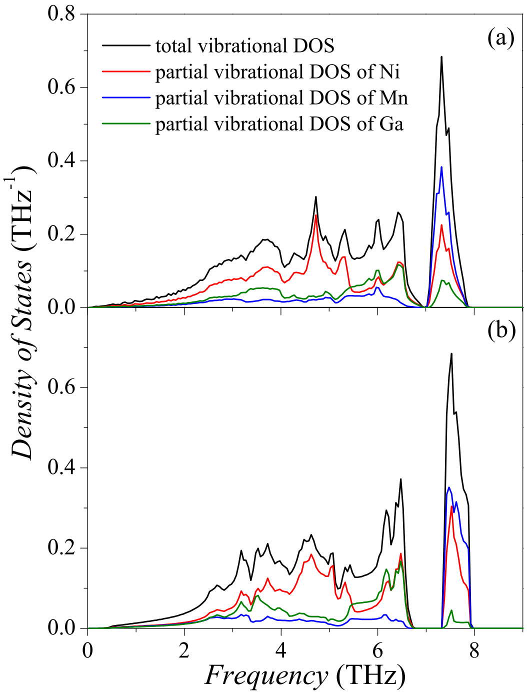

Figure 6.6: *Calculated density of states of stoichiometric* Ni_2MnGa. *a) shows the first principle calculations and b) corresponds to the Born-von Kármán fit calculations.*

Figure 6.6b shows the total and partial density of states calculations obtained from the Born-von Kármán model. The total density of states calculations exhibits the overall behavior of the phonon dispersion. High-frequency optical modes are well separated from the mid-frequency optical modes in agreement with Figure 6.5 (the gap between green and blue lines). The overall behavior of the total density of states shows similarities with the first-principles calculations within some deviations. In the Born-von Kármán model calculations, the high frequency optical modes are mainly occupied by manganese and nickel also contributes to these modes. Mid-frequency optical modes are half shared between nickel and gallium atoms. The low-frequency optical modes are mainly occupied by nickel atoms and all of the consisting atoms are contributing to the acoustic modes of the system. The main difference between the first-principles calculations and the BvK model fit is observed in the gap around 7 THz. The gap which is observed in the BvK model is wider compared to the first-principles predictions. This difference can be explained by the flatter distribution of the third optical modes in the measured phonon dispersion relations.

6.1.3 Austenite Phonon Dispersion of Offstoichiometric $Ni_{49}Mn_{32}Ga_{19}$

The austenite phonon dispersion of the offstoichiometric $Ni_{49}Mn_{32}Ga_{19}$ alloy has been investigated in the high symmetry directions of the $L2_1$ phase. The whole phonon dispersion relations have been measured to compare the effect of the offstoichiometry on the vibrational properties of the austenite phase. The color coding of the phonon dispersion is the same as explained for the stoichiometric composition in Chapter 6.1.1. The symbols show the experimental results of $Ni_{49}Mn_{32}Ga_{19}$ measured at 373 K and the solid lines are the same first-principles calculations of stoichiometric Ni_2MnGa for absolute zero temperature as shown in Figure 6.4.

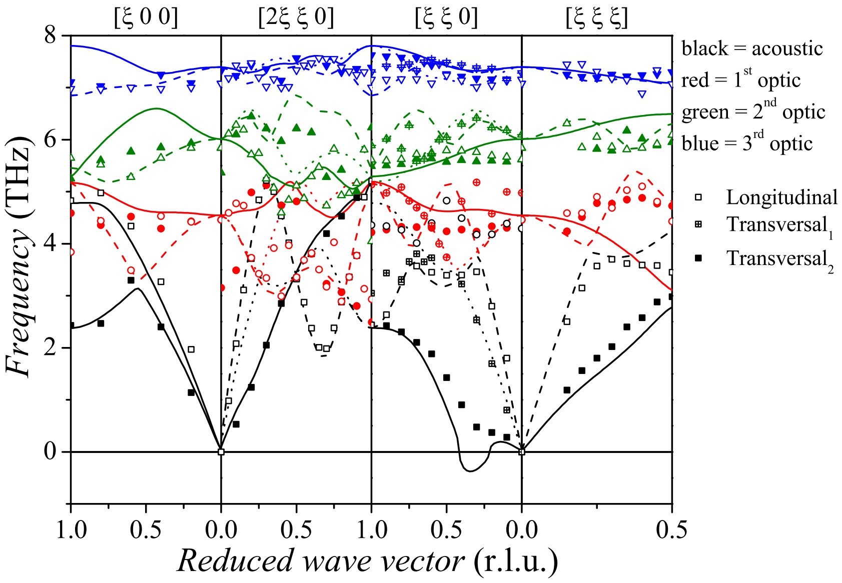

Figure 6.7: *Phonon dispersion of $Ni_{49}Mn_{32}Ga_{19}$ for the high symmetry directions of $L2_1$ structure. Lines show first principle calculations of stoichiometric Ni_2MnGa sample. Symbols indicate the experimental results at 373 K.*

First-principles calculations of the phonon dispersion relations of the offstoichiometric composition are not available presumably due to the need of large super cells which exceed todays computational power. Therefore, the offstoichiometric measurement results are compared to the stoichiometric calculations. Even though the comparison of different compositions, relation between theory and experimental results are in a qualitative agreement. In fact, the agreement between the acoustic modes are quite acceptable. In comparison to the stoichiometric measurements, optical modes in the offstoichiometric composition are less disperse which is attributed to different atomic interactions due to the offstoichiometry. In the low symmetry direction of [2ξξ0], the longitudinal acoustic branch shows oscillations in the 2-5 THz region in the whole reciprocal space similar to the stoichiometric composition.

6.1.4 Born-von Kármán Model Fit to the $Ni_{49}Mn_{32}Ga_{19}$

The measured phonon dispersion relations of the offstoichiometric $Ni_{49}Mn_{32}Ga_{19}$ alloy has been modeled by using the Born-von Kármán model. For the model, similar to stoichiometric composition interactions up to the 9th nearest neighborhood (42 parameters) have been used. Due to the manganese rich composition, the atomic weight and the scattering amplitudes have been corrected for the gallium. Elastic measurements (Chapter 5.1.4) show that 20.7 % of the excess manganese sits on the gallium site and due to this mixture of the manganese and gallium atoms, the effective atomic weight and the effective scattering amplitude of the gallium in the model changes. For the calculations atomic weight and scattering amplitude of the gallium have been changed to 66.91 g $mol^{-}1$ and 5.19 fm, respectively. The resulting BvK fit is shown in Figure 6.8 along with the experimental results.

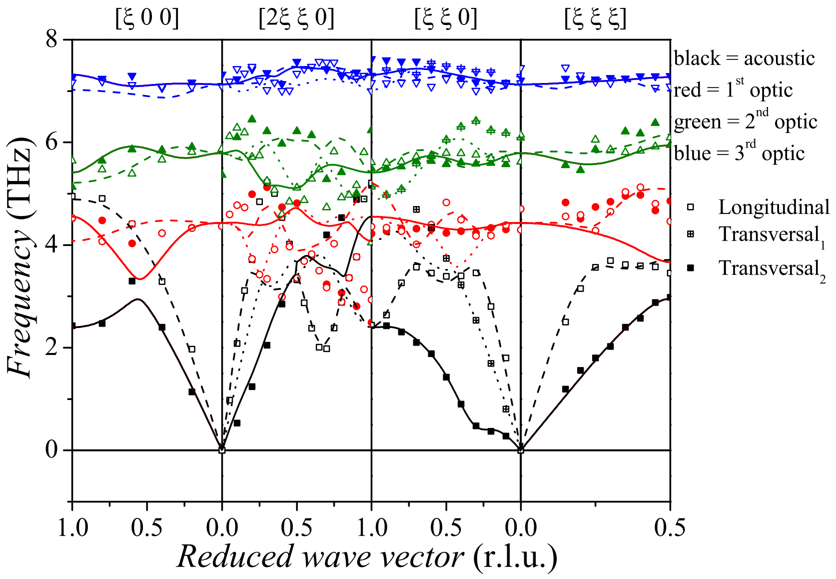

Figure 6.8: *Born-von Kármán model fit results of $Ni_{49}Mn_{32}Ga_{19}$ sample. Symbols are the experimental results as shown in Figure 6.7. Lines are the Born-von Kármán model fits to the experimental data.*

The calculated longitudinal and transversal force constants of the Born-von Kármán model of $Ni_{49}Mn_{32}Ga_{19}$ are shown in Table 6.2. The observed force constants of $Ni_{49}Mn_{32}Ga_{19}$ differ from the stoichiometric composition due to the different behavior of the phonon dispersion relations. In the offstoichiometric case, optical phonon modes are less disperse compared to the stoichiometric composition, this affects the force constants drastically.

Table 6.2: Longitudinal (f_L) and transversal (f_T) force constants obtained from the Born-von Kármán model fit to the $Ni_{49}Mn_{32}Ga_{19}$ at 373 K as shown in Figure 6.8. "N.N." defines the nearest neighbor numbers, "Shell" indicates the number of shells. The force constants are in the unit of dyn/cm.

N.N.	Shell	Interaction	f_L	f_T
1	1	Ni_1-Mn	36014.10	1963.10
2	1	Ni_1-Ga/Mn	25344.50	485.10
3	2	Ni_1-Ni_2	3206.10	-3716.00
4	2	Mn-Ga/Mn	-5940.20	782.90
5	3	Ni_1-Ni_1	-154.00	507.50
6	3	Mn-Mn	11722.90	-240.00
7	3	Ga/Mn-Ga/Mn	-1619.70	-2170.70
8	4	Ni_1-Mn	2759.70	-2266.80
9	4	Ni_1-Ga/Mn	3151.10	876.70
10	5	Ni_1-Ni_2	-7753.40	3707.40
11	5	Mn-Ga/Mn	10883.00	-2486.20
12	6	Ni_1-Ni_1	2950.50	2538.50
13	6	Mn-Mn	-3838.70	-1844.80
14	6	Ga/Mn-Ga/Mn	1210.10	-1960.00
15	7	Ni_1-Mn	-165.30	227.30
16	7	Ni_1-Ga/Mn	1225.30	-1034.20
17	8	Ni_1-Ni_2	189.40	-247.30
18	8	Mn-Ga/Mn	-1450.70	1356.80
19	9	Ni_1-Ni_1	-300.70	-156.50
20	9	Mn-Mn	3378.10	-1683.6
21	9	Ga/Mn-Ga/Mn	-2245.10	1023.50

The total and partial density of states calculations are shown in Figure 6.9 for the off-stoichiometric composition. Different line colors correspond to different contributions. Regarding the partial density of states of Ga this does not only correspond to Ga but a mixture of Ga and Mn atoms. The total density of states of $Ni_{49}Mn_{32}Ga_{19}$ perfectly shows the overall properties of the phonon dispersion. Similar to the Ni_2MnGa, high-frequency optical modes are well separated from the mid- and low frequency modes. High frequency modes are mainly occupied by the manganese atoms, mid-frequency modes are occupied by the nickel and gallium atoms, low frequency optical modes are occupied by nickel atoms. In the acoustic mode region all of the nickel, manganese and gallium atoms contribute to the vibration. The phonon density of states calculations of $Ni_{49}Mn_{32}Ga_{19}$ show sharper peak distributions due to the Van Hove singularities which are related with the observed flat phonon dispersion in the optical modes. Except for the observed Van Hove singularities, the overall behavior of the vibrational density of states resembles the stoichiometric composition.

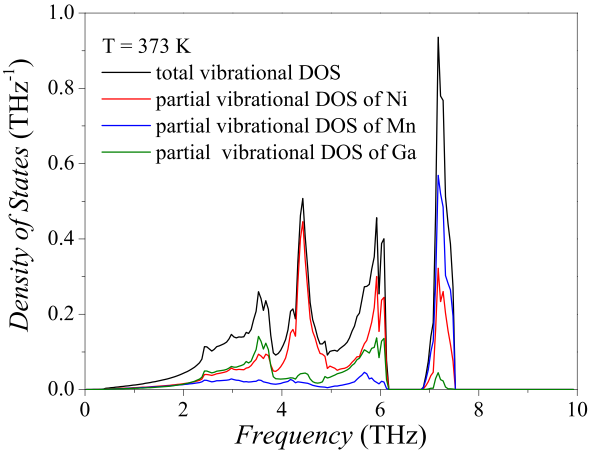

Figure 6.9: *Calculated density of states of off-stoichiometric* $Ni_{49}Mn_{32}Ga_{19}$ *from the Born-von Kármán model.*

6.2 Phonon Dispersions in the Martensite and Premartensite Phases

Low temperature, low symmetry phases of five-layered modulated martensite and non-modulated martensite phases have been investigated to compare the vibrational properties of these low symmetry phases with the measured vibrational properties in the high temperature, high symmetry phase. The five-layered modulated martensite (5M) phase measurements have been carried out on a mechanically trained single crystal with the chemical composition of $Ni_{50}Mn_{29}Ga_{21}$. The non-modulated (NM) martensite phase measurements have been carried out on a sample with a composition of $Ni_{50}Mn_{30}Ga_{20}$. NM and 5M martensite samples have been freshly trained before the inelastic neutron measurements as explained in Chapter 3.1 In addition to the martensite phase measurements, premartensite phase measurements of stoichiometric Ni_2MnGa have been carried out. The martensite phase measurements of 5M and NM samples have been carried out at room temperature without any sample environment. For the measurements of the premartensite phase, the stoichiometric austenite sample has been cooled down to 230 K where the sample is in the premartensite phase and no training has been applied to the sample.

6.2.1 Phonon Dispersion of $Ni_{50}Mn_{29}Ga_{21}$ in Five-Layered Modulated (5M) Martensite Phase

The vibrational modes of $Ni_{50}Mn_{29}Ga_{21}$ have been measured in different high symmetry directions of the five-layer modulated martensite phase at room temperature. In the martensite phase, due to the crystallographic anisotropy, the phonon dispersion relations have additional high symmetry directions compared to the austenite phase: $[00\xi]$ and $[0\xi\xi]$. As shown in Chapter 5.1.4, the c-axis of the 5M sample is the crystallographic short axis which creates these additional high symmetry directions. The measured phonon modes of $Ni_{50}Mn_{29}Ga_{21}$ are shown in Figure 6.10. The different color coding is used for determination of different phonon modes. In addition to the phonons, at higher frequencies (around 11-12 THz) additional inelastic signals have been observed, which can be attributed to magnons.

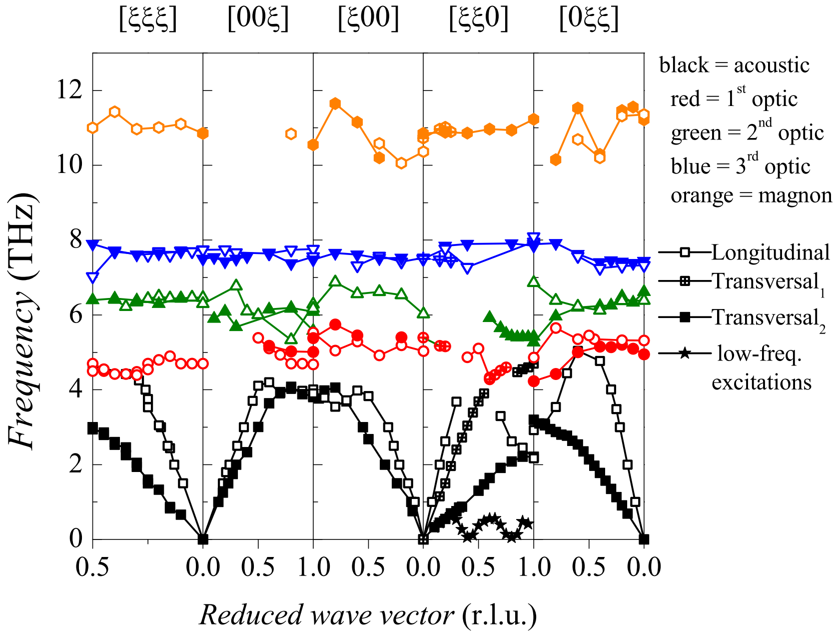

Figure 6.10: *Phonon dispersion of $Ni_{50}Mn_{29}Ga_{21}$ for the high symmetry directions of the 5-layer modulated martensite structure. Symbols indicate the measurement results which were carried out at 300 K.*

The overall vibrational properties of the martensite phase are similar to the properties of the austenite phase of similar composition. The optical modes show a flat distribution along the Brillouin zone as expected, similar to the austenite phase. In the $[\xi 00]$ and $[00\xi]$ directions, the observed transversal and longitudinal modes are lying in the same frequency region (around 4 THz). In the case of the $[\xi\xi 0]$ direction, the second-transversal and longitudinal modes meet at 2.2 THz, the same condition holds true at 3.1 THz for the $[0\xi\xi]$ direction. The difference at the zone boundary of the $[\xi\xi 0]$ and $[0\xi\xi]$ directions is due to the broken symmetry for these two directions. At the zone boundary, a strong anisotropy has been observed due to the tetragonal structure.

The observed high frequency inelastic signals are not related to the phonon dispersion but are also not coming from the experimental setup or from the sample environment. Initial first-principles calculations predict an optical-mode like magnon dispersion around this frequency region. Unfortunately, it is not possible to conclude unambiguously that the signals are related to the magnon dispersion of the martensite phase. To be sure about the conclusion, it is essential to redo the measurements with spin polarization analysis so that one can distinguish the magnetic signal from the nuclear one.

The softening, which is observed for the $TA_2[\xi\xi 0]$ phonon mode in the austenite phase, has been smeared out in the martensite phase. Additional to the hardening of the $TA_2[\xi\xi 0]$ phonon mode in the martensite phase, low frequency excitations have been observed along the $[\xi\xi 0]$ direction of 5M are discussed in the following (see the star symbols in Figure 6.10).

6.2.2 Phonon Dispersion of Non-modulated Martensite in $Ni_{50}Mn_{30}Ga_{20}$

Phonon measurements of the non-modulated (NM) martensite phase have been carried out at room temperature for two different high symmetry directions of the $Ni_{50}Mn_{30}Ga_{20}$ sample. These two high symmetry directions of the NM tetragonal phase are shown in Figure 6.11. The full symbols correspond to the measurements in transversal polarization and the open symbols are related to the measurements in longitudinal polarization. Different colors have been used to make it easier to distinguish different phonon modes.

The transverse polarization measurements along the $[\xi\xi 0]$ direction show a clear separation between the acoustic mode and the optical modes. Due to this reason it is possible to comment on that the optical modes seem to be decoupled from the differences in the acoustic region. Measured optical modes in the same polarization show little dispersion

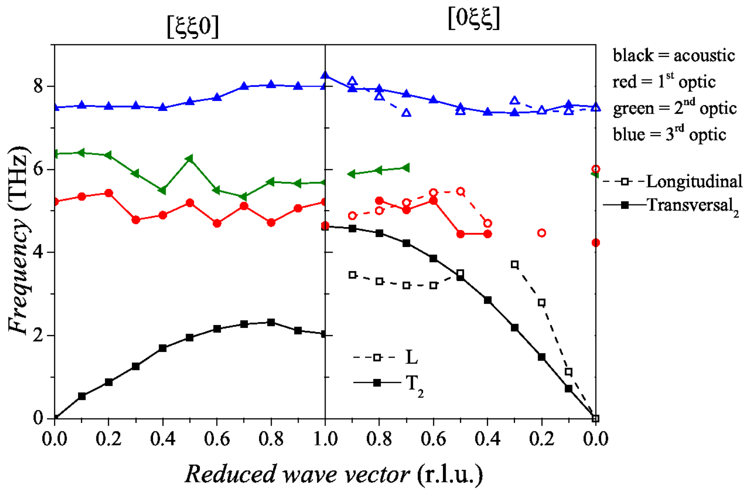

Figure 6.11: *Phonon dispersion of the non-modulated martensite of* $Ni_{50}Mn_{30}Ga_{20}$ *at room temperature in the [ξξ0] and [0ξξ] directions. Full and open symbols indicate transversal* (T_2) *and longitudinal (L) phonon measurements, respectively.*

along the Brillouin zone. Similar measurements along the [0ξξ] direction show no gap between the acoustic and optical modes. The comparison of the transversal modes shows that in the [0ξξ] direction the acoustic mode has a higher frequency compared to [ξξ0]. This kind of behavior has been observed for all martensite phases of Ni-Mn-Ga systems. At the zone boundary, due to the crystal symmetry, measured transverse modes show a gap similar to the gap observed in the 5M measurements.

6.2.3 Phonon Dispersion of Seven-Layer Modulated (7M) Martensite of $Ni_{49}Mn_{31}Ga_{20}$

The crystallographic investigations of seven-layer modulated (7M) martensite show, that the crystal has an orthorhombic structure at room temperature with the unit cell parameters of a=6.24 Å, b=5.78 Åand c=5.49Å[Meh07]. The vibrational properties of 7M marteniste phase of $Ni_{49}Mn_{31}Ga_{20}$ has been measured by T.Mehaddene. Figure 6.12 shows the acoustic phonon dispersion in the high symmetry direction of [0ξξ] and [ξξ0] for room temperature. The measurements of the TA_2[ξξ0] phonon mode show no softening feature. In addition to the [ξξ0] direction, [0ξξ] direction measurements show no softening feature. Due to the crystallographic asymmetry, the zone boundary conditions of the TA_2-modes differ for the [ξξ0] and the [0ξξ] directions. At the zone boundary, the low lying TA_2[ξξ0]-mode has a phonon frequency of 2.54 THz. In the case of the TA_2[0ξξ] zone boundary, the phonon has a frequency of 4.77 THz.

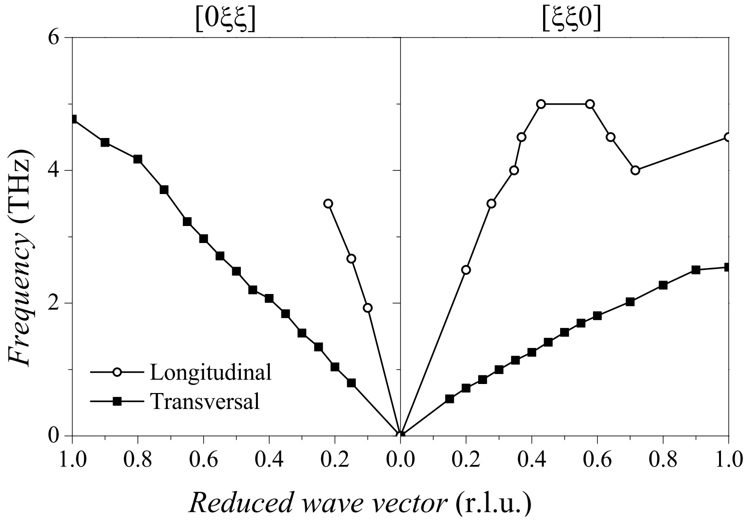

Figure 6.12: *Longitudinal and transversal acoustic modes of $Ni_{49}Mn_{31}Ga_{20}$ in the 7M martensite phase. Different symbols correspond to different polarizations in the measurements. The measurements were done at room temperature by T.Mehaddene [Meh07].*

6.2.4 Low Frequency Excitations of Martensite and Premartensite Phases

The low frequency region of the [$\xi\xi 0$] direction of 5M $Ni_{50}Mn_{29}Ga_{21}$ has been investigated in detail. Figure 6.13 shows the low frequency transfer region of the martensite phase along the [$\xi\xi 0$] direction. The color code shows the monitor normalized neutron counts in logarithmic scale. The peak maxima in the measured data are shown as red symbols and solid lines are added guide for the eye. For clarity, in the case of the low frequency excitations, a sinusoidal line shape has been used as a guide. Zero frequency transfer corresponds to elastic measurements, these measurements have been done to compare the elastic intensities with the previously existing data to prove the existence of commensurate modulation. The low frequency transfer measurements show inelastic signals existing in the whole Brillouin zone. Superstructure Bragg peaks have been observed at the commensurate positions of $\xi = 0.4$ r.l.u. and 0.8 r.l.u.

In the small ξ region it is not possible to distinguish the difference between the TA_2-mode and the low frequency excitations. At $\xi = 0.25$ r.l.u. the low frequency excitations and the TA_2-mode start to split. After this reciprocal point, the frequency of the TA_2-mode increases but the low frequency excitations oscillate in the frequency region below 0.6 THz for the whole Brillouin zone. Similar to the offstoichiometric martensite sample, the

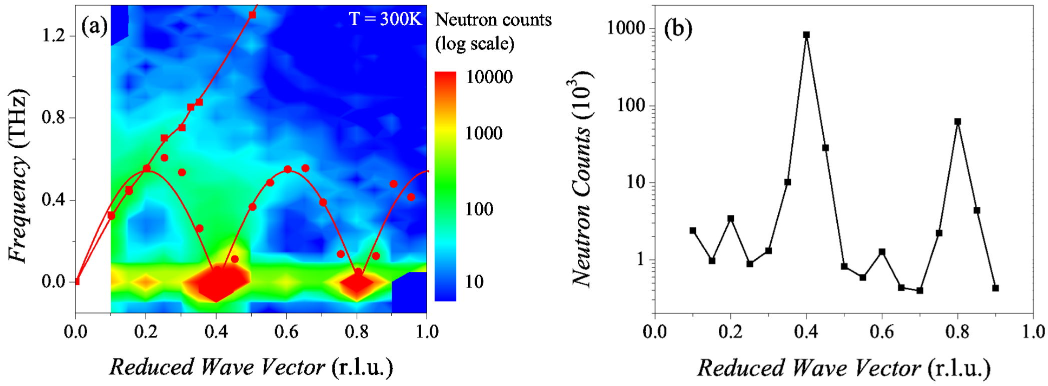

Figure 6.13: *(a)Low frequency inelastic neutron scattering measurements of* $Ni_{50}Mn_{29}Ga_{21}$ *in high symmetry direction of [ξξ0]. Measurements are done at room temperature. Color coding represents neutron intensities in logarithmic scale. The red symbols correspond to the peak maxima of the measured inelastic intensities and the lines are added as guide for the eye. (b) Elastic line cut along the transverse [ξξ0] direction.*

low frequency region of the stoichiometric Ni_2MnGa sample has been measured in the premartensite phase at 230 K, as shown in Figure 6.14.

In the premartensite phase, the superstructure peak lies at a commensurate position of ξ = 0.33 r.l.u., but the peak is not repeating itself at higher orders like ξ = 0.66 and 0.99 r.l.u. In the small ξ region it is not possible to distinguish the low energy excitations from the $TA_2[\xi\xi 0]$ phonon branch. The softening of the TA_2-mode approaches the superstructure peak of the premartensite phase but is not reaching zero frequency. In the premartensite case, around the phonon softening minimum, the measurements show an intensity between the soft phonon mode and the superstructure peak. Similar to the off-stoichiometric composition, in the premartensite case low energy excitation are observed up to ξ=0.6 r.l.u.

The low frequency transfer region in the transversal $[\xi\xi 0]$ direction of the $Ni_{49}Mn_{31}Ga_{20}$ alloy has been measured by T. Mehaddene [Meh07]. The measurements are shown as a contour plot in Figure 6.15a. In the seven-layered martensite (7M) phase, the low frequency measurements show no significant intensities around the superstructure Bragg peaks. The elastic line cut (Figure 6.15b) shows well defined super structure peaks at ξ = 0.3 and 0.6 r.l.u. values. The observed superstructure Bragg peaks are close to the expected values of ξ = 0.29 and 0.58 r.l.u. Compared to the 5M martensite and premartensite

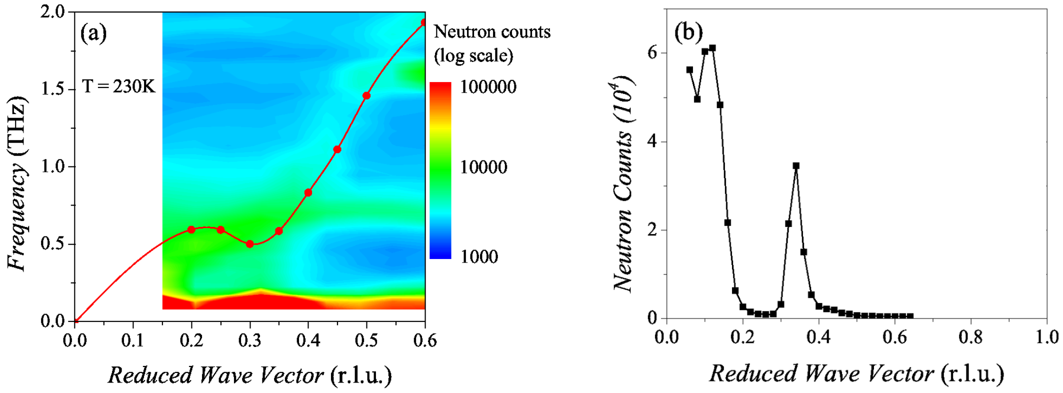

Figure 6.14: *(a)Low frequency inelastic neutron scattering measurements of* Ni_2MnGa *in the high symmetry direction* $[\xi\xi 0]$*. Measurements are done at 230 K. Color coding represents neutron intensities in logarithmic scale. The red symbols correspond to the peak maxima of the measured inelastic intensities and the lines are added as guide for the eye. (b) Elastic line cut along the transverse* $[\xi\xi 0]$ *direction.*

phase measurements, no significant intensities are observed in the 7M marteniste phase. This might be due to poor quality of the 7M martensite single crystal.

6.3 Temperature Dependence of the Softening in the Austenite Phases

The most interesting feature in the austenite phonon dispersion is observed in the $TA_2[\xi\xi 0]$ phonon modes, see Figures 6.5 and 6.8. Figure 6.16 shows a detailed study of the temperature dependence of the TA_2 phonon branch in Ni_2MnGa and $Ni_{49}Mn_{32}Ga_{19}$. For both compositions, the anomalous softening is visible even for the highest temperatures well above the phase transition temperature.

Figure 6.16a shows that in the stoichiometric composition the softening is restricted in a narrow interval of the reciprocal space (0.25 r.l.u. $\leq \xi \leq$ 0.45 r.l.u.). Phonon frequencies for higher ξ values remain unchanged. This holds true also for the premartensite phase, shown by the orange and brown symbols in Figure 6.16a. The softening behavior of the $TA_2[\xi\xi 0]$ phonon branch has been reported in literature for the stoichiometric composition [ZSW+95, ZSWT96]. In these studies, the temperature dependence of the soft mode has been intensively investigated around the magnetic ordering temperature. In the present study, the temperature range of measurements has been expended down to the lowest premartensite phase temperature.

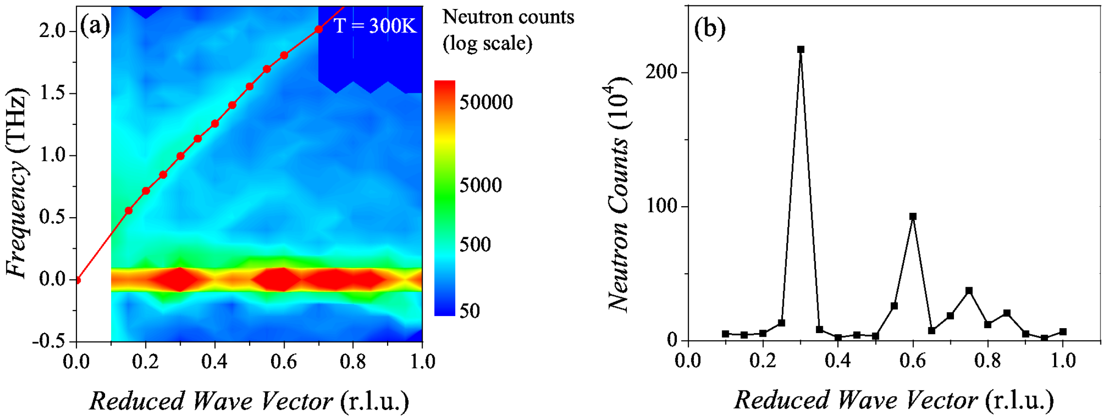

Figure 6.15: *(a)Low frequency region of the seven-layer modulated martensite of $Ni_{49}Mn_{31}Ga_{20}$ alloy in the [ξξ0] direction. Measurements are done at room temperature. Color coding represents neutron intensities in logarithmic scale. The red symbols correspond to the peak maxima of the measured inelastic intensities and the lines are added as guide for the eye. (b) Elastic line cut along the transverse [ξξ0] direction. The measurements were done by T. Mehaddene. [Meh07]*

The temperature dependence of the soft modes of $\mathrm{Ni_{49}Mn_{32}Ga_{19}}$ are shown in Figure 6.16b. Similar to the stoichiometric sample, in the austenite phase the softening is existing in a small reciprocal space interval (0.2 r.l.u. $< \xi <$ 0.5 r.l.u.). In the offstoichiometric composition, the observed softening is smeared out and less pronounced. In the martensite phase a slightly different behavior shows up, the entire phonon branch is at lower frequencies and the softening becomes even much less pronounced.

The question may arise whether the softening of the phonons stabilizes the austenite phase with respect to the martensite ground state. In the modified Landau expansion the square of the soft mode frequency is interpreted as an order parameter driving the transition [KG89]. The square of the frequency of the soft mode is expected to decrease linearly with temperature on approaching the phase transition temperature. Figure 6.17 shows such temperature-frequency plots for two different compositions of the austenite phases.

A linear behavior has been observed in the temperature dependence of the soft phonon frequency squares for both compositions. For the stoichiometric composition, Figure 6.17a, the slope of the phonon frequencies changes distinctly around the Curie temperature. In literature this coincidence has been interpreted with the onset of ferromagnetic

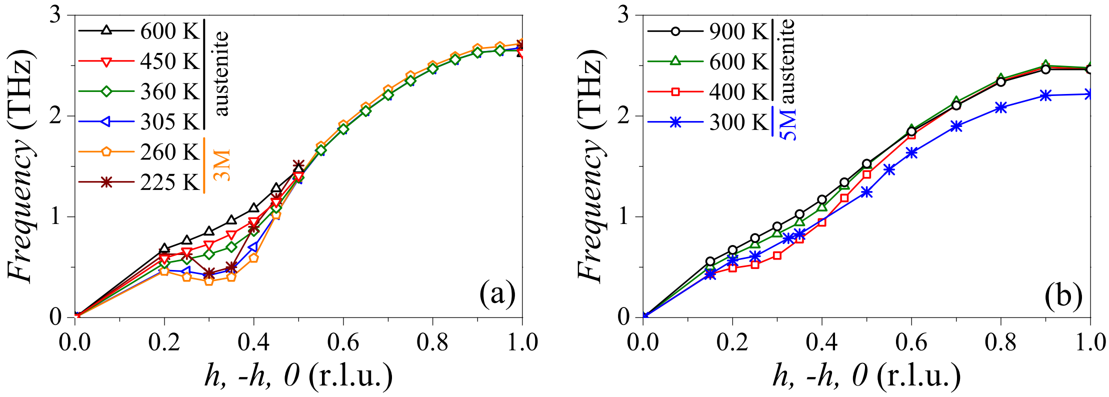

Figure 6.16: *Observed softening in the $TA_2[\xi\xi 0]$ phonon modes of (a) Ni_2MnGa and (b) $Ni_{49}Mn_{32}Ga_{19}$. Different colors correspond to different temperatures. Symbols correspond to measurements and lines in the austenite phases represent the Born-von Kármán model fits of the corresponding temperatures. In the 3M and 5M phases lines are added as a guide to the eye.*

ordering in the sample [SVKL97, MPZ$^+$01]. For the offstoichiometric composition, Figure 6.17b, the structural and magnetic transition temperatures are close. The change in the slope of the phonon frequency squared versus temperature, however, remains similar to the stoichiometric sample, i.e. about 100 K above the structural transition. This phenomenon is explained in detail by A. Planes *et al.* by means of magneto-elastic interactions [POGM97]. Further description can be bone by using the modified Landau theory, where the relation between temperature and soft phonon mode is described as [KG89, POGM97, Sha06]

$$\omega^2 = a(T - T_{critical}). \tag{6.1}$$

ω is the frequency of the soft phonon mode, T is the temperature and $T_{critical}$ is the structural transition temperature. In an ideal case, as expected from the modified Landau theory, at the structural transition temperature, the phonon frequency square reaches zero and for this reason, the transition temperatures of the high temperature phase to the low temperature phase and of the reverse transition must be at the same value. The measured phonon frequency squares are not reaching zero and due to this reason, the calculated structural transition temperatures differ for the austenite-premartensite and the reverse transitions. To estimate the structural transition temperatures of Ni_2MnGa, measurement results of $\xi = 0.35$ r.l.u. have been used. From a linear fit to the experimental results, the austenite to premartensite structural transition and the reverse transition temperatures have been calculated as 247.7 K and 314.4 K, respectively. For the offstoichiometric $Ni_{49}Mn_{32}Ga_{19}$, Figure 6.17b, the structural transition (T_M=361 K) and

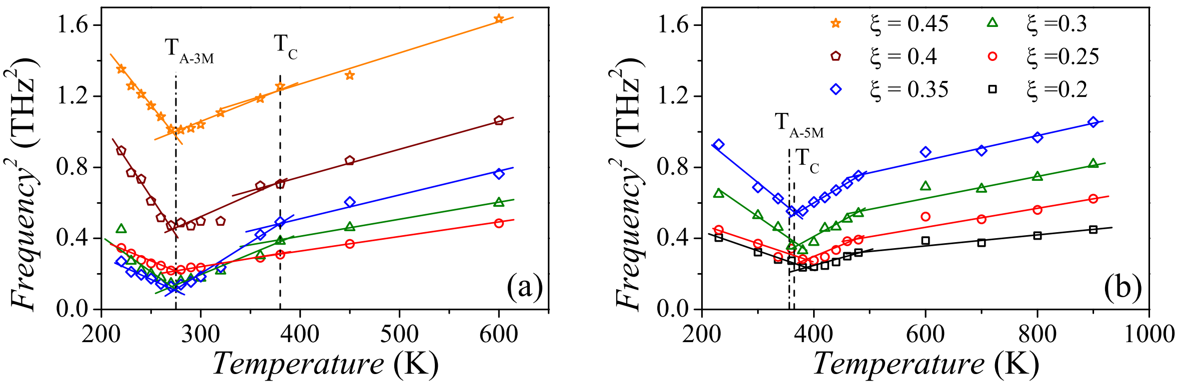

Figure 6.17: *Phonon frequency squares as a function of temperature for different ξ values of (a) Ni_2MnGa and (b) $Ni_{49}Mn_{32}Ga_{19}$. T_{A3M} and T_{A5M} define the structural transition temperatures of stoichiometric and offstoichiometric compositions, respectively. Above these temperatures, the alloys have $L2_1$ Heusler structure. Below these temperatures, Ni_2MnGa has 3-layered modulated premartensite and $Ni_{49}Mn_{32}Ga_{19}$ has 5-layer modulated martensite phase. The solid lines are a guide to the eye. T_C represents the Curie temperatures for both stoichiometric and offstoichiometric compositions.*

magnetic ordering (T_C=371 K) temperatures are close to each other. The slope change which has been observed around 500 K is not corresponding to the Curie temperature of the $Ni_{49}Mn_{32}Ga_{19}$. The structural transition temperatures of $Ni_{49}Mn_{32}Ga_{19}$ have been calculated from the modified Landau model. Due to the shallow slopes around the structural transition temperature, the obtained temperatures lie in a wide temperature range. The austenite to martensite transition and the reverse transition temperatures have been observed as 249.1 K and 755.3 K, respectively.

6.4 Composition and Phase Dependence of $TA_2[\xi\xi 0]$

Previous studies showed that the $TA_2[\xi\xi 0]$ phonon mode has a special importance in the structural transitions of the Ni-Mn-Ga alloys. The comparison of the $TA_2[\xi\xi 0]$-modes in different compositions and phases is shown in Figure 6.18. The measurement results show that all of the measured $TA_2[\xi\xi 0]$-modes lie in a similar frequency region. The austenite phase measurements show a strong phonon softening in a particular region of the reciprocal space ($\xi \leq 0.5$ r.l.u.) but the softening becomes less pronounced in the modulated martensite phase and totally disappears in the NM marteniste phase. Besides an additional softening feature has been observed at the zone boundary condition of the $TA_2[\xi\xi 0]$-modes of NM martensite.

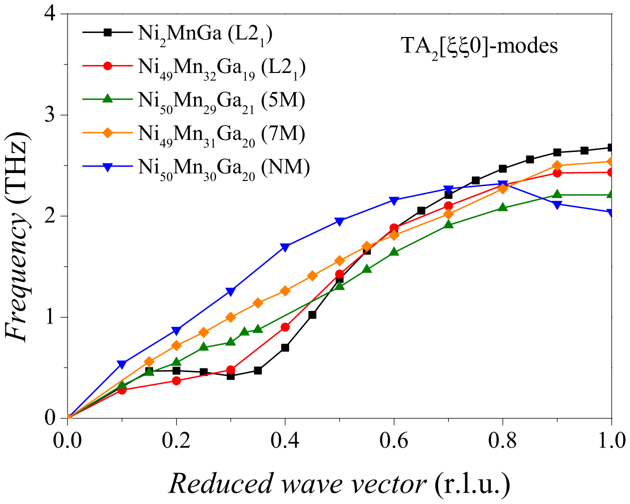

Figure 6.18: *Measured TA$_2$[ξξ0] soft phonon modes in different compositions and phases. Phases are given for each corresponding composition. All of the measurements were done at room temperature except for $Ni_{49}Mn_{32}Ga_{19}$ (L2$_1$). The measurements of $Ni_{49}Mn_{32}Ga_{19}$ (L2$_1$) were done at 373 K.*

First-principles calculations predict that the non-modulated martensite phase is the stable phase at 0 K. Due to this reason no phonon softening is expected in this phase. Our measurements confirm that there is a softening at the zone boundary condition of TA$_2$[ξξ0] mode of the NM marteniste phase. Additionally, the observed phonon frequencies of the TA$_2$[ξξ0] phonon in the NM martensite phase are increased compared to the modulated martensite and austenite phases.

Chapter 7

Discussions

7.1 Crystallographic Structures of Austenite and Martensite Phases

The Rietveld refinement results of the offstoichiometric compositions in austenite and martensite phases were given in Chapter 5.1.4. In the austenite phase of $Ni_{49}Mn_{32}Ga_{19}$ (at 600 K) a face-centered cubic structure is observed in agreement with the literature [WZTP84]. Refinement results show that nickel atoms occupy only nickel sites (X-sites) and due to excess manganese, manganese atoms occupy both manganese (Y-sites) and gallium (Z-sites) sites. Gallium atoms occupy only the gallium sites. Similar features have been observed in many different offstoichiometric compositions of Ni-Mn-Ga. In the excess manganese case, manganese atoms which are sitting in the gallium site are interacting anti-ferromagnetically with the neighboring manganese atoms. This anti-ferromagnetic interactions have been modeled by first-principles and observed experimentally for different Ni-Mn-based alloys [AAD+09, ESG+12, AAK+12, HKC12].

The martensite phase of the offstoichiometric Ni-Mn-Ga is confirmed as five-layer modulated martensite by Rietveld refinement for the room temperature measurements. The refinement results show, the low temperature martensite phase is not a real tetragonal phase but has a monoclinic structure. The crystallographic properties of this structure was given in Table 5.6. As the unit cell parameters of a and b are the same in the error bars and differs from c, the crystal structure can be treated as a tetragonal structure. In the phonon investigations, for convenience, the 5M crystal has been treated as a tetragonal phase. For this structure, modulation vector is defined as $\mathbf{q}= 0.4$ r.l.u. which agrees with literature. Righi *et al.* showed that, in an offstoichiometric Ni-Mn-Ga sample, the modulation in the five-layered martensite phase has a commensurate modulation vector of

q= 0.4 r.l.u. with a similar monoclinic structure [RAP+07]. Additionally, there are some other studies which show incommensurate modulations of the five layer and seven layer modulated martensite phases [RAC+06, RAV+08, RAP+09]. A sinusoidal modulation has been used in the Rietveld refinements. However, it has been shown in the literature that, a zigzag-like modulation can also be used for explaining the modulated structure. Figure 7.1 shows a schematic representation of these two different modulation modes in Ni_2MnGa.

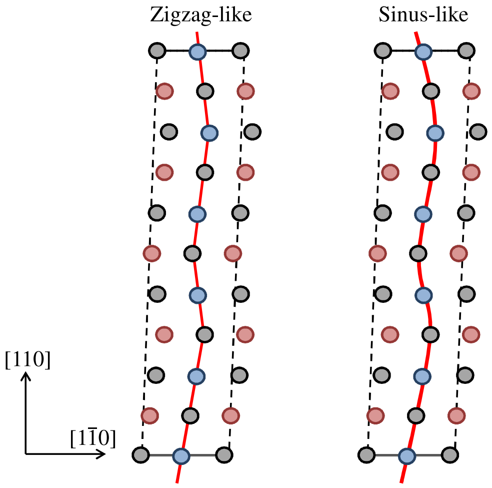

Figure 7.1: *Schematic represent of zigzag-like and sinus-like modulation of Ni-Mn-Ga alloys along [110] direction.*

7.2 Vibrational Properties of Austenite Phases

Ni-Mn-Ga alloys are the most investigated ferromagnetic shape memory alloys due to their prototype and unique shape memory properties. In literature the structural transition properties of these materials have been investigated by using wide range of different methods [WZTP84, GCOM+99, WCG+01, ZSW98, KTB+01, CPSC02, VBK+99, PMA09]. The most important feature which is observed in the Ni-Mn-based alloys is the tunability of the structural and the magnetic properties of these materials by changing the chemical compositions. Many of these Heusler structures can be tuned to undergo a diffusionless, displacive, first order martensite transition. This kind of structural transitions are generally associated with phonon anomalies in high temperature high symmetry phases. Vibrational properties of similar transitions have been investigated for transition metals which have bcc structure in the high temperature phases. These mono-atomic elements show a strong softening in L[$\xi\xi\xi$] and $T_2[\xi\xi0]$ phonon modes. The phonon dispersion investigations of mono-atomic elements of Ti [PHT+91], Hf [THP+91], Zr [HPT+91], La [GPS+93], Cr [TPH93] and Sc [PTH93] show strong phonon softening in the aforementioned phonon modes. In addition to the mono-atomic systems, Ni-based binary alloys show similar softening features which are attributed to the charge density waves [SSSW84, ZH92, SLN$^+$86].

The acoustic phonon dispersion of the stoichiometric Ni_2MnGa alloy has initially been measured by Zheludev *et al.* and a strong softening in the $TA_2[\xi\xi 0]$-mode has been observed [ZSW$^+$95]. After this observation, phonon dispersion of the austenite phase and effect of temperature on the softening properties of $TA_2[\xi\xi 0]$ phonon modes have been intensively investigated. In this work, to compare the austenite phases of the stoichiometric and offstoichiometric compositions, whole phonon dispersion of stoichiometric Ni_2MnGa has been measured. Measured phonon dispersion agrees with the existing phonon measurement data in the literature with some minor differences. The agreement between the first-principles calculations and the measured phonon dispersion is perfect for the acoustic modes and deviates a little bit in the optical modes. These small deviations are attributed to the small compositional changes and temperature differences between the calculations and measurements.

In order to derive thermodynamic properties, a Born-von Kármán (BvK) model has been used to fit the phonon dispersion in the austenite phase. The total and partial density of states were calculated from the force constants obtained by the BvK model. To see the effect of temperature on the vibrational properties, phonon dispersions have been fit to the BvK model for different temperatures. First-principles calculations predict a temperature dependent change only in the TA_2 and T_{2g}-modes. Previous investigations of Mehaddene *et al.* showed that at finite temperatures the T_{2g}-mode has no significant temperature dependence as expected from the theory [TJ07]. Due to this reasons, for our temperature dependent calculations, only the TA_2-modes have been changed for corresponding temperatures. For temperature dependent calculations, BvK model fits were applied to these modified phonon dispersions. Total vibrational density of states (vDOS) obtained from the model are shown in Figure 7.2 for different temperatures. From these calculated vDOS , in the harmonic approximation, mean square displacements, Debye temperatures and Debye frequencies have been calculated for corresponding temperatures. These calculation results are summarized in Table 7.1.

The calculated vDOS show no significant temperature dependence. Temperature dependent measurements of $TA_2[\xi\xi 0]$ phonon mode show a strong softening at ξ=0.33 r.l.u. but the weight of this softening is not strong enough in 4-dimensional space to influence the vDOS. Compared to the mono-atomic systems, in the case of Ni-Mn-Ga, TA_2 phonon mode does not show a significant effect on the overall vibrational properties.

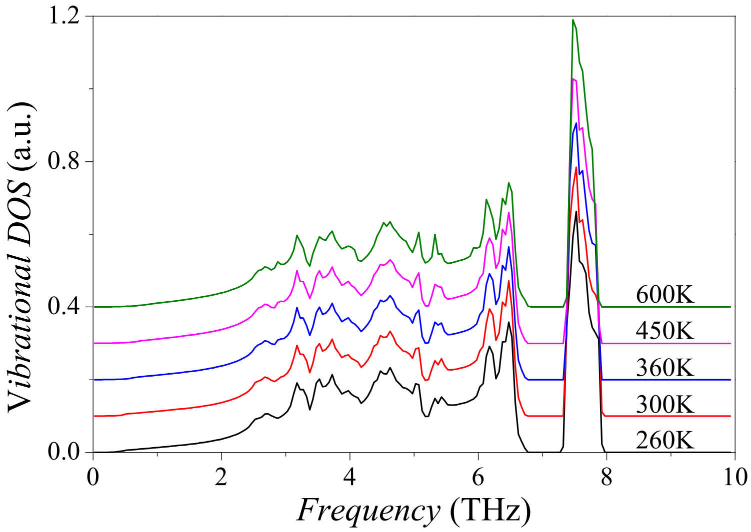

Figure 7.2: *Calculated vibrational density of states of stoichiometric Ni_2MnGa for different temperatures. Different colors depict different temperatures and the plots are shifted for clarity.*

Table 7.1: Temperature dependent thermodynamic properties of Ni_2MnGa calculated from the density of states obtained by the Born-von Kármán model. $< u_x^2 >$ corresponds to the atomic mean square displacement of the molecule and constituent elements (x = Ni_2MnGa, Ni, Mn and Ga), Θ_D refers to the Debye temperature and ν_D corresponds to the Debye frequencies.

Temp (K)	$< u^2_{Ni_2MnGa} >$ (x10^3 $\AA^2$)	$< u^2_{Ni} >$ (x10^3 $\AA^2$)	$< u^2_{Mn} >$ (x10^3 $\AA^2$)	$< u^2_{Ga} >$ (x10^3 $\AA^2$)	Θ_D (K)	ν_D (THz)
260	6.64	3.26	1.80	1.60	307	6.39
300	7.51	3.74	1.97	1.82	310	6.45
360	8.66	4.36	2.20	2.10	316	6.59
450	10.58	5.37	2.64	2.57	320	6.66
600	13.69	7.00	3.40	3.32	324	6.76

The vibrational entropies (S_{vib}) of the Ni_2MnGa have been calculated from the vDOS and the results are shown in Figure 7.3. Here, for the S_{vib} calculations three different approaches have been used. In the first approach, vibrational density of states resulting from the first-principles calculations are used - solid line in the figure (taken from [SGE12a]). Second, the Born-von Kármán fitted dispersion is used and the lattice entropy is calculated and harmonically extrapolated from this value in the shown temperature interval. The latter approach is named and plotted as harmonic approach in the figure. Third, measurements of the phonon dispersion at different temperatures have been used to calculate vDOS and the vibrational entropies for corresponding temperatures. The last approach is called and plotted as quasi-harmonic approach.

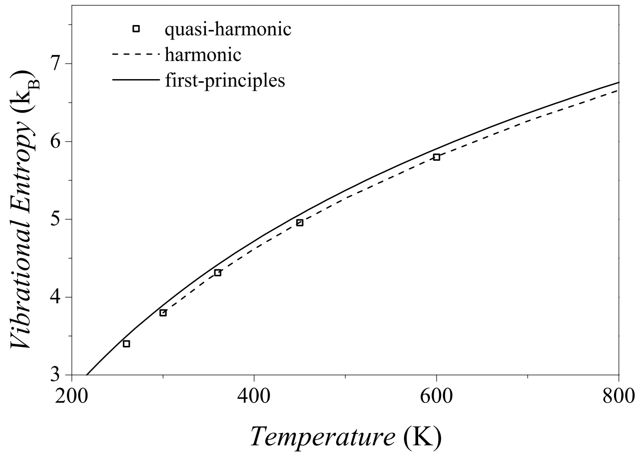

Figure 7.3: *Vibrational entropy calculations of Ni_2MnGa in the quasi-harmonic (open dots) and in the harmonic (dashed line) approximations. The quasi-harmonic approximation entropies are calculated from the density of states at the corresponding temperature. Harmonic entropies are extrapolated from the room temperature density of states. Solid line depicts the first principle calculations obtained using the harmonic approximation.*

All approaches end up in minor variations with respect to temperature dependence of the vibrational entropies. Since the quasi-harmonic vibrational entropy calculations do not deviate quantitatively from the harmonic vibrational entropies, it can not be concluded that the vibrational entropy stabilizes the high temperature phase. This differentiates the Ni-Mn-Ga system from mono-atomic metals like Zr, Cr and La [HPT$^+$91, GPS$^+$93, TPH93]. In the case of mono-atomic elements, changes in the longitudinal and transversal modes affect the vibrational density of state drastically. Compared to these mono-atomic systems in the Ni-Mn-Ga alloys, a very narrow region of the reciprocal space shows a pronounced softening and its effect of this softening is not so strong in the 4-dimensional space as in the pure elements.

Constant volume heat capacities of stoichiometric Ni_2MnGa are also calculated and shown in Figure 7.4. Here the results obtained from the phonon dispersion are compared with the theoretical calculations of Guo-Liang *et al.* [GLJDD$^+$09]. Similar to the vibrational entropy calculations the heat capacity calculation also agrees well with the first-principles calculations.

The elastic constants and the sound velocities are calculated from the initial slopes of the acoustic modes of Ni_2MnGa at room temperature. The fundamental relation between acoustic modes and elastic constants are listed in Table 7.2 for a cubic structure. For the calculations, the initial slopes of the acoustic branches are fitted by the following equation,

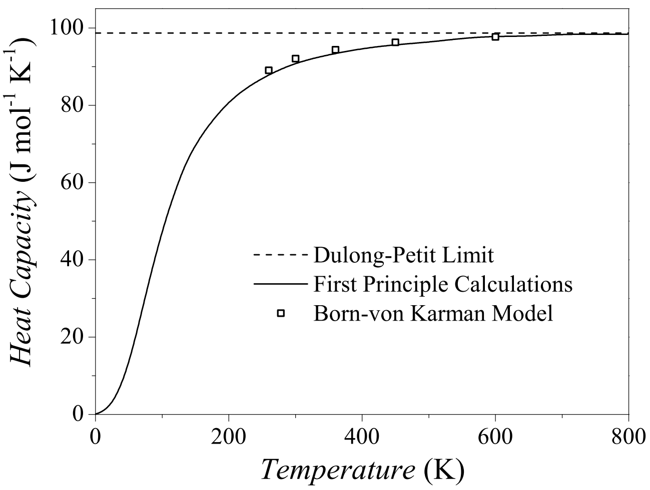

Figure 7.4: *Temperature dependence of the constant volume heat capacities (C_v) of stoichiometric Ni_2MnGa. Open symbols depict the calculated heat capacities from the Born-von Kármán model, solid line shows the theoretical calculations from [GLJDD+09] and the dashed line corresponds to the Dulong-Petit limit of the Ni_2MnGa.*

$$C_x = \rho v_y^2 \tag{7.1}$$

where C_x shows different elastic constants and v_y^2 corresponds to the sound velocity of a phonon modes as defined in Table 7.2. For the stoichiometric Ni_2MnGa calculations, the density of ρ=8.155 g/cm^3 has been used. Table 7.3 shows the calculated elastic constants for stoichiometric Ni_2MnGa at room temperature with comparison to the literature values. In this study, as the elastic constants are directly calculated from the initial slope of the acoustic modes of the dispersion, deviations of the calculations are strongly dependent on the resolution of the spectrometer at given point in the reciprocal space.

Table 7.2: Relation between the acoustic phonon modes and elastic constants for the high symmetry directions of the cubic phase [Kit86].

in [100] direction	in [110] direction	in [111] direction
$L : C_{11}$	$L : \frac{1}{2}(C_{11} + C_{12} + 2C_{44})$	$L : \frac{1}{3}(C_{11} + 2C_{12} + 4C_{44})$
$T : C_{44}$	$T_2 : \frac{1}{2}(C_{11} - C_{12}) = C'$	$T : \frac{1}{3}(C_{11} - C_{12} + C_{44})$
	$T_1 : C_{44}$	

In the experimental work of Vasilev *et al.*, electromagnetic generation technique has been used for the determination of the elastic constants [VKSC90]. Differently from this technique in the experimental studies of Worgull *et al.* and Mañosa *et al.*, pulse echo technique has been used for the elastic constant determination [WPT96, MGCO+97]. For the theoretical calculations, the standard approach in the first-principles framework has been

Table 7.3: Elastic constants of Ni-Mn-Ga alloys at room temperature obtained from the phonon measurements and the comparison with the literature values. The elastic constants are in the units of 10^{12} dyn/cm^2.

	C_{11}	C_{44}	C_{12}	C'	C_L
Present study - Exp.	1.67	1.15	1.18	0.25	2.58
Ref.[VKSC90] - Exp.	2.13	0.92	0.87	0.63	2.42
Ref.[WPT96] - Exp.	1.52	1.03	1.43	0.045	2.80
Ref.[MGCO+97] - Exp.	1.36	1.02	—	0.22	2.22
Ref.[BRC03] - Theory	1.53	1.00	1.48	0.025	2.51
Ref.[KC10] - Theory	1.63	1.07	1.52	0.055	2.65

used by Bungaro *et al.* [BRC03]. In the work of Kart *et al.* additional to the standard approach, total energies have been calculated as a function of the strain [KC10]. The comparison of the literature values and the present work shows that, the observed results differ considerably from each other. Elastic constant determination by phonon measurements uses relatively small wavelength sound propagations of the corresponding phonon branch. In these measurements, the obtained wavelength is defined by the resolution of the instrument at the corresponding point. Ultrasonic measurements use larger sound wavelengths. Due to this reason, results obtained from phonon measurements differ from the literature values. The lowest elastic constant value is observed for C' which corresponds to the low lying TA$_2$[$\xi\xi0$] phonon branch. Additional to room temperature measurements, temperature dependence of the elastic constants were investigated and the results are shown in Table 7.4.

The main difference is expected in the C' elastic constant which is related with the TA$_2$[$\xi\xi0$] phonon branch. The calculations show that, the softening which is observed at the particular region of the reciprocal space (around ξ=0.33 r.l.u.) does not effect the C' elastic constant of Ni$_2$MnGa. In other words, the C' elastic constant does not alter significantly with temperature but TA$_2$[$\frac{1}{3}\frac{1}{3}0$] does. The investigation of Mañosa *et al.* shows that the elastic constants of the stoichiometric Ni$_2$MnGa mainly changes at the martensite transition temperature (T$_M$ = 230 K) [MGCO$^+$97]. Above this transition temperature, elastic constants stays roughly constant and at the structural transition C' and C_{44} values decrease significantly. Our calculation results obtained from phonon measurements confirm the ultrasonic measurement results of Mañosa *et al.* From these results,

Table 7.4: Elastic properties of Ni_2MnGa for different temperatures. Temperatures are in K, elastic constants are in the unit of 10^{12} dyn cm^{-2}, average sound velocities are in km s^{-1}, bulk and shear modulus are in GPa.

Temperature	C_{11}	C_{44}	C_{12}	C'	C_L	<V>	Bulk Modulus	Shear Modulus
260	1.69	1.21	1.14	0.27	2.62	3.08	132.56	83.34
300	1.67	1.15	1.18	0.25	2.58	2.98	134.59	78.75
360	1.66	1.13	1.19	0.24	2.56	2.97	134.48	77.58
450	1.66	1.13	1.18	0.24	2.55	2.98	134.13	77.10
600	1.62	1.17	1.12	0.25	2.54	3.04	128.78	80.12

we can conclude that shear is not triggering the premartensite transition and shuffling of the neighboring planes plays an important role.

Similar to the stoichiometric composition, to calculate the thermodynamic properties, BvK model has been used to model the phonon dispersion of $Ni_{49}Mn_{32}Ga_{19}$. To see the effect of temperature on the vibrational properties, different $TA_2[\xi\xi0]$-modes have been used in the BvK models for different temperatures. The calculated vDOS obtained from the BvK models are presented in Figure 7.5 for different temperatures.

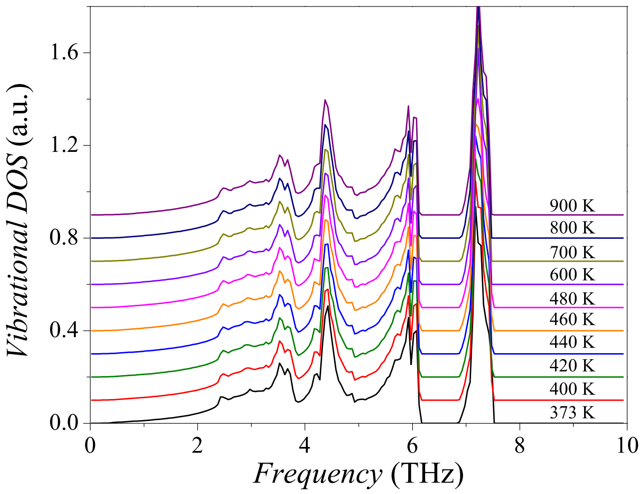

Figure 7.5: *Calculated vibrational density of states of offstoichiometric $Ni_{49}Mn_{32}Ga_{19}$. Different colors depict different temperatures and the plots are shifted for the clarity.*

As the TA_2-mode has a small contribution to the 4-dimensional integral, temperature variations do not change the features of the vibrational density of states drastically. With these calculations, it is confirmed that in both stoichiometric and offstoichiometric compositions $TA_2[\xi\xi0]$ phonon mode has no significant effect on the vDOS. Due to the computational difficulties it is not easy to find an offstoichiometric Ni-Mn-Ga calculation in the literature. Despite this, Siewert *et al.* were able to calculate the offstoichiometric $Ni_8Mn_5Ga_3$ composition just by changing a gallium atom with a manganese one in the unit cell [SGE12b]. The composition of the resultant alloy ($Ni_{50}Mn_{31.25}Ga_{18.75}$) is similar to the measured offstoichiometric composition but without any random atomic distribution in the calculated cell. Figure 7.6 shows the vDOS calculation results of $Ni_8Mn_5Ga_3$ taken from [SGE12b]. Due to the additional manganese atom, the unit cell of the structure changes and this creates additional phonon branches which are not observable in our phonon measurements. These additional phonon modes create a crowded phonon dispersion and also a complicated vDOS.

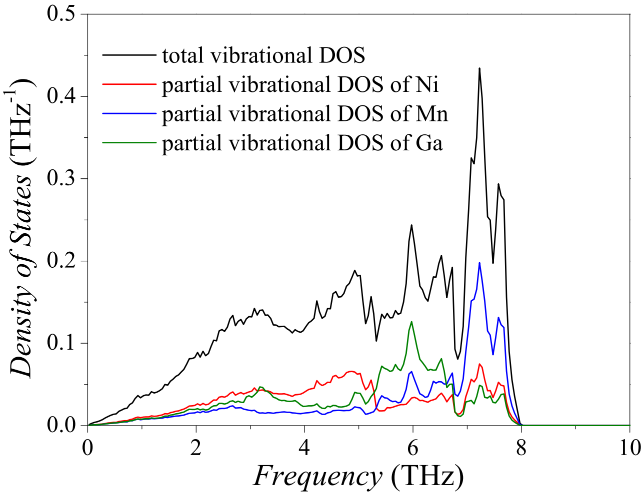

Figure 7.6: *Vibrational density of states calculation of $Ni_8Mn_5Ga_3$ from the first-principles calculations. Black color represents total density of states, colored lines depict partial density of states of different atoms. Figure is taken from reference [SGE12b].*

Due to the crowded phonon dispersion, some of the features of vDOS obtained from first-principles differ from the measurements. For example the clear gap, which is observed for the stoichiometric composition around 7 THz region, is not existing anymore. Instead of that, around 6.9 THz the total vDOS shows a dip. The phonon dispersion calculations of the offstoichiometric composition give so many unrealistic branches, or in other words these branches are not observable in the measurements. Due to this reason, vDOS obtained from the first-principles calculations gives broader vDOS distribution which dissipates the gap between the second and third optical modes. The calculations obtained from the BvK model rely on the experimental facts, so these calculations are more reliable. Besides the different total vDOS behavior, nevertheless, first-principles calculation predict right partial vDOS distribution which agrees with the experiment results. High frequency vibrations which are around 8 THz, are mainly occupied by manganese atoms.

Table 7.5: Thermal properties of $Ni_{49}Mn_{32}Ga_{19}$ for different temperatures. Temperatures are in K, atomic displacements are in 10^3 $\AA^2$, Debye temperatures are in K and Debye frequencies are in THz.

Temperature	$<u^2>_{Ni}$	$<u^2>_{Mn}$	$<u^2>_{Ga}$	$<u^2>_{Ni_2MnGa}$	Θ_D	ν_D
373	4.75	2.45	2.64	10.03	301.55	6.28
400	5.05	2.52	2.82	10.61	303.65	6.32
420	5.28	2.60	2.95	11.05	304.84	6.35
440	5.52	2.71	3.08	11.54	305.32	6.36
460	5.66	2.80	3.18	11.87	307.82	6.41
480	5.86	2.90	3.30	12.30	308.90	6.43
600	7.19	3.54	4.04	15.07	312.00	6.49
700	8.38	4.13	4.72	17.58	312.03	6.50
800	9.46	4.68	5.34	19.89	313.60	6.53
900	10.58	5.21	5.97	22.23	314.65	6.55

The mid-frequency region is occupied mainly by gallium atoms and the low frequency optical modes are occupied by nickel atoms and all atoms contribute to the acoustic region.

Temperature dependent thermodynamic properties of offstoichiometric $Ni_{49}Mn_{32}Ga_{19}$ have been calculated from the BvK model fits and the results are shown in Table 7.5. As expected, with increasing temperature, atomic displacements increase for the whole molecule and consisting elements.

Similar to the stoichiometric composition, vibrational entropies have been calculated in three different approaches. Figure 7.7 shows the results of the harmonic first principle calculations (solid line), harmonic (dashed-line) and quasi-harmonic (symbols) calculations obtained from BvK model. For the harmonic approximation, vibrational density of states of 373 K is harmonically extrapolated to higher temperatures. For the theoretical calculations, $Ni_8Mn_5Ga_3$ composition has been used in the harmonic model [SGE12b].

In the offstoichiometric $Ni_{49}Mn_{32}Ga_{19}$, similar to the stoichiometric composition, quasi-harmonic and harmonic models do not deviate. This behavior indicates that in the offstoichiometric composition, the vibrational entropy alone is not enough for the stabilization of the austenite phase. For the stabilization of the high temperature phase of $Ni_{49}Mn_{32}Ga_{19}$, additional to vibrational entropy, magnetic (and/or electronic) entropy play a role.

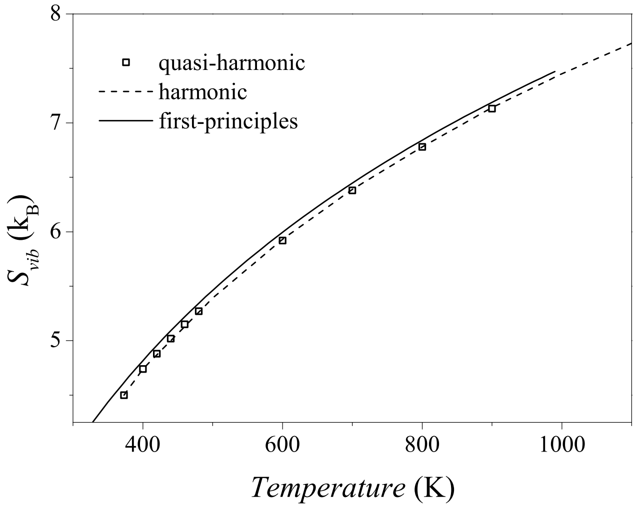

Figure 7.7: *Vibrational entropy calculations of offstoichiometric $Ni_{49}Mn_{32}Ga_{19}$. Open dots and dashed line represents calculation results of quasi-harmonic and harmonic approximations, respectively. Solid line depicts the first principle calculation results of $Ni_8Mn_5Ga_3$.*

Figure 7.8 shows the calculated lattice contribution to the heat capacities. Constant volume heat capacities of $Ni_{49}Mn_{32}Ga_{19}$ for different temperatures have been calculated directly from the BvK model fit and are indicated as open symbols in the figure. Solid line shows the first-principles calculation of the offstoichiometric $Ni_8Mn_5Ga_3$. The theoretical calculations and the experimental results agree quite well for the offstoichiometric composition. This behavior is expected due to the good agreement between the vibrational entropies.

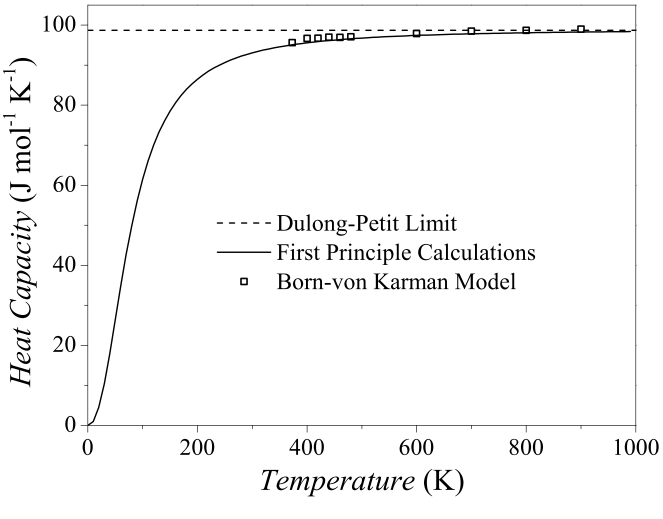

Figure 7.8: *Temperature dependence of the constant volume heat capacities (C_v) of offstoichiometric $Ni_{49}Mn_{32}Ga_{19}$. Open scatters depict the calculated heat capacities from the Born-von Kármán model, solid line shows the theoretical calculations from [SGE12b] and the dashed line corresponds to the Dulong-Petit limit of the Ni_2MnGa.*

The elastic constants and the sound velocities of $Ni_{49}Mn_{32}Ga_{19}$ were calculated from the initial slopes of the acoustic modes. Table 7.6 summarizes the obtained results of these calculations. For these calculations the density of 8.055 g/cm^3 was used. As expected,

Table 7.6: Elastic properties of $Ni_{49}Mn_{32}Ga_{19}$ for different temperatures. Temperatures are in K, elastic constants are in 10^{12} dyn cm^{-2}, average sound velocities are in km s^{-1}, bulk and shear modulus are in GPa.

Temperature	C_{11}	C_{44}	C_{12}	C'	C_L	<V>	Bulk Modulus	Shear Modulus
373	2.402	1.075	2.115	0.144	3.334	2.662	221.046	70.234
400	2.396	1.068	2.151	0.123	3.342	2.577	223.312	68.992
420	2.393	1.067	2.153	0.120	3.340	2.567	223.354	68.843
440	2.395	1.066	2.151	0.122	3.339	2.577	223.232	68.822
460	2.418	1.059	2.099	0.160	3.318	2.722	220.557	69.934
480	2.420	1.058	2.082	0.169	3.309	2.758	219.473	70.232
600	2.436	1.047	2.050	0.193	3.290	2.839	217.879	70.544
700	2.426	1.047	2.046	0.190	3.283	2.841	217.239	70.414
800	2.432	1.042	2.007	0.213	3.262	2.913	214.896	71.014
900	2.430	1.039	1.986	0.222	3.247	2.948	213.443	71.241

the main difference is observed in elastic constant of C'. Different from the stoichiometric composition, in the $Ni_{49}Mn_{32}Ga_{19}$, the softening is smeared out in the **q**-space. Due to this smeared out nature, the softening can be observed at smaller ξ values which effects the initial slope of the TA_2-phonon mode. The obtained results show an increase in the C' elastic constant with increasing temperature. Despite this fact, the temperature dependent change in the rest of the elastic constants is not so significant. From this observation we can conclude that, compared to the stoichiometric composition, in the offstoichiometric sample the shear plays a role in the structural transition. This kind of shear effect is expected for the $Ni_{49}Mn_{32}Ga_{19}$ because the observed structural transition is a real martensite transition.

7.3 Temperature Dependence of the $TA_2[\xi\xi0]$ Phonon Modes

The austenite $TA_2[\xi\xi0]$ phonon mode attracts interest after the observation of the softening at room temperature. Our studies on soft $TA_2[\xi\xi0]$ phonon modes show temperature dependent softening for both Ni_2MnGa and $Ni_{49}Mn_{32}Ga_{19}$ compositions. The temperature dependence of the near stoichiometric Ni-Mn-Ga alloys have been studied intensively in the literature. Figure 7.9 shows an abstract of the existing literature in comparison with the austenite samples studied in this work. To make a clear comparison, temperatures are normalized to the Curie temperatures of the alloys. In Figure 7.9a, mainly near stoichiometric compositions are shown around their Curie temperatures (T_C) and all of these alloys exhibit slope changes around T_C. Measurement results of Ni_2MnGa and $Ni_{49}Mn_{32}Ga_{19}$ are shown in Figure 7.9b. The stoichiometric composition show a slope change around its T_C similar to the literature. In the case of $Ni_{49}Mn_{32}Ga_{19}$ the slope change does not correspond to the magnetic ordering temperature.

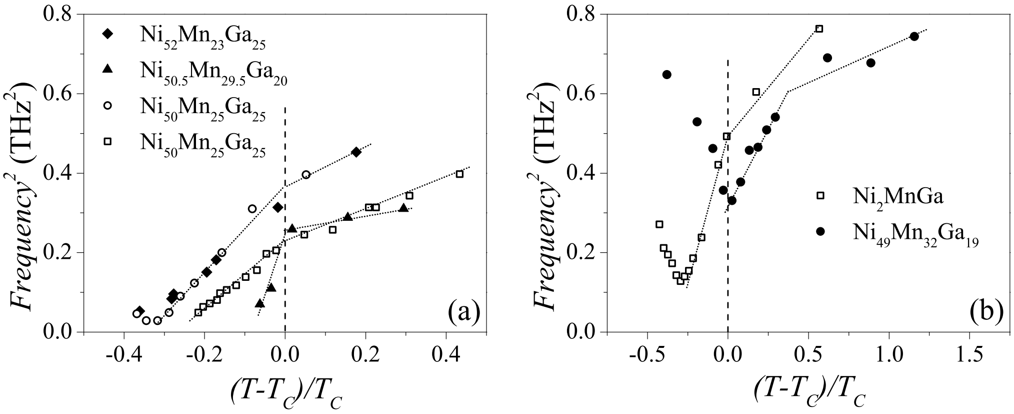

Figure 7.9: *Squared phonon frequencies of TA$_2$[ξξ0] phonon around the Curie temperatures of Ni-Mn-Ga alloys. Different symbols correspond to different composition. Temperature axis is normalized to the Curie temperatures of the alloys. (a) The existing literature values (Figure is adapted from [MPZ+01]). (b) The measurement results of Ni_2MnGa for $\xi=0.35$ r.l.u. and $Ni_{49}Mn_{32}Ga_{19}$ for $\xi=0.3$ r.l.u.*

For the stoichiometric or near-stoichiometric compositions, it is possible to find many articles which investigate the relation between the soft phonon mode and the magnetic ordering, but the relation between the structural transition and the phonon frequencies have not been investigated as detailed as magnetic transitions. To my knowledge, only existing investigation literature around the structural transition was carried out by Zheludev *et al.* [ZSW+95]. The measurement results of these study are shown in Figure 7.9a as open circles. For the low temperature region of the graph, squared phonon energies are increasing but the temperature interval in the premartensite phase is too small to allow an interpretation. To improve the knowledge in the premartensite phase, in the present study, the phonon frequencies of the soft mode have been measured down to 220 K which is the lowest accessible temperature in the premartensite phase of our Ni_2MnGa composition. For Ni_2MnGa measurements, approaching to the premartensite transition temperature, squared phonon frequencies decrease for all ξ values around the softening minimum. The highest softening is observed at ξ= 0.35 r.l.u. which is the closest measured reciprocal space point to the softening minimum of $\xi = \frac{1}{3}$ r.l.u. Despite the decrease in the phonon frequency square, it is not reaching to zero as expected from the modified Landau theory. The reason of this feature is explained by the phonon-phonon interactions. Hickel *et al.* showed that, the softening of the TA_2-mode is strongly affected by the phonon-phonon interactions [HUAZ+12]. Similar coupling between TA_2-modes and T_{2g}-modes was reported in [ZAER06]. Figure 7.10a shows the first-principles predictions on the behavior of the soft mode as a function of temperature for Ni_2MnGa by Hickel *et al.* [HUAZ+12]. For comparison experimental results of Ni_2MnGa for ξ=0.35 r.l.u. are given in Figure 7.10b.

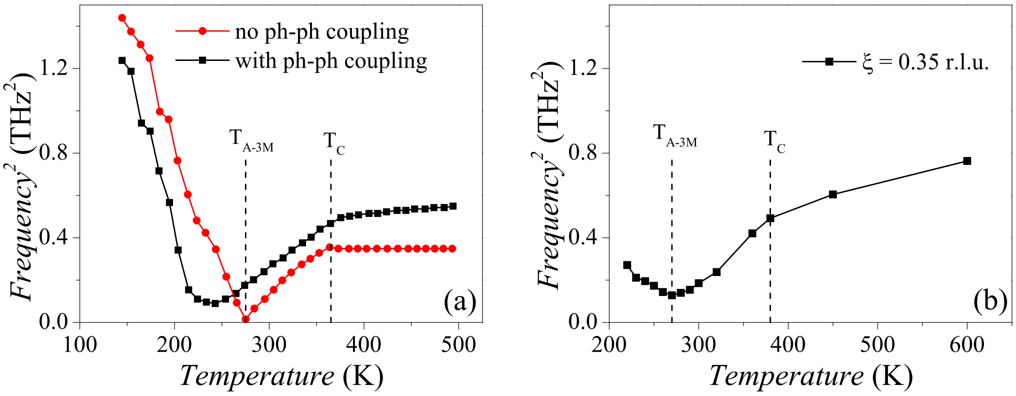

Figure 7.10: *(a) Calculation results of temperature dependence of squared soft mode frequencies. The black symbols and red symbols indicate calculation results with and without phonon-phonon interactions, respectively. The figure is taken from [HUAZ+12]. (b) phonon frequency square of Ni_2MnGa for ξ=0.35 r.l.u. Dashed lines indicate critical transition temperatures.*

In Figure 7.10a, red symbols indicate the calculation results without taking phonon-phonon interactions into account. The slope of the phonon mode is changing around 380 K which agrees with the Curie temperature of the stoichiometric sample and around the structural transition temperature, the phonon frequencies are reaching to zero and increasing again in the premartensite phase. When phonon-phonon interactions are taken into account (black symbols), again the slope of the soft phonon mode is changing around Curie temperature as expected but the real difference is occurring around the structural transition temperature. The squared phonon frequencies are not reaching to zero anymore around the structural transition temperature but creating a minimum. These first-principles calculation results fit perfectly with present study and the literature. Transition temperatures can be calculated from the slopes of the phonon modes. The austenite to premartensite transition temperature of 266 K is observed with the slope of $a = 0.0338$ THz^{2}K^{-1} and the reverse transformation temperature of 273 K with $a = 0.0117$ THz^{2}K^{-1} without phonon-phonon coupling. The transition temperatures with phonon-phonon coupling, changes to 222 K with $a = 0.0033$ THz^{2}K^{-1} and 238 K with $a = 0.0015$ THz^{2}K^{-1} for austenite-to-premartensite and reverse transition, respectively. The first-principles calculations show that the phonon-phonon coupling shifts the transition temperature to a lower value than the real transition temperature. The slopes of the phonon modes do not change so much and slope of the austenite-to-premartensite transition agrees with the present experimental result. In the premartensite phase, calculations show a sharper increase compared to the present results.

Similar to the softening minimum, it is also possible to compare the zone boundary vibrational properties of the TA$_2$[$\xi\xi$0] phonon modes. Figure 7.11 compares the stoichiometric and the offstoichiometric TA$_2$[$\xi\xi$0] phonon modes at zone boundary conditions (ξ=1 r.l.u.). In Figure 7.11a, the temperatures are normalized to structural transition temperatures, and in Figure 7.11b temperatures are normalized to Curie temperatures.

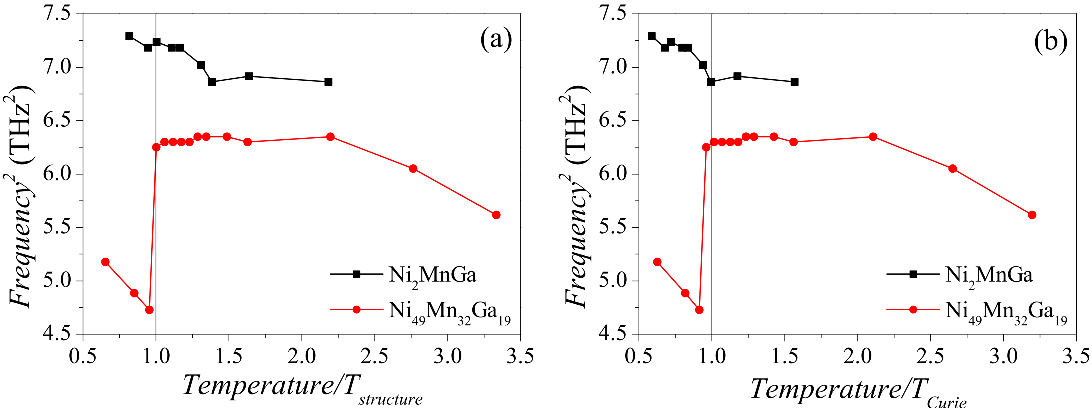

Figure 7.11: *Temperature dependence of the TA$_2$-mode at the zone boundary (ξ=1.0 r.l.u.). Squares indicate the measurement results of Ni_2MnGa and circles show the $Ni_{49}Mn_{32}Ga_{19}$ measurements. The temperature axes are normalized to (a) structural transition temperature and (b) Curie temperature.*

Figure 7.11a shows the zone boundary frequency changes of the TA$_2$-mode around the structural transition temperatures. These results clearly show that the structural transition affects the zone boundary condition of the offstoichiometric composition. In the austenite phase the zone boundary phonons lie around the 6.2 THz region and when the martensite transition occurs the phonon frequencies decrease rapidly and increase again with further decreasing temperature. This is not the case for stoichiometric composition. Around the premartensite transition temperature the phonon frequencies lie around 7.2 THz and the premartensite transition does not affect these phonon modes. Figure 7.11b shows the effect of magnetic ordering on the vibrational properties of TA_2-mode at the zone boundary. In the stoichiometric sample the magnetic ordering changes the zone boundary frequency of the TA_2-mode. In the paramagnetic region the phonon frequencies lies around 6.8 THz region but when the ferromagnetic ordering is achieved the phonon frequencies increase and reach the value of 7.2 THz. The effect of ferromagnetic ordering on the offstoichiometric composition is not so strong. The magnetic ordering temperature of the $Ni_{49}Mn_{32}Ga_{19}$ is too close to the structural transition temperature and due to this reason, the zone boundary phonon measurements do not show any significant changes in the ferromagnetic region of the austenite phase.

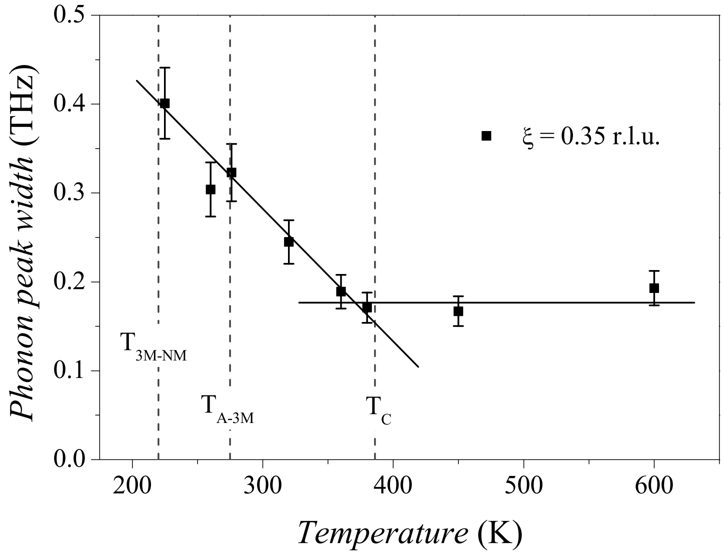

Figure 7.12: *Temperature dependence of the phonon lifetime for $\xi = 0.35$ r.l.u. Solid lines are guide for the eye and dashed lines depict the critical temperatures of Ni_2MnGa.*

The phonon peak widths of Ni_2MnGa have been calculated from the measured soft $TA_2[\xi\xi0]$ phonons. The FWHM values of the phonon peak has been achieved by the deconvolution of the measured points with the instrumental resolution of PUMA [Eck07]. For this calculations $\xi = 0.35$ r.l.u. has been used. After the deconvolution of the resolution ellipsoid, FWHMs of the phonon have been calculated from a damped harmonic oscillator fit to the data. FWHM results of these fits are shown as a function of temperature in Figure 7.12. The critical temperatures of Ni_2MnGa are shown as dashed lines in the graph. Measurements show that the phonon lifetime around the softening is increasing when the ferromagnetic ordering is achieved. This indicates strongly the effect of magnetic properties on the vibrational properties of the soft mode in the stoichiometric composition. The results which are shown in Figure 7.11 and Figure 7.12 confirm the effect of magnetism on the soft mode of the TA_2 phonon in the stoichiometric composition.

7.4 Vibrational Properties of Martensite Phases

The vibrational properties in martensite phases are important to understand the nature of the magnetic field induced shape memory effect. As explained in Chapter 2.3.1, magnetic shape memory effect can be observed in two different ways. Phonon properties in the austenite phase are important to understand the magnetic field induced structural transition. However, to understand the nature of the magnetic field induced variant reorientation in the martensite phase, austenite phase phonons are not suitable. To overcome the lack of knowledge in the vibrational properties of the martensite phase, we investigate the phonon dispersion of two existing martensite phases of Ni-Mn-Ga alloys. Full phonon dispersion of the five-layer modulated martensite phase has been measured for the high symmetry directions of the martensite phase. Additional to this, the $[\xi\xi0]$ and $[0\xi\xi]$ measurements of the non-modulated martensite have been done.

7.4.1 Vibrational Properties of $Ni_{50}Mn_{29}Ga_{21}$ in 5M Martensite Phase

To understand the nature of the magnetic filed induced variant reorientation, it is essential to investigate the vibrational properties of one of the possible martensite phase. In this work, we were able to measure the phonon dispersion of the offstoichiometric five-layer modulated martensite phase. The phonon dispersion of this 5M martensite was shown in Figure 6.10 in Chapter 6.2.1. Up to now, these measurements are the only existing experimental literature for the vibrational properties of the 5M martensite phase. The full phonon dispersion calculations of real five-layered modulated martensite phase need too much time for calculations, in the order of months [GE09]. Entel *et al.* were able to calculate the $[\xi\xi0]$ high symmetry direction of the stoichiometric composition within a oversimplified way. For the simplification, calculations have been done in a tetragonal structure in which the modulation is assumed as a small perturbation of the structure [EBG$^+$08]. Comparison of these oversimplified model calculations with the room temperature measurements of $Ni_{50}Mn_{29}Ga_{21}$ is shown in Figure 7.13. Solid lines indicate the first-principles calculation results of 5M tetragonal martensite and symbols show the measurement results. Similar to the previous representations, solid symbols correspond to second-transverse (T_2) mode, open and crossed symbols represent longitudinal (L) and

Table 7.7: Comparison of the calculated sound velocities of off-stoichiometric $L2_1$ austenite and 5M martensite phases.

	Austenite (10^5 cm s^{-1})	5M Martensite (10^5 cm s^{-1})
ν_{LA}	8.15 ± 0.24	7.92 ± 0.32
ν_{TA_1}	4.92 ± 0.15	4.55 ± 0.14
ν_{TA_2}	1.63 ± 0.10	1.78 ± 0.07

first-transverse (T_1) modes. The star symbols, which are shown in the low frequency transfer part of the figure, correspond to the observed peak maxima of the low frequency excitations.

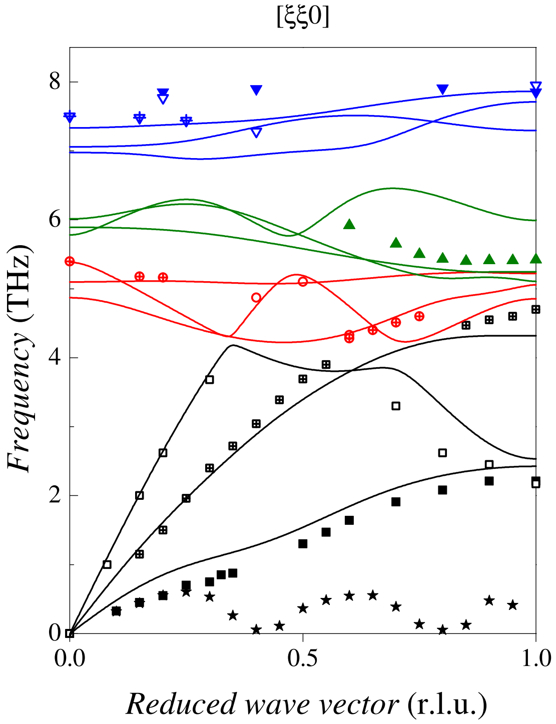

Figure 7.13: *Comparison of first principle calculations and the phonon measurements of [ξξ0] direction of Ni-Mn-Ga. Symbols correspond to the measurement results of $Ni_{50}Mn_{29}Ga_{21}$ sample and lines show the first principle calculations of stoichiometric composition from [EBG+ 08].*

The comparison of experimental data with the simplified theoretical predictions shows that, the agreement between them is qualitatively good. In the acoustic modes for the high ξ region, the theory predicts higher frequencies than the observed ones. Because the 5M modulation is not included in the theoretical model, the low energy excitations are absent from the calculations. Also one has to take into account that, the first-principles calculations of the 5M martensite have been made for the stoichiometric composition.

Despite all of these differences, the measurements confirm that, this oversimplified model is acceptable for modeling the $[\xi\xi 0]$ phonon dispersion of five-layer modulated martensite phase. In overall, the phonon of the 5M lies in the same frequency region of the austenite phase. Similar to the austenite phase optical modes show very limited dispersion. Another similarity has been observed at the sound velocities of the $[\xi\xi 0]$ direction. Figure 7.14 and Table 7.7 compare the initial slopes of the acoustic modes for 5M martensite with those of the austenite ($L2_1$) phase. They are all very much the same. With the exception of the softening of the $TA_2[\xi\xi 0]$ branch around ξ=0.2-0.4 r.l.u. the vibrational properties of the martensite and austenite resemble very much.

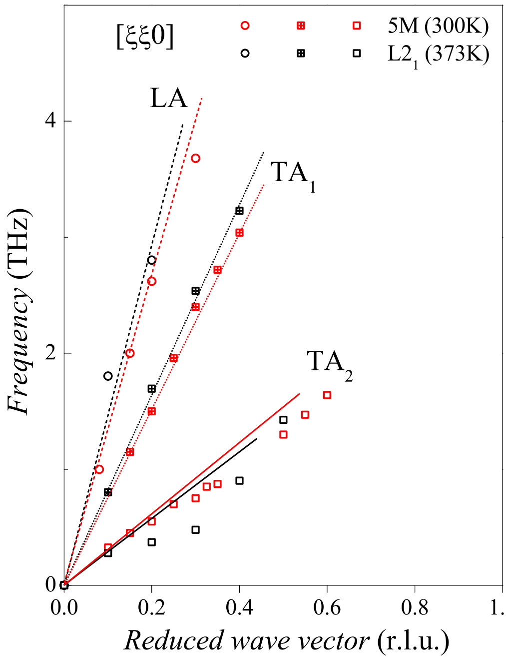

Figure 7.14: *Transversal and longitudinal $[\xi\xi 0]$ phonon branches of austenite and five-layer modulated martensite phases. Symbols in black represent the measurement results of $Ni_{49}Mn_{32}Ga_{19}$ in austenite phase and red symbols correspond the martensite phase of $Ni_{50}Mn_{29}Ga_{21}$. Circles indicate longitudinal polarization, crossed and open squares represent first (TA_1) and second (TA_2) transversal polarizations, respectively. Lines correspond to sound velocities in Table 7.7*

7.4.2 Vibrational Properties of $Ni_{50}Mn_{30}Ga_{20}$ in NM Martensite Phase

The non-modulated tetragonal structure is predicted to be the stable low temperature martensite phase of Ni_2MnGa in different theoretical calculations [AEN02, UHN$^+$09, SGD$^+$11, EGH$^+$12]. Also some of the offstoichiometric compositions of Ni-Mn-Ga alloys show non-modulated tetragonal structure in the martensite phase with c/a ratio higher than 1. As an example, the offstoichiometric $Ni_{50}Mn_{30}Ga_{20}$ sample shows non-modulated martensite phase at room temperature with the c/a ratio of 1.21 which qualitatively agrees with [PCSC00, EHAN03]. Small differences in the observed c/a ratios between literature and present study are related to the compositional differences. Due to the high symmetry of the non-modulated tetragonal phase (compared to modulated martensite phases), it is possible to calculate the phonon dispersion of the stoichiometric Ni_2MnGa by using the first-principles. The measurements for $Ni_{50}Mn_{30}Ga_{20}$ are shown in Figure 7.15 in comparison with theoretical calculations of non-modulated tetragonal phase of Ni_2MnGa by Siewert *et al.* [SGE12a].

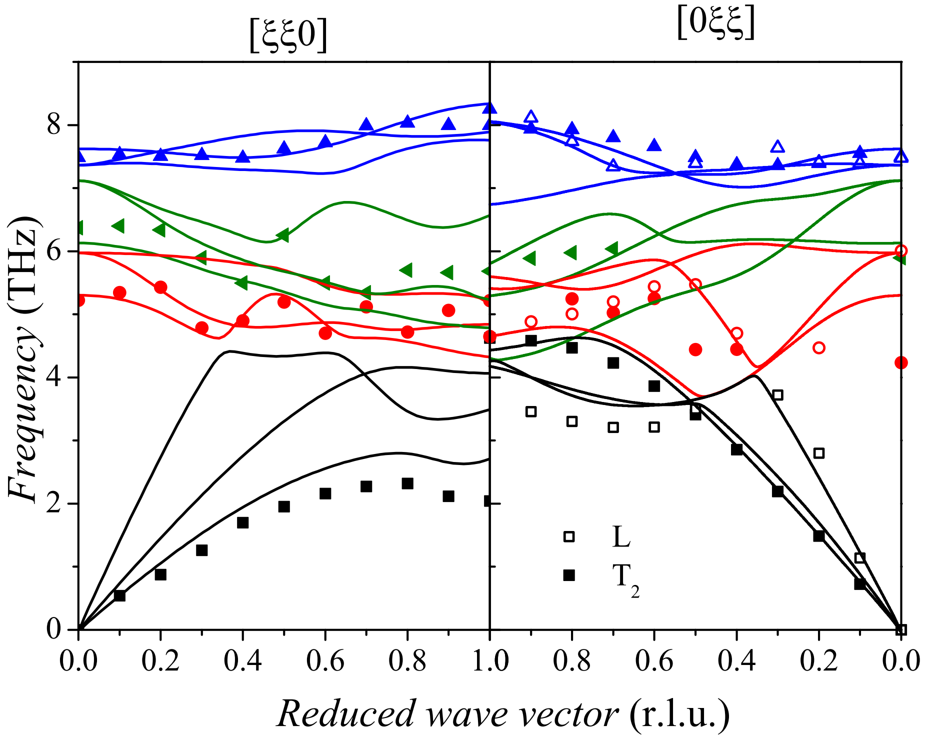

Figure 7.15: *Phonon dispersion of the non-modulated martensite of $Ni_{50}Mn_{30}Ga_{20}$ at room temperature in [ξξ0] and [0ξξ] directions as shown in Figure 6.11. Full and open symbols indicate transversal(T_2) and longitudinal(L) phonon measurements, respectively. Solid lines are the first-principles calculations of Ni_2MnGa and were taken from [SGE12a].*

The phonon measurements of offstoichiometric $Ni_{50}Mn_{30}Ga_{20}$ agrees qualitatively with the theoretical calculations of stoichiometric non-modulated tetragonal phase. Both theoretical calculations and experimental results show a gap at the zone boundaries of acoustic [ξξ0] and [0ξξ] modes. The main difference is clearly observed at the T_2-mode of these high symmetry directions. This kind of difference is expected from the crystallographic anisotropy of the non-modulated tetragonal phase. Although the chemical composition of the measured system differs from the calculated one, qualitative agreement in the acoustic modes and the high frequency optical modes are surprisingly good.

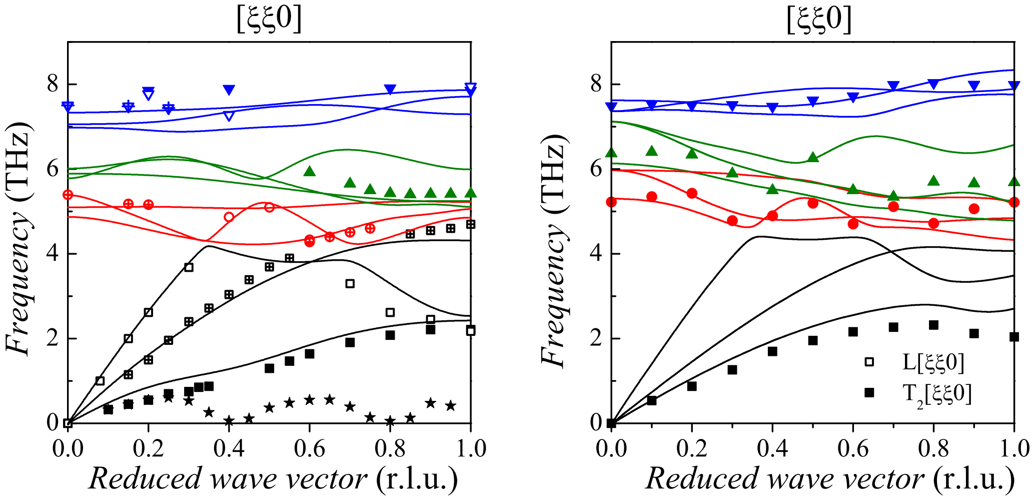

Figure 7.16: *Comparison of the [ξξ0] direction phonon dispersion of (a) 5M martensite and (b) NM martensite phases. Solid lines are first-principles calculations of corresponding phases of* Ni_2MnGa.

The comparison of the [ξξ0] directions of 5M and NM marteniste phases are shown in Figure 7.16. In the case of 5M marteniste phase, a weak softening is observed at $TA_2[\xi\xi0]$ phonon mode in a particular region of the reciprocal space ($0.2 < \xi < 0.5$ r.l.u.). In the NM martensite phase $TA_2[\xi\xi0]$ phonon mode shows no strong softening feature at aforementioned region. In this particular region, the TA_2-mode of the NM martensite shows higher frequencies compared to austenite and modulated martensite phases. In 5M martensite phase optical modes are well split into three different groups. In the NM martensite phase, specially in the mid frequency (first and second optical modes) region, optical modes are more entangled. It has been shown that in the austenite phase measurements, in each of these optical groups, one kind of atom is dominating the vibration. It might be interesting to see if that is also the case in the martensite phases. To make this calculation possible in the NM martenite, it is essential to measure all high symmetry directions of the phase.

7.4.3 Low Frequency Excitations of Pre-martensite and Martensite Phases

Low frequency measurements of the Ni_2MnGa have been carried out at 230 K which corresponds to the temperature of premartensite phase of the stoichiometric composition. The measurements showed that the softening which is a feature of the austenite phase still keeps its existence in premartensite phase. Additional to this, an inelastic intensity between soft $TA_2[\xi\xi 0]$ mode and superstructure peak is observed. Similar feature has been observed by Shapiro *et al.* in Ni_2MnGa at 200 K [SVH$^+$07]. The work of Shapiro *et al.* shows a incommensurate superstructure peak at ξ=0.43 r.l.u. without any repetition in the Brillouin zone. Our temperature dependent elastic measurements confirm the existence of the ξ=0.43 peak at low temperatures -see Figure 7.18. The temperature dependent elastic measurements of Ni_2MnGa confirm the premartensite transition around 270 K. Here the premartensite phase indicates itself as the peak at a commensurate position (ξ=0.33 r.l.u.). At low temperatures, an incommensurate peak (ξ=0.43 r.l.u.) replaces the commensurate peak. The commensurate and incommensurate peaks at 220 K are shown in Figure 7.18b. The evaluation of these peaks are shown in Figure 7.18b as inset. Here ξ=0.33 r.l.u. corresponds to the intensities of superstructure Bragg peak of premartensite phase. It is clear that, this peak does not exist at high temperatures in the austenite phase. After the premartensite transformation, the peak intensity increases and saturates around the martensite transition temperature. When the martensite transformation temperature is approached the intensity of premartensite peak decreases (ξ=0.33 r.l.u.) and the intensity of incommensurate peak increases (ξ=0.43 r.l.u.). The behavior of the incommensurate martensite peak agrees well with the investigation of Shapiro *et al.*. Additionally to these two peaks, another peak like behavior is observed at around ξ=0.12 r.l.u. The intensity of this peak increases monotonously in the premartensite and martensite phases in the measured temperature interval. A similar increase in intensity around ξ=0.17 r.l.u. is observed in Ni_2MnGa by Stuhr *et al.* [SVKL97]. The real nature of the peak is still unknown.

The overall behavior in the low frequency regions of martensite and premartensite looks similar but has some minor differences. In the case of martensite (Figure 7.17), the observed softening is less pronounced as expected by the nature of the structural transition and the superstructure peak is observed at incommensurate position of ξ=0.43 r.l.u. In the premartensite case (Figure 6.14) softening is more pronounced and the superstructure peak is observed at commensurate position of ξ=0.33 r.l.u. In both cases, superstructure peaks are not repeated for higher orders and additional intensities are observed around these superstructure peaks. In the work of Shapiro *et al.*, observed additional intensi-

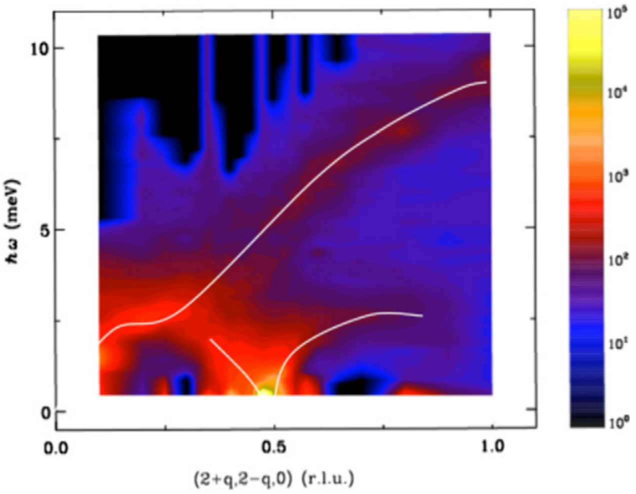

Figure 7.17: *Contour plot of the low energy region of Ni_2MnGa at 200 K. Color bar represents logarithmic neutron intensity and white lines are guide for the eye. Image is taken from [SVH$^+$07].*

ties around the superstructure peak have been attributed to charge density waves due to different sound velocities of these excitations compared to the transverse acoustic mode [SVH$^+$07].

Similar low frequency measurements in five-layer modulated martensite of $Ni_{50}Mn_{29}Ga_{21}$ were done and shown in Figure 6.13. Different from stoichiometric composition in five-layer modulated martensite phase, superstructure Bragg peaks repeat itself in the whole Brillouin zone at the commensurate positions of $\xi = 0.4$ and 0.8 r.l.u. Additionally, another difference in the low frequency transfer is observed in the slopes of the acoustic-like intensities which are around the superstructure peaks. As indicated before, in stoichiometric system, the slope of the low frequency excitations which are related with the incommensurate superstructure peak differs from the slope of $TA_2[\xi\xi0]$ [SVH$^+$07]. In the case of 5M martensite, low frequency excitations have similar slopes compared to $TA_2[\xi\xi0]$ phonon mode. The sound velocity calculations show similar values for TA_2-mode (1.78×10^5 cm/s) of the martensite phase and the low frequency excitations (1.70×10^5 cm/s).

7.5 Effect of Mechanical Training on the Martensites

To observe an efficient ferromagnetic shape memory effect, it is important to create single variant state in the martensite phase. In our investigations, as shown in Chapter 5.1.4.1, measured martensite samples were mechanically trained beforehand. In the present work, two different martensite single crystals have been mechanically trained (non-modulated and five-layer modulated martensite samples). The effect of training is strongly observed on non-modulated sample. The multiple variant state (five variants) have been observed

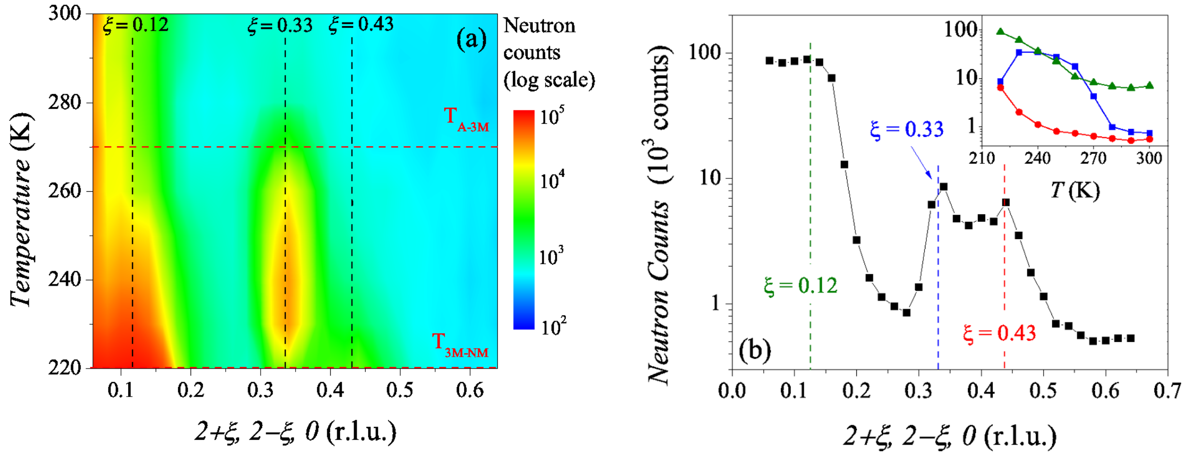

Figure 7.18: *(a) Contour plot representation of elastic measurements for stoichiometric* Ni_2MnGa *as a function of temperature. Color bar represents neutron intensity in logarithmic scale, red dashed lines indicate critical transition temperatures of* Ni_2MnGa*. (b) Elastic intensity plot at 220 K along [2+ξ 2-ξ 0] direction. Inset figure shows the intensity profiles of colored dashed lines as a function of temperature.*

in the initial measurements of the non-modulated martensite sample (Figure 5.11a). After mechanical training, these variants disappeared and the crystal transformed to a single variant state (Figure 5.11b).

The effect of training on the shape recovery properties of Ni-Mn-Ga alloys is investigated in literature by means of different methods. The studies of Chmielus *et al.* and Rolfs *et al.* show that mechanical training is necessary to observe low twinning stresses for the shape memory alloys [CRW$^+$10, RCG$^+$12]. In addition to the training, surface treatment also plays an important role on stress recovery properties. It is shown in [RCG$^+$12] that the training may cause reorientation of the defects in the single crystals which creates cracks on the sample and destroys the shape memory effect. Our investigations show that this holds true only for the modulated martensite phase. In the case of non-modulated martensite, mechanical training did not show any destructive effect on the single crystal.

Figure 7.19 shows optical microscopy images of the five-layer modulated martensite sample. In Figure 7.19a the surface of the five-layered martensite sample with 10x magnification is shown. Here the domain structure of the martensite phase is clearly visible as bright and dark regions on the surface. Figure 7.19b-c show the similar surface after multiple mechanical training cycles again with magnification of 10x. It is clear that, after mechanical training, cracks occur on the surface of the sample and this holds true for each surface. The zoomed in image of a crack is shown in Figure 7.19d. The zig-zag structure of the crack is perfectly visible in the image. The training is essential for creating single variant samples but when a surface defect occurs on the sample, the mechanical training is not suitable anymore due to the inhomogeneous load distribution along the sample. This inhomogeneous distribution improves the crack network and destroys the mechanical training process. Similar cracked structures have been observed by Xiong *et al.* in offstoichiometric Mn-rich Ni-Mn-Ga just by applying thermal cycling [XLP05]. In that work, it is concluded that the zig-zag like crack structure occurs due to the existence of several modulated martensite phases and penetrates within the twin boundaries. In addition to our observations, similar multiple twin structure has been observed for different modulated martensitic phases of offstoichiometric Ni-Mn-Ga alloys [SLL+10, CSO+10, DBR+11, KNT+11]. These studies mainly conclude that, the modulated structure does not only consist of macroscopic domain structures but also microscopic domain structures are embedded in. In our optical microscopy investigations only the macroscopic domains were visible as different shades.

7.6 Relation of Entropy with the Phase Stability

The lattice entropies of the austenite phases were calculated and shown in Chapter 7.2 for stoichiometric and offstoichiometric compositions. In addition to these entropy calculations which were shown in above mentioned chapters, the transition entropy changes of different Ni-Mn-Ga have been calculated by means of calorimetric measurements. The calculated total entropy change of the transition from a calorimetric measurement, $\Delta\mathrm{S}_{transition}$, can be formulated as in the following;

$$\Delta S_{transition} \approx \frac{\Delta Q_{transition}}{T} \tag{7.2}$$

where , ΔQ is the heat change at the transformation, and T is the transformation temperature. It is possible to calculate the transformation heat, directly from the calorimetric measurements which were carried out for the polycrystalline samples. For the determination of the structural transformation temperature peak maxima and minima of the calorimetric measurements were used. Table 7.8 shows that at the structural transition temperatures the entropy of the system changes slightly as a function of chemical composition.

The enthalpy change at the transition temperature was calculated by taking the absolute averages of the heat exchange values $\Delta Q_{heating}$ and $\Delta Q_{cooling}$. When the Gibbs free energies of martensite and austenite are equal then the total entropy changes can be calculated

Table 7.8: Observed heat transfer values during heating ($\Delta Q_{heating}$) and cooling ($\Delta Q_{cooling}$) cycles, enthalpy change (ΔH), total entropy change (ΔS) values and transition temperatures of different $Ni_{50+x}Mn_{25-x}Ga_{25}$ alloys.

Alloy	$\Delta Q_{heating}$ J g^{-1}	$\Delta Q_{cooling}$ J g^{-1}	ΔH J g^{-1}	ΔS k_B	$T_{transition}$ K
$Ni_{52.5}Mn_{22.5}Ga_{25}$	7.67	-7.59	7.63	0.186	293.9
$Ni_{55}Mn_{20}Ga_{25}$	6.50	-6.92	6.71	0.107	439.4
$Ni_{57.5}Mn_{17.5}Ga_{25}$	6.75	-6.96	6.86	0.091	530.7

from Equation 7.2. These calculated values of ΔS agree with the work of Khovailo *et al.* [KOAT03]. The enthalpy and entropy changes of stoichiometric sample can not be calculated due to the sluggish nature of the premartensite transition.

The study of Enkovaara *et al.* claims that, from the first-principles calculations, cubic to tetragonal transition in stoichiometric Ni_2MnGa is driven by the vibrational free energy [EHAN03]. The main reason for this conclusion relies on the extrapolation of the free energy within the Debye approximation. The only argument stating that the structural phase transition is driven by the phonon is the rough coincidence of the calculated and experimental phase transition temperatures. As the first-principles calculations can not directly determine the entropy differences at finite temperatures experimental findings are more reliable at these temperatures. For clarifying the hypothesis of Enkovaara *et al.*, vibrational entropies of the stoichiometric Ni_2MnGa in the austenite phase have been calculated directly from the vibrational density of states - see Figure 7.3 and 7.7. The calculated lattice entropies for quasi-harmonic model do not deviate quantitatively from the harmonic model at transition temperatures. This holds true for both stoichiometric and offstoichiometric compositions. The temperature dependence of the phonon frequency squared of both compositions (see Figure 6.17) shows similar behavior around the structural transition temperature. Besides the structural changes, the phonon frequencies are identical at the structural transition. As there is no significant jump in the phonon frequencies of the $TA_2[\xi\xi0]$ soft phonon mode, it is possible to conclude that the lattice entropy has no significant effect on the total entropy change at the structural transition.

Besides these observations, magnetization measurements of stoichiometric and offstoichiometric (see Figure 5.3 and Figure 5.6) compositions show significant changes in magnetization around the structural transition temperatures. Therefore for both compositions, magnetic contribution to the total energies may play a role in the phase stabilization. Since there is no clear experimental evidence that the vibrational entropy is dominating the austenite phase stabilization, changes in magnetic (or electronic) entropy may play a significant role in the phase stabilizations.

Recent positron annihilation study of Haynes *et al.* [HWL$^+$12] and theoretical calculations [LRH02, GAZ$^+$08, UHN$^+$09] show that Fermi surface nesting plays an important role on the vibrational properties of the $TA_2[\xi\xi0]$ phonon branch. As this branch is the anomalous phonon branch which mainly drives the structural transition, it is possible to conclude that the Fermi surface nesting plays an important role on phase stabilization. In these studies, the softening which is observed in stoichiometric Ni_2MnGa sample is strongly correlated to the Fermi surface nesting or electron-phonon coupling. Our investigations show that, in the austenite phase for the stoichiometric composition, the phonon lifetime increases in the ferromagnetic region, which indicates the strong interaction between the phonon softening and the magnetic properties of the sample. All of these observation proves that the lattice vibrations alone is not enough to stabilize the phase or drive the structural transitions.

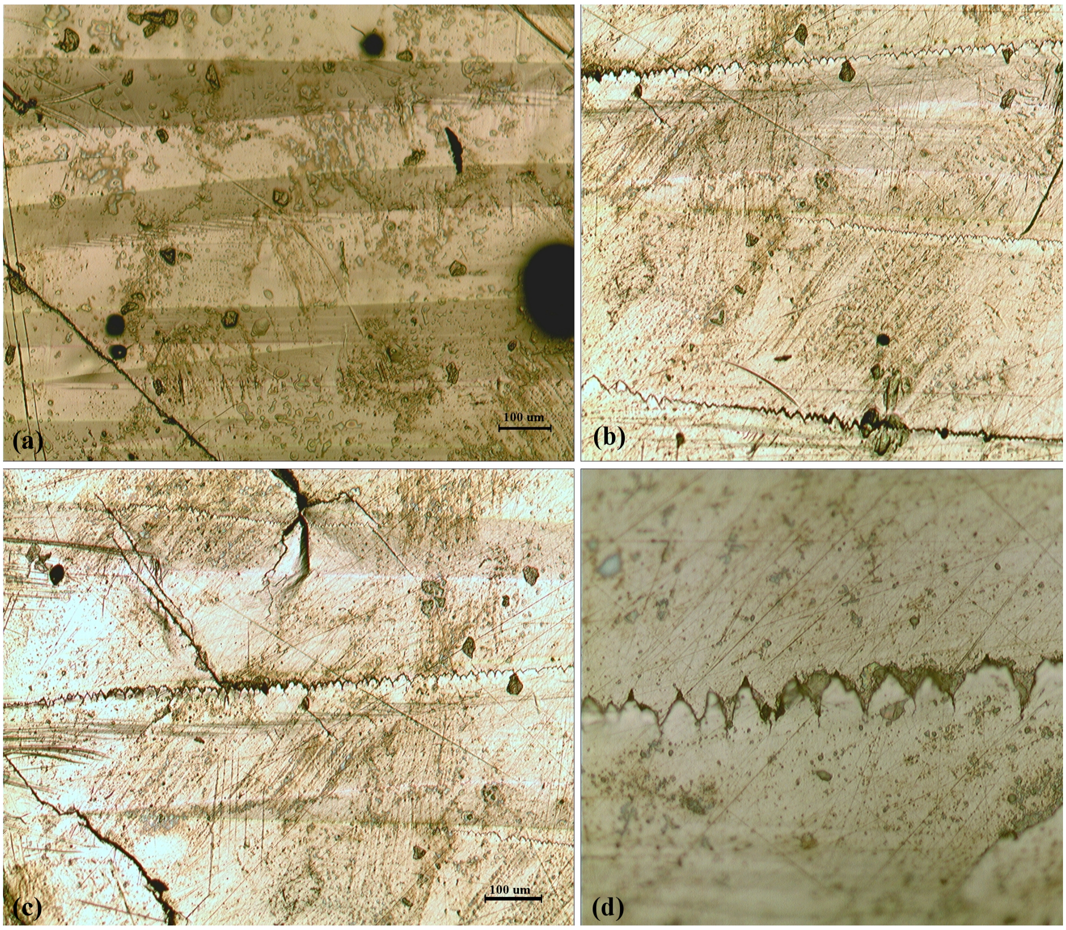

Figure 7.19: *Optical microscopy images of the surface characteristics of five-layer modulateded martensite* $Ni_{50}Mn_{29}Ga_{21}$*. (a) shows the macroscopic domain structure of the five-layered modulated martensite. Here, bright and dark regions correspond to different orientations of the domains. (b)-(c) shows the surface defects (cracks) which become much pronounced after mechanical training. (d) shows the magnified image of the crack structure.*

Chapter 8

Summary and Outlook

In this study, large single single crystals of austenite and martensite phases, which are suitable for phonon measurements, have been used. These high quality single crystals have been produced by Dr. K. Rolfs by using a special crystal growth technique (SLARE). This technique helps to reduce the chemical compositional gradient in the sample and improves the purity of the single crystals. By using these single crystals, in the austenite phase, complete phonon dispersions of the stoichiometric and offstoichiometric alloys have been measured for the first time. Depending upon these complete phonon dispersion measurements, thermodynamic properties of stoichiometric and offstoichiometric alloys have been calculated for the first time from the phonon dispersions. The effect of compositional changes on the phonon dispersion of the austenite phase has been investigated. The phonon dispersion measurements of martensite phases have been carried out on Ni-Mn-Ga samples for the first time. A complete phonon dispersion of the five-layer modulated (5M) martensite phase has been measured on $Ni_{50}Mn_{29}Ga_{21}$ sample at room temperature. A very good agreement has been achieved between the $[\xi\xi0]$ direction phonon measurements and first-principles calculations of the 5M martensite. The same also holds true in non-modulated martensite phase measurements.

Temperature dependence of the soft phonon mode of $TA_2[\xi\xi0]$ has been investigated for stoichiometric and offstoichiometric compositions around the structural and magnetic transition temperatures. From these investigations, transformation mechanisms of austenite-to-premartensite and austenite-to-martensite phase have been revealed. The relation between the magnetic ordering and the vibrational properties has been investigated by means of the comparison of temperature dependent magnetization and phonon measurements. Temperature dependent phonon investigations revealed that, phonon measurements alone are not enough to clarify the relation between the structural and magnetic properties.

Phonon Softening

Softening which is observed at $TA_2[\xi\xi0]$ phonon branches of stoichiometric and offstoichiometric compositions gives a clue about the transformation path of the martensite transition. In the case of stoichiometric composition, softening minimum is at ξ=0.33 r.l.u. perfectly agrees with the susceptibility calculations [LRH02]. The observed softening for Ni_2MnGa is more pronounced compared to $Ni_{49}Mn_{32}Ga_{19}$ which has a minimum around ξ=0.27 r.l.u. The compositional disorder in the offstoichiometric sample leads to a smearing of the phonon anomaly in the q-space and this smearing out is observable in the elastic constant calculations of the $TA_2[\xi\xi0]$ phonon mode. Temperature dependence of the C' elastic constant shows that, in the stoichiometric composition, temperature has no significant effect in the austenite phase. Similar feature has been observed in the ultrasonic measurements of Manosa *et al.* [MGCO$^+$97]. These results indicate that, at the austenite-to-premartensite structural transition shear is not playing a role but shuffle is. The temperature dependent elastic constants of offstoichiometric sample shows a slight temperature dependence at C' elastic constant which indicates, that the shear is playing a role in the austenite-to-martensite structural transition.

Temperature Dependence of $TA_2[\frac{1}{3}\frac{1}{3}0]$

Temperature dependence of the softening at the $TA_2[\xi\xi0]$ phonon branch around the softening minimum has similar behavior both for stoichiometric and offstoichiometric compositions. The square of the phonon frequencies gets soft without reaching to zero while approaching the structural transition from both phases. The temperature dependent feature is described by generalized Landau expansion. In the case of stoichiometric sample, the observed slope changes coincide perfectly with structural and magnetic transition temperatures. Additionally, line width investigations of the stoichiometric sample indicates a broadening in the ferromagnetic region which shows the effect of ferromagnetism on the vibrational properties. Due to these reasons, it is possible to comment that for the stoichiometric composition the Landau expansion reflects both structural and magnetic ordering phenomena. In case of the offstoichiometric composition, the temperature behavior of the phonon softening reflects the structural transition, however, no obvious influence of the magnetic transition to the phonon softening is observed. It is shown that the offstoichiometric composition has much complicated magnetic structure compared to the stoichiometric case. Due to this complex magnetic structure of the offstoichiometric composition, the relation between magnetic ordering and the lattice vibrations is still an open question.

Vibrational Entropies

Martensite phases of offstoichiometric Ni-Mn-Ga alloys were measured in non-modulated (NM) and five-layer modulated (5M) martensites. Measurements were compared with theoretical calculations existing in the literature. The agreement between the literature and the measurements is qualitatively good. The main difference between the literature and the measurements is based on the compositional and temperature differences. In both martensite phases, frequency differences at the zone boundaries in the acoustic modes which are expected from the first-principles calculations are confirmed by our measurements. Additionally, the observed acoustic modes in the offstoichiometric 5M martensite do not differ so much from the acoustic modes of the offstoichiometric austenite sample. Low frequency excitations are observed in 5M sample. These acoustic-like intensities are strongly correlated with the commensurate superstructure Bragg peaks of the modulated phase. The slope of these acoustic-like intensities are similar to the slope of the $TA_2[\xi\xi 0]$ phonon branch. In stoichiometric sample, similar low frequency excitations are observed in the premartensite phase. For the stoichiometric composition observed low frequency excitations in the incommensurate martensite phase are attributed to the phason excitations associated with the charge density waves [SVH$^+$07]. This might hold true for stoichiometric composition but definitely not the case for the offstoichiometric one. Putting together the puzzles of present study with these of [SVH$^+$07] phason manifest in stoichiometric martensite at an incommensurate position, in modulated martensite, the corresponding low lying excitations can be fully understood in terms of acoustic phonons of the respective layered structure. This brings the question of existence of charge density waves in offstoichiometric compositions.

Different Entropy Contributions to Phase Diagram

The effect of vibrational entropy on the phase stabilization of the austenite phase was investigated. The results show that only the lattice entropy is not enough to drive the structural transition and also not enough for the stabilization of the austenite phase. Recent first-principles calculations and the positron annihilation study reveal a strong relation between the Fermi surface nesting and the vibrational properties. Very fundamentally, temperature dependent magnetization measurements show significant changes at the structural transitions. Since the magnetic properties of austenite and martensite phases differs significantly, the magnetic contribution to the total energy may play a role in the structural transition and the phase stabilization. The magnetization measurements of stoichiometric Ni_2MnGa show that, around the premartensite and martensite transitions, the entropy change is not only due to changes in lattice entropy but a mixture of all lattice, magnetic and electronic entropies. The stoichiometric Ni_2MnGa is ferromagnetic in the temperature interval of 200 K $\leq$ T $\leq$ 300 K and the calculated entropy changes in this temperature range show a positive entropy change as a function of the applied magnetic field. With the application of an external magnetic field to a ferromagnet, it is expected to observe a decrease in the magnetic entropy. This observed anomalous behavior indicates that not only magnetic entropy but all magnetic, structural and electronic entropies play a role at the premartensite and martensite transitions in Ni_2MnGa.

Crystallographic Structures and Flattening of Phonon Dispersion

The crystallographic structures of offstoichiometric Ni-Mn-Ga alloys were investigated in both austenite and martensite phases. The obtained results agree with the literature. For the austenite phase, the $L2_1$ structure with the space group of $Fm\bar{3}m$ was observed. Rietved refinement, in the offstoichiometric composition, shows that the excess manganese atoms occupy the manganese and gallium sites only. Due to this, the atomic interactions in the offstoichiometric composition differ from those of the stoichiometric composition. This difference brings about an increased variation in force constants between atoms which causes a flattening of the phonon dispersion in the optical modes. The same occupancy condition holds true for the martensite phase of the five-layer modulated (5M) sample and due to this, the optical modes of 5M are also relatively flat. The martensite phase refinement results show that, the exact structure of the martensite has a monoclinic structure (space group of I2/m) with a commensurate modulation vector of ξ=0.4 r.l.u.

Effect of Training

The effects of mechanical training on the martensite phases were investigated. The mechanical training works perfectly for creating a single variant state of non-modulated martensite. Unfortunately, this was not the case for five-layer modulated martensite phase. It was observed that, the cyclic mechanical training generates surface defects on the investigated five-layer modulated martensite crystals. These defects inhibit the effect of training and damage the single crystal.

Outlook

To better understand the nature of the ferromagnetic shape memory effect, it is necessary to have a theoretical explanation for the relation between the magnetic and vibrational properties at finite temperatures. A measurement of the magnon dispersion of stoichiometric and offstoichiometric sample may help to understand the effect of magnetism on vibrational modes. The magnon measurements can be carried out on the Neutron Resonance Spinecho Triple Axis Spectrometer (TRISP) which is located at at Forschungs-

Neutronenquelle Heinz-Maier Leibnitz (FRM II). Investigating the vibrational properties of Ni_2Mn-X (X = In and Sb) alloys might allow comparison with Heusler alloys of different magnetic properties. Temperature dependent magnetization investigations of these materials reveal two different magnetic ordering temperatures. It might be interesting to see if the Fermi surface nesting and phonon softening are taking role in the transition properties of these magnetic materials, too. Additionally, direct measurements of the electronic properties as a function of composition and temperature may support more information about the nature of the structural transition.

Bibliography

[AAD$^+$09] S. Aksoy, M. Acet, P. P. Deen, L. Mañosa, and A. Planes. Magnetic correlations in martensitic Ni-Mn-based Heusler shape-memory alloys: Neutron polarization analysis. *Phys. Rev. B*, 79:212401, Jun 2009.

[AAK$^+$12] S. Aksoy, M. Acet, T. Krenke, E. F. Wassermann, M. Gruner, P. Entel, L. Mañosa, A. Planes, and P. P. Deen. Magnetic Interactions Governing the Inverse Magnetocaloric Effect in Martensitic NiMn-Based Shape-memory Alloys. In Tomoyuki Kakeshita, Takashi Fukuda, Avadh Saxena, and Antoni Planes, editors, *Disorder and Strain-Induced Complexity in Functional Materials*, volume 148 of *Springer Series in Materials Science*, pages 67–77. Springer Berlin Heidelberg, 2012.

[AEN02] A. Ayuela, J. Enkovaara, and R. M. Nieminen. Ab initio study of tetragonal variants in Ni_2MnGa alloy. *Journal of Physics: Condensed Matter*, 14(21):5325, 2002.

[AMP11] M. Acet, L. Mañosa, and A. Planes. Chapter Four - Magnetic-Field-Induced Effects in Martensitic Heusler-Based Magnetic Shape Memory Alloys. In K.H.J. Buschow, editor, *Handbook of Magnetic Materials*, volume 19 of *Handbook of Magnetic Materials*, pages 231–289. Elsevier, 2011.

[BRC03] Claudia Bungaro, K. M. Rabe, and A. Dal Corso. First-principles study of lattice instabilities in ferromagnetic Ni_2MnGa. *Phys. Rev. B*, 68:134104, Oct 2003.

[Bro66] B. N. Brockhouse. *Phonons in Perfect Lattices and in Lattices with Point Imperfections*. Oliver and Boyd, 1966. Chapter: Neutron Scattering by Phonons.

[CGH$^+$11] Markus Chmielus, Illya Glavatskyy, Jens-Uwe Hoffmann, Volodymyr A. Chernenko, Rainer Schneider, and Peter Müllner. Influence of constraints and twinning stress on magnetic field-induced strain of magnetic shape-memory alloys. *Scripta Materialia*, 64(9):888–891, 2011.

[CPS03] T. Castán, A. Planes, and A. Saxena. Modulated phases in multi-stage structural transformations. *Phys. Rev. B*, 67:134113, Apr 2003.

[CPSC02] V.A. Chernenko, J. Pons, C. Seguí, and E. Cesari. Premartensitic phenomena and other phase transformations in NiMnGa alloys studied by dynamical mechanical analysis and electron diffraction. *Acta Materialia*, 50(1):53–60, 2002.

[CRW$^+$10] M. Chmielus, K. Rolfs, R. Wimpory, W. Reimers, P. Müllner, and R. Schneider. Effects of surface roughness and training on the twinning stress of NiMnGa single crystals. *Acta Materialia*, 58(11):3952–3962, 2010.

[CSO$^+$10] R. Chulist, W. Skrotzki, C.-G. Oertel, A. Böhm, T. Lippmann, and E. Rybacki. Microstructure and texture in $Ni_{50}Mn_{29}Ga_{21}$ deformed by high-pressure torsion. *Scripta Materialia*, 62(9):650–653, 2010.

[DBR$^+$11] Anett Diestel, Anja Backen, Ulrich K. Rossler, Ludwig Schultz, and Sebastian Fahler. Twin boundary energy of hierarchically twinned magnetic shape memory alloys. *Applied Physics Letters*, 99(9):092512, 2011.

[DTLP03] C. Degueldre, P. Tissot, H. Lartigue, and M. Pouchon. Specific heat capacity and Debye temperature of zirconia and its solid solution. *Thermochimica Acta*, 403(2):267–273, 2003.

[EBG$^+$08] Peter Entel, Vasiliy D. Buchelnikov, Markus E. Gruner, Alfred Hucht, Vladimir V. Khovailo, Sanjeev K. Nayak, and Alexey T. Zayak. Shape Memory Alloys: A Summary of Recent Achievements. *Materials Science Forum*, 583:21–41, 2008.

[EBK$^+$06] P. Entel, V. D. Buchelnikov, V. V. Khovailo, A. T. Zayak, W. A. Adeagbo, M. E. Gruner, H. C. Herper, and E. F. Wassermann. Modelling the phase diagram of magnetic shape memory Heusler alloys. *Journal of Physics D: Applied Physics*, 39(5):865, 2006.

[Eck07] G. Eckold. *Fit PUMA3 Code.* Georg-August-Universität Göttingen, July 2007.

[EGH$^+$12] P. Entel, M. E. Gruner, A. Hucht, A. Dannenberg, M. Siewert, H. C. Herper, T. Takeshita, T. Fukuda, V. V. Sokolovskiy, and V. D. Buchelnikov.

Phase Diagrams of Conventional and Inverse Functional Magnetic Heusler Alloys: New Theoretical and Experimental Investigations. In T. Kakeshita, T. Fukuda, A. Saxena, and A. Planes, editors, *Disorder and Strain-Induced Complexity in Functional Materials*, volume 148 of *Springer Series in Material Science*, chapter 2. Springer, 2012.

[EHAN03] J. Enkovaara, O. Heczko, A. Ayuela, and R. M. Nieminen. Coexistence of ferromagnetic and antiferromagnetic order in Mn-doped Ni_2MnGa. *Phys. Rev. B*, 67:212405, Jun 2003.

[ESG+12] Peter Entel, Mario Siewert, Markus E. Gruner, Aparna Chakrabarti, Sudipta R. Barman, Vladimir V. Sokolovskiy, and Vasiliy D. Buchelnikov. Optimization of smart Heusler alloys from first principles. *Journal of Alloys and Compounds*, (0):In Press, 2012.

[Ful10] Brent Fultz. Vibrational thermodynamics of materials. *Progress in Materials Science*, 55:247–352, 2010.

[GAZ+08] M. E. Gruner, W. A. Adeagbo, A. T. Zayak, A. Hucht, S. Buschmann, and P. Entel. Influence of magnetism on the structural stability of cubic $L2_1$ Ni_2MnGa. *The European Physical Journal - Special Topics*, 158:193–198, 2008. 10.1140/epjst/e2008-00675-1.

[GCOM+99] Alfons Gonzàlez-Comas, Eduard Obradó, Lluís Mañosa, Antoni Planes, V. A. Chernenko, Bart Jan Hattink, and Amílcar Labarta. Premartensitic and martensitic phase transitions in ferromagnetic Ni_2MnGa. *Phys. Rev. B*, 60:7085–7090, Sep 1999.

[GE09] Markus Ernst Gruner and Peter Entel. Simulating functional magnetic materials on supercomputers. *Journal of Physics: Condensed Matter*, 21(29):293201, 2009.

[GLJDD+09] Xu Guo-Liang, Chen Jing-Dong, Chen Dong, Ma Jian-Zhong, Yu Ben-Hai, and Shi De-Heng. First-principles calculation of elastic and thermodynamic properties of Ni_2MnGa Heusler alloy. *Chinese Physics B*, 18(2):744, 2009.

[GPS+93] F. Güthoff, W. Petry, C. Stassis, A. Heiming, B. Hennion, C. Herzig, and J. Trampenau. Phonon dispersion of bcc La. *Phys. Rev. B*, 47:2563–2572, Feb 1993.

[GSL+03] Y. Ge, O. Söderberg, N. Lanska, A. Sozinov, K. Ullakko, and V.K. Lindroos. Crystal structure of three Ni-Mn-Ga alloys in powder and bulk materials. *Journal de Physique IV*, 112:921–924, 2003.

[HKC12] Burak Himmetoglu, Vamshi M. Katukuri, and Matteo Cococcioni. Origin of magnetic interactions and their influence in the structural properties of Ni_2MnGa and related compounds. arXiv:1203.1553v1 [cond-mat.mtrl-sci], Mar 2012.

[HPT+91] A. Heiming, W. Petry, J. Trampenau, M. Alba, C. Herzig, H. R. Schober, and G. Vogl. Phonon dispersion of the bcc phase of group-IV metals. II. bcc zirconium, a model case of dynamical precursors of martensitic transitions. *Phys. Rev. B*, 43:10948–10962, May 1991.

[HUAZ+12] Tilmann Hickel, Matthé Uijttewaal, Ali Al-Zubi, Biswanath Dutta, Blazej Grabowski, and Jörg Neugebauer. Ab Initio-Based Prediction of Phase Diagrams: Application to Magnetic Shape Memory Alloys. *Advanced Engineering Materials*, 14(8):547–561, 2012.

[HWL+12] T. D. Haynes, R. J. Watts, J. Laverock, Zs. Major, M. A. Alam, J. W. Taylor, J. A. Duffy, and S. B. Dugdale. Positron annihilation study of the Fermi surface of Ni_2MnGa. *New Journal of Physics*, 14(3):035020, 2012.

[JH68] G.B. Johnston and E.O. Hall. Studies on the Heusler alloys – I. Cu_2MnAl and associated structures. *Journal of Physics and Chemistry of Solids*, 29(2):193–200, 1968.

[JLX+02] Chengbao Jiang, Ting Liang, Huibin Xu, Ming Zhang, and Guangheng Wu. Superhigh strains by variant reorientation in the nonmodulated ferromagnetic NiMnGa alloys. *Applied Physics Letters*, 81(15):2818–2820, 2002.

[JMD+04] Chengbao Jiang, Yousaf Muhammad, Lifeng Deng, Wei Wu, and Huibin Xu. Composition dependence on the martensitic structures of the Mn-rich NiMnGa alloys. *Acta Materialia*, 52(9):2779 – 2785, 2004.

[KC10] S. Ozdemir Kart and T. Cagin. Elastic properties of Ni_2MnGa from first-principles calculations. *Journal of Alloys and Compounds*, 508(1):177–183, 2010.

[KDSA07] Mahmud Khan, Igor Dubenko, Shane Stadler, and Naushad Ali. Exchange bias behavior in Ni–Mn–Sb Heusler alloys. *Applied Physics Letters*, 91(7):072510, 2007.

[KG89] J. A. Krumhansl and R. J. Gooding. Structural phase transitions with little phonon softening and first-order character. *Phys. Rev. B*, 39:3047–3053, Feb 1989.

[Kit66] C. Kittel. *Phonons in Perfect Lattices and Lattices with Point Imperfections*, chapter General Introduction, pages 1–50. Oliver and Boyd, 1966.

[Kit86] C. Kittel. *Introduction to Solid State Physics*. John Wiley & Sons Ltd, 1986.

[KNT+11] S. Kaufmann, R. Niemann, T. Thersleff, U. K. R oler, O. Heczko, J. Buschbeck, B. Holzapfel, L. Schultz, and S. F ahler. Modulated martensite: why it forms and why it deforms easily. *New Journal of Physics*, 13(5):053029, 2011.

[KOAT03] V. V. Khovailo, K. Oikawa, T. Abe, and T. Takagi. Entropy change at the martensitic transformation in ferromagnetic shape memory alloys $Ni_{2+x}Mn_{1-x}Ga$. *Journal of Applied Physics*, 93(10):8483–8485, 2003.

[KPS+99] J. Kästner, W. Petry, S.M. Shapiro, A. Zheludev, J. Neuhaus, Th. Roessel, E.F. Wassermann, and H. Bach. Influence of atomic order on $TA_1[110]$ phonon softening and displacive phase transition in $Fe_{72}Pt_{28}$ Invar alloys. *The European Physical Journal B*, 10:641–648, 1999.

[KTB+01] V. V. Khovailo, T. Takagi, A. D. Bozhko, M. Matsumoto, J. Tani, and V. G. Shavrov. Premartensitic transition in $Ni_{2+x}Mn_{1-x}Ga$ Heusler alloys. *Journal of Physics: Condensed Matter*, 13(42):9655, 2001.

[LJC+07] Zhe Li, Chao Jing, Jiping Chen, Shujuan Yuan, Shixun Cao, and Jincang Zhang. Observation of exchange bias in the martensitic state of $Ni_{50}Mn_{36}Sn_{14}$ Heusler alloy. *Applied Physics Letters*, 91(11):112505, 2007.

[LRH02] Yongbin Lee, Joo Yull Rhee, and B. N. Harmon. Generalized susceptibility of the magnetic shape-memory alloy Ni_2MnGa. *Phys. Rev. B*, 66:054424, Aug 2002.

[LSS+04] N. Lanska, O. Soderberg, A. Sozinov, Y. Ge, K. Ullakko, and V. K. Lindroos. Composition and temperature dependence of the crystal structure of Ni–Mn–Ga alloys. *Journal of Applied Physics*, 95(12):8074–8078, 2004.

[Mar95] V.V. Martynov. X-Ray Diffraction Study of Thermally and Stress-Induced Phase Transformations in Single Crystalline Ni-Mn-Ga Alloys. *Journal de Physique IV*, C8:91–99, 1995.

[Meh07] T. Mehaddene. Unpublished measurements of 7M martensite of $Ni_{49}Mn_{21}Ga_{20}$ alloy. 2007.

[MFM94] Frederick Milstein, Huei Eliot Fang, and Jochen Marschall. Mechanics and energetics of the Bain transformation. *Philosophical Magazine A*, 70(4):621–639, 1994.

[MGCO+97] Lluís Mañosa, Alfons Gonz'alez-Comas, Eduard Obradó, Antoni Planes, V. A. Chernenko, V. V. Kokorin, and E. Cesari. Anomalies related to the TA_2-phonon-mode condensation in the Heusler Ni_2MnGa alloy. *Phys. Rev. B*, 55:11068–11071, May 1997.

[ML71] W. Marchall and S. W. Lovesey. *Theory of Thermal Neutron Scattering.* Oxford University Press, 1971.

[MMA+00] S.J. Murray, M. Marioni, S.M. Allen, R.C. O'Handley, and T.A. Lograsso. 6% magnetic-field-induced strain by twin-boundary motion in ferromagnetic Ni-Mn-Ga. *Applied Physics Letters*, 77(6):886–888, AUG 7 2000.

[MNP+08] Tarik Mehaddene, Jürgen Neuhaus, Winfried Petry, Klaudia Hradil, Philippe Bourges, and Arno Hiess. Interplay of structural instability and lattice dynamics in Ni_2MnAl. *Phys. Rev. B*, 78:104110, Sep 2008.

[MPZ+01] Lluís Mañosa, Antoni Planes, J. Zarestky, T. Lograsso, D. L. Schlagel, and C. Stassis. Phonon softening in Ni–Mn–Ga alloys. *Phys. Rev. B*, 64:024305, Jun 2001.

[PCSC00] J. Pons, V.A. Chernenko, R. Santamarta, and E. Cesari. Crystal structure of martensitic phases in Ni–Mn–Ga shape memory alloys. *Acta Materialia*, 48(12):3027–3038, 2000.

[PDL00] V. Petricek, M. Dusek, and Palatinus L. *Jana2000: Structure Determination Software Programs.* Institute of Physics, Praha, Czech Republic., 2000.

[PGPT01] V. K. Pecharsky, K. A. Gschneidner, A. O. Pecharsky, and A. M. Tishin. Thermodynamics of the magnetocaloric effect. *Phys. Rev. B*, 64:144406, Sep 2001.

[PHT+91] W. Petry, A. Heiming, J. Trampenau, M. Alba, C. Herzig, H. R. Schober, and G. Vogl. Phonon dispersion of the bcc phase of group – IV metals. I. bcc titanium. *Phys. Rev. B*, 43:10933–10947, May 1991.

[PMA09] Antoni Planes, Lluís Mañosa, and Mehmet Acet. Magnetocaloric effect and its relation to shape-memory properties in ferromagnetic Heusler alloys. *Journal of Physics: Condensed Matter*, 21(23):233201, 2009.

[POGM97] Antoni Planes, Obradó, Eduard, Gonzàlez-Comas, Alfons, and Mañosa, Lluís. Premartensitic Transition Driven by Magnetoelastic Interaction in bcc Ferromagnetic Ni_2MnGa. *Phys. Rev. Lett.*, 79:3926–3929, Nov 1997.

[PTH93] W. Petry, J. Trampenau, and C. Herzig. Phonon dispersion of β-Sc. *Phys. Rev. B*, 48:881–886, Jul 1993.

[RAC$^+$06] Lara Righi, Franca Albertini, Gianluca Calestani, Luigi Pareti, Antonio Paoluzi, Clemens Ritter, Pedro A. Algarabel, Luis Morellon, and M. Ricardo Ibarra. Incommensurate modulated structure of the ferromagnetic shape-memory Ni_2MnGa martensite. *Journal of Solid State Chemistry*, 179(11):3525–3533, 2006.

[RAP$^+$07] L. Righi, F. Albertini, L. Pareti, A. Paoluzi, and G. Calestani. Commensurate and incommensurate 5M modulated crystal structures in Ni–Mn–Ga martensitic phases. *Acta Materialia*, 55(15):5237–5245, 2007.

[RAP$^+$09] Lara Righi, Franca Albertini, Antonio Paoluzi, Simone Fabbrici, Elena Villa, Gianluca Calestani, and Stefano Besseghini. Incommensurate and Commensurate Structural Modulation in Martensitic Phases of FSMA. *Materials Science Forum*, 635:33–41, December 2009.

[RAV$^+$08] L. Righi, F. Albertini, E. Villa, A. Paoluzi, G. Calestani, V. Chernenko, S. Besseghini, C. Ritter, and F. Passaretti. Crystal structure of 7M modulated Ni–Mn–Ga martensitic phase. *Acta Materialia*, 56(16):4529–4535, 2008.

[RCG$^+$12] Katharina Rolfs, Markus Chmielus, Jan M. Guldbakke, Robert C. Wimpory, Annika Raatz, Winfried Petry, Peter Mllner, and Rainer Schneider. Key Properties of Ni–Mn–Ga Based Single Crystals Grown with the SLARE Technique. *Advanced Engineering Materials*, 14(8):614–635, 2012.

[RCW$^+$10] K. Rolfs, M. Chmielus, R.C. Wimpory, A. Mecklenburg, P. Mllner, and R. Schneider. Double twinning in Ni–Mn–Ga–Co. *Acta Materialia*, 58(7):2646–2651, 2010.

[Rei73] J. A. Reissland. *The Physics of Phonons*. John Wiley & Sons Ltd, 1973.

[Rei10] W. Reichardt. *Users Guide to GENAX2*, 2010.

[RFS$^+$06] M. Richard, J. Feuchtwanger, D. Schlagel, T. Lograsso, S.M. Allen, and R.C. OHandley. Crystal structure and transformation behavior of Ni–Mn–Ga martensites. *Scripta Materialia*, 54(10):1797–1801, 2006.

[Rol11] Katharina Rolfs. *Influence of the alloying element cobalt on the key properties of ferromagnetic shape memory Ni-Mn-Ga single crystals.* PhD thesis, Technische Universität München, 2011.

[SGD$^+$11] M. Siewert, M. E. Gruner, A. Dannenberg, A. Chakrabarti, H. C. Herper, M. Wuttig, S. R. Barman, S. Singh, A. Al-Zubi, T. Hickel, J. Neugebauer, M. Gillessen, R. Dronskowski, and P. Entel. Designing shape-memory Heusler alloys from first-principles. *Applied Physics Letters*, 99(19):191904, 2011.

[SGE12a] Mario Siewert, Markus E. Gruner, and Peter Entel. First-principles calculations of Ni_2MnGa phonon dispersion. Private Communication, 2012.

[SGE12b] Mario Siewert, Markus E. Gruner, and Peter Entel. First-principles calculations of $Ni_8Mn_5Ga_3$. Private Communication, 2012.

[Sha06] S. M. Shapiro. *Magnetism and Structure in Functional Materials.* Number 6. Springer, 2006. Chapter 6: Neutron Scattering Studies of Anomalous Phonon Behavior in Functional Materials.

[SHSS11] L. Straka, H. Hänninen, A. Soroka, and A. Sozinov. Ni–Mn–Ga single crystals with very low twinning stress. *Journal of Physics: Conference Series*, 303(1):012079, 2011.

[SLL$^+$10] N. Scheerbaum, Y.W. Lai, T. Leisegang, M. Thomas, J. Liu, K. Khlopkov, J. McCord, S. Fähler, R. Trger, D.C. Meyer, L. Schultz, and O. Gutfleisch. Constraint-dependent twin variant distribution in Ni_2MnGa single crystal, polycrystals and thin film: An EBSD study. *Acta Materialia*, 58(14):4629–4638, 2010.

[SLLU02] A. Sozinov, A.A. Likhachev, N. Lanska, and K. Ullakko. Giant magnetic-field-induced strain in NiMnGa seven-layered martensitic phase. *Applied Physics Letters*, 80(10):1746–1748, Mar 11 2002.

[SLN$^+$86] S. M. Shapiro, J. Z. Larese, Y. Noda, S. C. Moss, and L. E. Tanner. Neutron scattering study of premartensitic behavior in Ni–Al alloys. *Phys. Rev. Lett.*, 57:3199–3202, Dec 1986.

[SP06] Herbert R. Schober and Winfried Petry. *Lattice Vibrations*. Wiley-VCH Verlag GmbH & Co. KGaA, 2006.

[SPH71] G. Sandrock, A. Perkins, and R. Hehemann. The premartensitic instability in near-equiatomic TiNi. *Metallurgical and Materials Transactions B*, 2:2769–2781, 1971. 10.1007/BF02813251.

[Squ97] G. L. Squire. *Introduction to the Theory of Thermal Neutron Scattering*. Dover Publications Inc., 1997.

[Sri90] G. P. Srivastava. *The Physics of Phonons*. A. Hilger, 1990.

[SSSW84] S. K. Satija, S. M. Shapiro, M. B. Salamon, and C. M. Wayman. Phonon softening in $Ni_{46.8}Ti_{50}Fe_{3.2}$. *Phys. Rev. B*, 29:6031–6035, Jun 1984.

[SST02] Gen Shirane, Stephen M. Shapiro, and John M. Tranquada. *Neutron Scattering with a Triple-Axis Spectrometer*. Cambridge University Press, 2002.

[SVH$^+$07] S. M. Shapiro, P. Vorderwisch, K. Habicht, K. Hradil, and H. Schneider. Observation of phasons in the magnetic shape memory alloy Ni_2MnGa. *EPL (Europhysics Letters)*, 77(5):56004, 2007.

[SVK00] U. Stuhr, P. Vorderwisch, and V. V. Kokorin. Phonon softening in Ni_2MnGa with high martensitic transition temperature. *Journal of Physics: Condensed Matter*, 12(34):7541, 2000.

[SVKL97] U. Stuhr, P. Vorderwisch, V. V. Kokorin, and P.-A. Lindgård. Premartensitic phenomena in the ferro- and paramagnetic phases of Ni_2MnGa. *Phys. Rev. B*, 56:14360–14365, Dec 1997.

[SWZL00] D.L Schlagel, Y.L Wu, W Zhang, and T.A Lograsso. Chemical segregation during bulk single crystal preparation of NiMnGa ferromagnetic shape memory alloys. *Journal of Alloys and Compounds*, 312(1–2):77–85, 2000.

[THP$^+$91] J. Trampenau, A. Heiming, W. Petry, M. Alba, C. Herzig, W. Miekeley, and H. R. Schober. Phonon dispersion of the bcc phase of group − IV metals. III. bcc hafnium. *Phys. Rev. B*, 43:10963–10969, May 1991.

[TJ06] T.Mehaddene and J.Neuhaus. Unpublished EDX measurements of off-stoichiometric $Ni_{49}Mn_{32}Ga_{19}$. Aug 2006.

[TJ07] T.Mehaddene and J.Neuhaus. Temperature dependent inelastic neutron scattering measurements of $Ni_{49}Mn_{32}Ga_{19}$ in the austenite phase. 2007.

[TPH93] J. Trampenau, W. Petry, and C. Herzig. Temperature dependence of the lattice dynamics of chromium. *Phys. Rev. B*, 47:3132–3137, Feb 1993.

[UHK$^+$96] K. Ullakko, J. K. Huang, C. Kantner, R. C. O'Handley, and V. V. Kokorin. Large magnetic-field-induced strains in Ni_2MnGa single crystals. *Applied Physics Letters*, 69(13):1966–1968, 1996.

[UHN$^+$09] M. A. Uijttewaal, T. Hickel, J. Neugebauer, M. E. Gruner, and P. Entel. Understanding the Phase Transitions of the Ni_2MnGa Magnetic Shape Memory System from First Principles. *Phys. Rev. Lett.*, 102:035702, Jan 2009.

[VBK$^+$99] A. N. Vasil'ev, A. D. Bozhko, V. V. Khovailo, I. E. Dikshtein, V. G. Shavrov, V. D. Buchelnikov, M. Matsumoto, S. Suzuki, T. Takagi, and J. Tani. Structural and magnetic phase transitions in shape-memory alloys $Ni_{2+x}Mn_{1-x}Ga$. *Phys. Rev. B*, 59:1113–1120, Jan 1999.

[VKSC90] A. N. Vasil'ev, V. V. Kokorin, Y. I. Savchenko, and V. A. Chernenko. *Sov. Phys. JEPT*, 71:803, 1990.

[WCG$^+$01] W. H. Wang, J. L. Chen, S. X. Gao, G. H. Wu, Z. Wang, Y. F. Zheng, L. C. Zhao, and W. S. Zhan. Effect of low dc magnetic field on the premartensitic phase transition temperature of ferromagnetic Ni_2MnGa single crystals. *Journal of Physics: Condensed Matter*, 13(11):2607, 2001.

[WPT96] J. Worgull, E. Petti, and J. Trivisonno. Behavior of the elastic properties near an intermediate phase transition in Ni_2MnGa. *Phys. Rev. B*, 54:15695–15699, Dec 1996.

[WZTP84] P. J. Webster, K. R. A. Ziebeck, S. L. Town, and M. S. Peak. Magnetic order and phase transformation in Ni_2MnGa. *Philosophical Magazine Part B*, 49(3):295–310, 1984.

[XLP05] Feng Xiong, Yong Liu, and E. Pagounis. Fracture mechanism of a Ni–Mn–Ga ferromagnetic shape memory alloy single crystal. *Journal of Magnetism and Magnetic Materials*, 285(3):410–416, 2005.

[YQIE04] W. Yuan, Z. Qiao, Herbert Ipser, and Gunnar Eriksson. Thermodynamic assessment of the Ni–Ga system. *Journal of Phase Equilibria and Diffusion*, 25:68–74, 2004. 10.1007/s11669-004-0172-z.

[ZAER06] A. T. Zayak, W. A. Adeagbo, P. Entel, and K. M. Rabe. e/a dependence of the lattice instability of cubic Heusler alloys from first principles. *Applied Physics Letters*, 88(11):111903, 2006.

[ZEB04] A. T. Zayak, P. Entel, and V. D. Buchelnikov. Dynamical properties of Ni_2MnGa determined from density functional calculations. *Phase Transitions*, 77:253, 2004.

[ZH92] G. L. Zhao and B. N. Harmon. Phonon anomalies in β-phase Ni_xAl_{1-x} alloys. *Phys. Rev. B*, 45:2818–2824, Feb 1992.

[ZSW$^+$95] A. Zheludev, S. M. Shapiro, P. Wochner, A. Schwartz, M. Wall, and L. E. Tanner. Phonon anomaly, central peak, and microstructures in Ni_2MnGa. *Phys. Rev. B*, 51:11310–11314, May 1995.

[ZSW98] F. Zuo, X. Su, and K. H. Wu. Magnetic properties of the premartensitic transition in Ni_2MnGa alloys. *Phys. Rev. B*, 58:11127–11130, Nov 1998.

[ZSWT96] A. Zheludev, S. M. Shapiro, P. Wochner, and L. E. Tanner. Precursor effects and premartensitic transformation in Ni_2MnGa. *Phys. Rev. B*, 54:15045–15050, Dec 1996.

List of publications

Publications related to the dissertation

- S. Ener, J. Neuhaus, W. Petry, R. Mole, K. Hradil, M. Siewert, I. Titov, M.E.Gruner, P. Entel and M. Acet, Physical Review B *Effect of temperature and compositional changes on the phonon properties of Ni-Mn-Ga shape memory alloys*, **86** (2012) 144305.

- S. Ener, J. Neuhaus, B. Pedersen, W. Petry, *Vibrational properties of Ni-Mn-Ga shape memory alloy in the martensite phases*, (2012) In preperation.

Scientific reports

- S. Ener, J. Neuhaus, K. Hradil, R. Mole, P. Link and W. Petry, *Phonon properties of Ni-Mn-Ga shape memory alloys in martensite and austenite phases*, E13 Annual Report 2009.

- S. Ener, J. Neuhaus, R. Mole, K. Hradil, M. Siewert, B. Pedersen, I. Titov, M.E. Gruner, P. Entel, M. Acet, and W. Petry, *Effect of temperature and composition changes on phonon properties of Ni-Mn-Ga*, E13 Annual Report 2010.

- S. Ener, J. Neuhaus, D. Lamago, W. Petry, *Vibrational properties of austenite* Ni_2MnGa *Heusler alloy*, E13 Annual Report 2011.

Invited talks

- S. Ener, J. Neuhaus, W. Petry, *Ni-Mn-Ga Shape Memory Alloys: Phonon properties*, Seminar talk, Chemnitz, 24 May 2011.

Conference talks

- S. Ener, T. Mehaddene, J. Neuhaus, W. Petry, *Lattice dynamics in ferromagnetic shape memory alloys* 4th FRM II Workshop on Neutron Scattering, Burg Rothenfels, 15 – 18 Jun 2009.
- S. Ener, J. Neuhaus, K. Hradil, R. Mole, P. Link, W. Petry, *Dynamical properties of Ni-Mn-Ga alloys*, DPG Frühjahrstagung, Regensburg, 21–26 Mar 2010.
- S. Ener, J. Neuhaus, R. Mole, K. Hradil, B. Pedersen, W. Petry, *Phonon properties of Ni-Mn-Ga shape memory alloys*, FRM II User Meeting, Garching, 15 Oct 2010.
- S. Ener, J. Neuhaus, R. Mole, K. Hradil, W. Petry, *Effect of temperature and compositional changes on the vibrational properties of Ni-Mn-Ga alloys.* DPG Frühjahrstagung, Dresden, 13 – 18 Mar 2011.
- S. Ener, J. Neuhaus, W. Petry, *Phonon properties of magnetic shape memory materials*, 5th FRM II Workshop on Neutron Scattering, Burg Rothenfels, 6 – 9 Jun 2011.
- S. Ener, J. Neuhaus, W. Petry, *Vibrational Properties of Ni-Mn-Ga Ferromagnetic Shape Memory Alloys*, DyProSo XXXIII, Aussois, France, 18 – 22 Sep 2011.

Conference poster presentations

- S. Ener, T. Mehaddene, J. Neuhaus, K. Hradil, R. Mole, P. Link and W. Petry, *Phonon properties of Ni2mnGa in austenite and martensite phases*, SNI2010, Berlin, 24–26 Feb 2010.
- S. Ener, J. Neuhaus, R. Mole, K. Hradil, M. Siewert, I. Titov, M. E. Gruner, B. Pedersen, P. Entel, M. Acet, W. Petry, *Investigation of the phonon properties of Ni-Mn-Ga materials as a function of temperature*, ICFSMA'11, Dresden, 18 – 22 Jul 2011.

Acknowledgements

I want to thank to everybody who contributed directly or indirectly to this work in various ways;

- First of all, I would like to thank to Prof. Dr. W. Petry for giving me the opportunity to be a member of his research group at Technische Universität München and at Forschungs-Neutronenquelle Heinz-Maier Leibnitz (FRM II) for this PhD thesis. I also would like to thank him for giving me this interesting topic to work on and many thanks for fruitful discussions.

- I would like to thank to Dr. J. Neuhaus for his supervision and support throughout my thesis with his knowledge. I would also like to thank him for his stimulating and constructive criticism about my study and help throughout my work.

- I would like to than to Dr. K. Hradil, Dr.R. A. Mole and Dr. O. Sobolev for their assistance with the neutron scattering experiments on triple axis instrument (PUMA) at at Forschungs-Neutronenquelle Heinz-Maier Leibnitz (FRM II).

- I would like to than to Dr. B. Pedersen for his assistance with the neutron diffraction experiments on the RESI instrument at Forschungs-Neutronenquelle Heinz-Maier Leibnitz (FRM II). I also would like to thank him for his help on the Rietveld refinements.

- I would like to thank to Prof. Dr. M. Acet for giving me the opportunity to carry out some experiments at the Universität Duisburg-Essen and also for the discussions during my study. I would also like to thank my colleague I. Titov for assisting me on the magnetization measurements.

- I would like to thank to Prof. Dr. P. Entel, Dr. M. E. Gruner and Dr. M. Siewert for the first-principles calculations and beneficial discussions.

- I would like to thank to Dipl. Ing. S. Mayr for her assistance for the EDX measurements.

- I would like to thank to members of the workshop of “Chair of Functional Materials” and the workshop of at Forschungs-Neutronenquelle Heinz-Maier Leibnitz (FRM II) for their support on sample holders and sample environment for neutron scattering experiments.

- I would like to thank to all members of “Chair of Functional Materials” who welcomed me to the institute and offered a pleasant working atmosphere. I also would like to thank to the secretaries of “Chair of Functional Materials” and Forschungs-Neutronenquelle Heinz-Maier Leibnitz (FRM II) for their helps in administration.

- Financial support from the Deutsche Forschungsgemeinschaft through the Priority Program SPP1239 is gratefully acknowledged.

- Last but not least, I would like to thank to my parents for their never ending supports and encouragements throughout my whole life.

Appendix

Table 1: Room temperature phonon measurements of Ni_2MnGa single crystal in [ξ00] direction.

ξ (r.l.u.)	TA[ξ00] (THz)	TO^1[ξ00] (THz)	TO^2[ξ00] (THz)	TO^3[ξ00] (THz)	LA[ξ00] (THz)	LO^1[ξ00] (THz)	LO^2[ξ00] (THz)	LO^3[ξ00] (THz)
0.0	0	5.08	5.95	7.56	0	5.08	—	7.55
0.1	0.77	5.11	6.29	7.55	0.80	5.06	—	7.55
0.2	1.22	4.83	6.38	7.54	1.27	4.81	—	7.42
0.3	1.86	4.03	6.37	7.55	2.41	4.60	—	7.41
0.4	2.37	3.68	6.60	7.59	3.02	5.15	—	7.47
0.5	2.91	3.72	6.50	7.64	3.76	5.12	—	7.39
0.6	3.39	3.65	6.43	7.75	4.38	4.83	—	7.39
0.7	3.38	4.00	6.19	7.90	4.87	4.87	—	7.44
0.8	2.90	4.45	6.04	7.85	4.98	5.55	—	7.49
0.9	2.76	4.88	5.62	7.78	4.92	5.61	—	7.58
1.0	2.66	5.36	5.31	7.68	4.97	5.70	—	7.56

Table 2: Room temperature phonon measurements of Ni_2MnGa single crystal in [$\xi\xi$0] direction.

ξ (r.l.u.)	TA$_1$[$\xi\xi$0] (THz)	TO$^1_1$[$\xi\xi$0] (THz)	TO$^2_1$[$\xi\xi$0] (THz)	TO$^3_1$[$\xi\xi$0] (THz)	LA[$\xi\xi$0] (THz)	LO^1[$\xi\xi$0] (THz)	LO^2[$\xi\xi$0] (THz)	LO^3[$\xi\xi$0] (THz)
0.0	0	—	6.19	7.57	0	—	6.19	7.57
0.1	0.68	—	6.30	7.58	1.11	—	6.00	7.55
0.2	1.72	—	6.45	7.55	2.66	—	6.45	7.47
0.3	2.52	—	6.46	7.59	3.91	—	6.48	7.42
0.4	3.20	—	6.45	7.65	—	4.85	5.87	7.46
0.5	—	3.82	6.28	7.66	—	5.28	5.96	7.51
0.6	—	4.38	6.09	7.70	—	4.89	6.38	7.57
0.7	—	4.77	5.66	7.72	3.80	—	6.53	7.50
0.8	—	5.04	5.12	7.59	3.48	—	6.35	7.72
0.9	4.85	—	5.15	7.36	2.81	—	6.07	7.89
1.0	5.55	—	5.10	7.37	2.60	—	5.30	7.55

Table 3: Room temperature phonon measurements of Ni_2MnGa single crystal in $[\xi\xi0]$ direction.

ξ (r.l.u.)	$TA_2[\xi\xi0]$ (THz)	$TO_2^3[\xi\xi0]$ (THz)
0.0	0	7.57
0.1	—	7.57
0.15	0.466	—
0.2	0.47	—
0.25	0.457	—
0.3	0.419	—
0.35	0.473	—
0.4	0.697	7.56
0.45	1.023	—
0.5	1.377	—
0.55	1.657	—
0.6	1.874	7.63
0.65	2.054	—
0.7	2.21	7.94
0.75	2.352	—
0.8	2.469	7.94
0.85	2.56	—
0.9	2.631	8.14
0.95	2.649	—
1.0	2.677	8.23

Table 4: Room temperature phonon measurements of Ni_2MnGa single crystal in [$\xi\xi\xi$] direction.

ξ (r.l.u.)	TA[$\xi\xi\xi$] (THz)	TO^1[$\xi\xi\xi$] (THz)	TO^2[$\xi\xi\xi$] (THz)	TO^3[$\xi\xi\xi$] (THz)	LA[$\xi\xi\xi$] (THz)	LO^1[$\xi\xi\xi$] (THz)	LO^2[$\xi\xi\xi$] (THz)	LO^3[$\xi\xi\xi$] (THz)
0.0	0	5.09	6.19	7.57	0	5.09	6.15	7.53
0.05	—	4.97	6.20	7.52	0.84	5.06	6.20	7.48
0.10	—	4.91	6.28	7.52	1.80	4.92	6.34	7.48
0.15	1.23	4.57	6.34	7.51	2.58	4.45	6.41	7.44
0.20	1.63	4.38	6.38	7.50	3.34	—	—	—
0.25	1.94	4.20	6.45	7.48	3.99	4.32	6.34	7.40
0.30	2.20	3.92	6.48	7.50	3.90	4.72	6.08	7.45
0.35	2.57	3.83	6.51	7.49	3.89	5.21	6.10	7.46
0.40	2.70	3.82	6.53	7.46	4.02	5.28	6.18	7.47
0.45	2.98	3.48	6.50	7.47	4.20	4.96	6.02	7.41
0.50	3.56	3.61	6.48	7.45	4.48	4.86	6.15	7.35

Table 5: Room temperature phonon measurements of Ni_2MnGa single crystal in $[2\xi\xi0]$ direction.

ξ (r.l.u.)	LA$[2\xi\xi0]$ (THz)	LO$^1[2\xi\xi0]$ (THz)	LO$^2[2\xi\xi0]$ (THz)	LO$^3[2\xi\xi0]$ (THz)	TA$[2\xi\xi0]$ (THz)	LO$^1[2\xi\xi0]$ (THz)	LO$^2[2\xi\xi0]$ (THz)	LO$^3[2\xi\xi0]$ (THz)
0.0	0	5.08	5.31	7.56	0	5.08	5.95	7.54
0.05	—	4.63	6.27	—	—	4.81	5.49	—
0.1	2.04	4.65	6.29	7.54	0.73	4.74	6.03	7.53
0.15	3.18	4.34	6.20	—	—	4.65	6.39	—
0.2	3.85	4.39	5.92	7.61	1.37	—	5.35	7.52
0.25	4.84	3.37	5.85	—	—	4.84	5.79	—
0.3	5.40	3.35	—	7.61	2.24	5.19	6.38	7.57
0.35	5.17	3.15	—	—	—	5.22	6.10	—
0.4	4.72	3.14	—	7.60	2.99	5.04	6.01	7.36
0.45	4.16	3.49	—	—	—	5.03	6.17	—
0.5	3.53	3.52	5.10	7.68	3.53	5.11	6.62	7.72
0.55	3.05	3.87	5.27	—	—	—	—	—
0.6	2.59	3.77	5.27	7.80	3.97	5.88	6.12	7.71
0.65	2.28	—	—	—	—	—	—	—
0.7	2.27	3.44	5.09	7.80	4.43	5.47	6.32	7.59
0.75	2.59	—	—	—	—	—	—	—
0.8	3.06	3.07	4.89	7.73	4.70	4.70	5.82	7.59
0.85	3.54	3.20	4.63	—	—	—	—	—
0.9	4.63	3.11	—	7.68	5.08	5.08	5.51	7.43
0.95	—	2.72	—	—	—	—	—	—
1.0	5.30	—	5.10	7.66	5.24	5.23	5.23	7.55